Theses and Dissertations

2019-06-01

Mechanically Scanned Interference Pattern Structured Illumination Imaging

Jarom Silver Jackson
Brigham Young University

Follow this and additional works at: https://scholarsarchive.byu.edu/etd

Mechanically Scanned Interference Pattern Structured Illumination Imaging

Jarom Silver Jackson

A dissertation submitted to the faculty of
Brigham Young University
in partial fulfillment of the requirements for the degree of

Doctor of Philosophy

Dallin S. Durfee, Chair
Jean-Francois Van Huele
Michael Ware
Scott Bergeson
Justin Peatross

Department of Physics and Astronomy

Brigham Young University

ABSTRACT

Mechanically Scanned Interference Pattern Structured Illumination Imaging

Jarom Silver Jackson
Department of Physics and Astronomy, BYU
Doctor of Philosophy

A method of lensless, single pixel imaging is presented. This method, referred to as MAS-IPSII, is theoretically capable of resolutions as small as one quarter of the wavelength of the imaging light. The resolution is not limited by the aperture of any optic, making high resolutions (including subwavelength) feasible even at very large (greater than a meter) distances. Imaging requires only flat optics and a coherent source, making it a good candidate for imaging with extreme wavelengths in the UV and x-ray regimes. The method is demonstrated by the imaging of various test targets. Both real and complex imaging (i.e. holography) is demonstrated.

ACKNOWLEDGMENTS

I would like to acknowledge and thank all those who made it possible for me to be where I am today and to complete the research that I have done. I am very grateful to the BYU physics department for providing a solid base education in physics, as well as some of the resources that made my research possible. I am also grateful to many of the people at BYU who helped, directly or indirectly with my research. Dr. Neal Bangerter oversaw my project for a medical imaging class that eventually lead to the work that is the focus of this dissertation. A couple undergraduate students Dallen Petersen and Ben Whettan, have been very helpful. I am grateful to the members of my committee for being willing to work with me, review my work, and who were always willing to make time to talk to me when I needed another perspective on a difficult problem. I am especially grateful for Dr. Dallin Durfee, who has not only been my graduate advisor, but also a mentor, a teacher and a friend.

I want to acknowledge my parents, who are responsible for starting me on this path, and my wife Amber, who has been instrumental in helping me finish it. Amber has been extremely supportive and understanding, even when at times I would run off to the lab late at night, or on weekends and holidays to check on an experiment or fix something that went wrong. I think she may be even more excited than I am to finally be done.

Contents

List of Figures

List of Tables

Chapter 1

Introduction

Imaging developments are linked hand in hand with scientific progress in many fields. The development of the telescope in the 17th century led to a revolution in astronomy and was followed closely by the invention of the compound microscope. This brought into being the field of microbiology and all the medical advances that came soon thereafter. Developments in medical and scientific imaging through the 20th century were often followed by a slew of scientific breakthroughs, many of which have practical real world applications and improve quality of life for people around the world. All of these developments have led to a vast landscape of imaging modalities which work on a variety of base physical principles and have different sets of strengths and weaknesses. This gives researchers a large tool bag to draw from when attempting to understand the world and solve new problems. My intention in this dissertation is to make a contribution to this list of imaging possibilities and to add some new insight to the subset of imaging methods related to my work. The method I propose, develop theory for and demonstrate is related to a type of imaging which I will refer to throughout this document as interference pattern structured illumination imaging (IPSII for short). My contribution to this subfield is a type of mechanical angle scan IPSII, or MAS-IPSII for short, that allows for fully lensless single pixel IPSII imaging.

MAS-IPSII combines some of the advantages of existing IPSII techniques with the advantages

of imaging without the need of a lens. This leads to a variety of potential use cases discussed later, and gives MAS-IPSII a unique position within the field of imaging techniques. The development of this method, and the proof of concept experimentation I have done have made for an extensive project in its own right. Further development and work are still required to realized the full potential of the method, or even establish the practicality of many of the use cases I propose.

My purpose here is to introduce the method, the theory, the potential applications, demonstrate proof-of-concept experiments, and lay down a course for continued exploration and development. In order to understand the motivation for my work, I would like to break optical imaging into a few categories to illustrate how IPSII fits in. I will also give a brief overview some methods in each category, with emphasis on IPSII related techniques, their use cases and drawbacks.

There are many ways to categorize imaging methods. I'd like to start by dividing them into two categories: analog image formation, and computational imaging. The first category contains methods that rely on actual image formation—these are analog methods which could work with photo sensitive film, and are often compatible with manual viewing with the eye. The second category contains techniques which require acquired data to be processed and displayed digitally before a meaningful object space image is obtained.

1.1   Analog Imaging

There are a few ways to create real, viewable images. The simplest, in concept, is what I will refer to as 'shadow imaging', where the light passes through or around an object and onto a detector (e.g. photographic film, CCD detector array, etc). With an opaque object, this only gives the outline of an object. If the object is transparent, the light transmitted through the object also gives information about the inside of the object. Examples of shadow imaging in practice include medical x-ray radiography and CT imaging, as well as some forms of on-chip microscopy [1–6]. This type of

imaging uses the ray approximation—the assumption that light acts like a particle, traveling in a straight line. This assumption is approximately correct if the features being imaged are sufficiently large relative to the wavelength of the light and the working distance (the distance between the detector and the object). This works well for x-rays because the wavelength is extremely small compared to what is being imaged (bones, organs, etc.). For imaging of smaller things with larger wavelengths (such as optical microscopy), the detector has to be placed extremely close to the object because small features in the wavefronts of light diffract at wide angles, causing the ray approximation to break down even over small distances.

The limitations imposed by the diffraction of light are most easily overcome by focal plane imaging, which is by far the most common category of imaging. This type of imaging uses precisely curved surfaces to refract or reflect light in such a way that light from a given point on one plane converges, or focuses, on a single point on another plane. In the ray optics approximation this means all rays emitted from any single point on one plane (the 'object' plane) come back together at a single corresponding point (the 'conjugate' point) on another plane (the 'conjugate' plane), thus recreating the intensity pattern of the light at the object on another plane, usually with some amount of magnification.

Another explanation for focal imaging is that the optic is shaped such that the sum of light rays traveling along every available path from a given point on the object plane interferes destructively at every point on the conjugate plane except the conjugate point. In this view, even focal plane imaging could be seen as a type of 'interference pattern' imaging, but I will reserve that language for other approaches. In either view, the important concept is that the focal optic creates a kind of copy of the light-field at the object on another plane. A sensor or piece of film placed at that plane records information as if it were directly on top of the object, thus avoiding the blurring caused by diffraction effects that are an inherent problem in shadow imaging.

The properties of images created by focal plane imaging are dependent on the focusing optic.

Resolution of an ideal focusing optic depends on the angle 2θ subtended by the optic from the point of view of the object, which causes an unavoidable trade-off between working distance (WD), optic size d, and resolution dx, which can not be independently optimized:

$$dx \approx \frac{\lambda}{2n\sin\theta} = \frac{\lambda}{2\text{NA}} \tag{1.1}$$

$$\tan\theta = \frac{d}{2\text{WD}}, \tag{1.2}$$

where $\text{NA} = n\sin\theta$ is the numerical aperture of the lens, and n is the index of refraction of the medium surrounding the object. Resolution can be defined in various ways, leading to slightly different results (e.g. the Raleigh criterion, which instead gives $dx \approx .61\lambda/\text{NA}$).

A second key property is the depth-of-field (DOF), the region in front of and behind the object plane from which light will still be focused to a sufficiently small point on the conjugate plane to not cause significant blurring. The DOF limits the depth of an object that can be clearly imaged, and is also directly related to the numerical aperture such that there is an inverse relationship between depth-of-field and resolution. This is one of the core limitations in the field of optical microscopy.

Finally, the quality of an image is also affected by deviations of the focusing optic from ideal behaviour. There are several types of image aberrations (distortions) which are caused by deviations of an optic from the ideal shape, wavelength dependent properties, and off-axis effects. These included spherical aberrations, chromatic aberrations, coma, and other distortions caused by imperfect lenses.

Another method of real image formation is 'pinhole' imaging. Light from the object is passed through a tiny hole. From a ray optics perspective, you can think of the hole as blocking all rays but one from each point, so that on any later image plane, each point is only illuminated by a single ray from a corresponding point on the object. The result is similar to that of imaging with a lens, but with essentially unlimited DOF. However, almost all of the light has to be thrown away, so this method requires very bright illumination and a sensitive detector. Furthermore, the amount of light scales inversely with the square of the pinhole radius, which in turn scales with resolution, so higher

resolutions require even more illumination. If the hole is very small, then diffraction effects also limit resolution, making pinhole cameras incapable of resolutions close to the wavelength of light. These limitations make pinhole imaging useful in only niche cases.

The last type of analog imaging I will mention is holography. While this does not quite fit in the same category as the other mentioned 'real' image formation methods, I include it here because traditional holography does not require any computation. Holography uses (in its simplest form) monochromatic light. Light from the object is interfered with light from a reference. This interference pattern is recorded on film. The object wave is then recreated by passing a copy of the original reference wave through the film, which modifies the light wavefronts back to something similar to the original wavefronts coming off the object, so that when viewing through the film, it appears as if the object is where it originally was. Holography is a very powerful technique because holograms contain some amount of 3D information about an object. However, it is very difficult to do outside of carefully controlled imaging setups.

1.2   Computational Imaging

The category of computational imaging is very broad, with many methods under current development, and includes any method where the measured information must be processed in some way before a useful image is obtained. In principle, any image produced by any analog imaging method could be reproduced computationally with a direct measurement of the object wave—no optics necessary—but this would require full phase information. Unfortunately optical photodetectors cannot measure phase directly, so a variety of other methods must be used. The following is a brief survey of these methods, focusing mainly on those that are relevant to understanding the development and utility of IPSII.

Digital Holography

Digital holography is a field that attempts to find missing phase information with a variety of methods. Similar to analog holography, for example, a reference wave may be used to create interference fringes which are modulated in time or space. Demodulating these fringes gives the spatial phase of the object wave. Another approach is to measure the object wave at multiple image planes, then use iterative methods and fill in the missing phase information that is consistent with the changes in intensity. Once phase is determined, the object wave is then processed to give an in-focus image at any plane, or a stack of focused images of the object.

Another recent form of computational imaging that is making its way into practical devices is plenoptic, or 'light-field' imaging. It is so termed because it measures not only the intensity of light at a given point, but also vector directions for the light rays passing though each pixel. This allows light from different places to be separated. In practical terms this allows the taking of digital pictures whose focus and DOF can be computationally altered at will—similarly to what is possible with digital holograms.

Structured Illumination

A very different type of computational imaging is structured illumination imaging (SI), which abandons the basic goal of measuring the object wave that is common to most imaging methods. SI instead attempts to use knowledge about the structure of the illuminating light, which can be controlled. In SI a known pattern of light is used to illuminate an object. A detector then uniformly samples the light passing through or reflecting off the object. The signal on this detector is proportional to the overlap between the illumination pattern and the object. As such, it contains information about the amount of the given pattern 'contained' in the object. By repeating this measurement with many different patterns, enough information is gleaned to reconstruct an image of the object.

Technically, even raster scan methods, such as LIDAR, are a simple form of SI where the illumination 'patterns' are just a dot of illumination that is scanned over the object. However, use of the term usually refers to a method that uses a non-trivial basis set for the illumination, and requires some computation to transform from the SI basis to an object space image. The most convenient basis sets to use in SI are 2D orthonormal basis functions sets such as sine/cosine [7] waves or Hadamard functions [8]. When such an orthonormal set is used, each measurement gives one component of the object image in the basis set. When all such components are measured a corresponding inverse transform (such as an inverse Fourier transform) may be used to reconstruct the image.

Among other benefits, SI also introduces the possibility of compressive sensing. This is a technique that reproduces an image with fewer measurements than the effective pixel count of the resulting image. The additional information is generated by using very high level abstract assumptions about the nature of the image—typically the fact that meaningful (to humans) images usually have a high degree of sparsity in various alternate domains such as the Fourier domain.

1.3   Lensless Imaging

Lenses (or other equivalent focusing optics) are typically employed in most forms of imaging, and are responsible for many of the fundamental and technical limitations that constrain how well anything can be imaged. Fundamental constraints include the trade-off between resolution and depth of field, and the trade-off between working distance and optic size (for a given resolution and DOF). Technical challenges include spherical and chromatic aberrations, coma and lens imperfections, and absorption.

The alternative to refractive lenses are reflective focusing devices (e.g. spherical or parabolic mirrors), but these place the same fundamental constraints on imaging as equivalent lenses. They

also face many of the same technical challenges (with the exception of chromatic aberrations). Unlike lenses, however they are also difficult to stack in an imaging system, making aberration minimizing multi-element objectives much more difficult to design and manufacture. For this reason, microscope objective and commercial camera lenses are almost always built from refractive lenses.

The technical problems with lenses increase quickly with size, which in practice limits the diameter of high quality lenses to a few cm. This means that high NA diffraction limited resolutions (i.e. on the scale of a wavelength of light) are only feasible at very short working distances, typically less than a cm. Larger apertures are possible for mirrors, which are typically used in long working-distance imaging (e.g. telescopes). However, they are not very practical for high-NA applications, such as microscopy.

Another limitation imposed by lenses (and other focusing devices) is the availability of appropriate materials for the desired wavelengths. In the optical region we have a wide range of highly transparent or reflective materials available for refractive or reflective focusing, respectively. This is not the case at shorter wavelengths where refractive optics are generally out of the question, and even reflective focusing optics are difficult to make. Deep UV (DUV) and soft X-ray (SXR) optics have been an active area of of research and development for decades, and still face many challenges [9, 10]. Even for applications at longer than visible wavelengths, such as far infrared (FIR) and terahertz (THZ) imaging, where refractive optics are more readily available, lenses are still often a limiting necessity and are an ongoing area of research [11, 12].

Lensless imaging is a holy grail in many fields of optics because of these constraints. Unfortunately, methods compatible with lensless imaging are often limited in even more restrictive ways than the limitations imposed by a lens. Typically a lens is still used in methods capable of lensless imaging because it greatly simplifies and enhances most methods. Methods that can be implemented without use of a lens or focusing optic include shadow imaging, pinhole imaging,

structured illumination and holography.

Pinhole imaging has its use cases, as discussed previously, but is not a general solution to the lens problem. Holography also has its niche applications, but also is not a general solution. Analog holograms could potentially record information without lenses, but would require the same optics to view the hologram as would be needed to view the object (e.g. if the object were microscopic). Digital holography is much more promising, but recording a digital hologram is no small technical feat, and remains an active area of research due to the detector resolution needed to record a hologram.

Lensless shadow imaging and structured illumination, on the other hand, are in common practical usage. They generally have the same limitations on resolution due to diffraction effects, however. In the case of shadow imaging , the detector needs to be close to the object. Equivalently, in the case of shadow SI [13], the mask forming the shadow needs to be close to the object. In both cases this means the ratio of the working distance to the desired resolution must be much smaller than the ratio of the desired resolution to the wavelength of light used. If anything close to wavelength scale resolution is desired, then the working distance is going to be on that same scale. This makes it difficult to achieve ultra high resolutions (e.g. smaller than a wavelength) with lensless shadow imaging or most types of structured illumination imaging, though methods such as on chip microscopy [3] and optofluidic devices [2, 4] attempt to do so by minimizing the distance between sensor and sample.

1.4   Single Pixel Imaging

Another limitation of traditional digital imaging is the need for a detector array. In practice, there are usually a number of constraints involved with this. While detectors are available for wavelengths ranging from gamma rays into the THz region, only a few of these detector technologies have been

used to realize small detectors that can be packed into a detector array. Even for the wavelength regions where such technologies do exist (e.g. CCD and CMOS in the optical and near infrared), they often have a lower sensitivity and quantum efficiency than is available in the best single pixel detectors. Furthermore, all detector arrays have an effective fill ratio which is less than ideal—there are gaps and dead-zones between individual pixel detectors where signal is lost. This typically results in a loss of 0 to 70% of the useable signal, depending on the type of detector used [14, p.11].

Because of the limitations imposed by detector arrays, imaging techniques that require only a single detector (i.e. single pixel) can be useful in a variety of situations. THz imaging, for example, typically uses single pixel methods [12]. Many optical microscopy techniques also use single pixel methods, such as confocal laser scanning microscopy.

In principle, any method using an array detector could be converted into a single pixel method by raster scanning an aperture or detector where the array detector would have been. However, such a method would throw out most of the light with each measurement, resulting in a photon efficiency inversely proportional to the pixel number. Either the noise in the image or the time to take the image would increase drastically compared to using an array detector. Because of this, single pixel imaging in practice is typically confined to SI based techniques (which are inherently single-pixel detector methods) where there is no fundamental drop in photon efficiency.

1.5   Interference Pattern Structured Illumination Imaging

The motivation behind our method (MAS-IPSII) is that it has the potential to resolve many of the problems discussed in previous sections. It can be done without lenses (and all the limitations they impose), at arbitrary working distances (unlike other lensless methods), and with a single pixel detector. The key idea that makes this all possible is that interference patterns can be generated with fine features without the use of focusing optics, and at large distances.
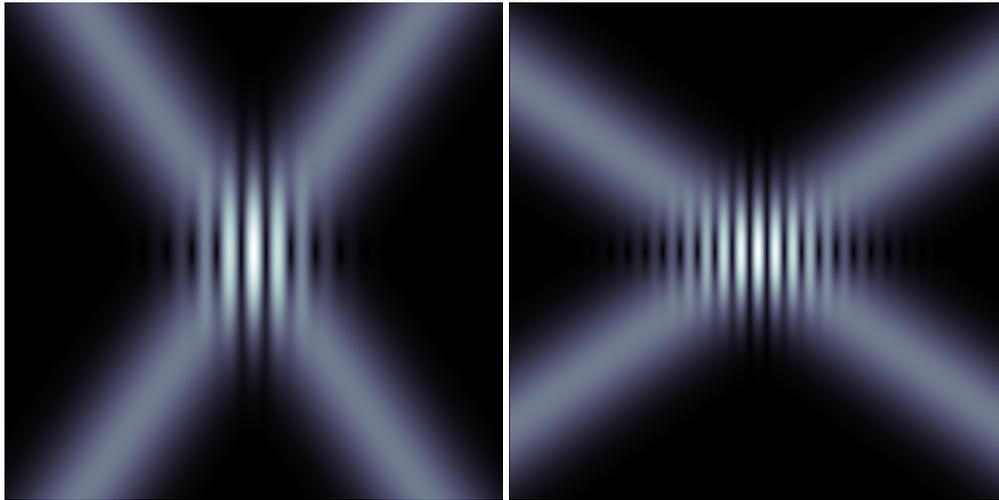
Figure 1.1 Two beams with flat wavefronts interfere to create sinusoidal fringes. Left: beams crossing at a small angle create large fringes. Right: beams crossing at a large angle create small fringes.

Consider two plane waves interfering at an angle of 2θ from each other. A pattern of constructive (bright) and destructive (dark) planar fringes is created (see Fig. 1.1). The intensity of the fringes varies sinusoidally, with a fringe spacing proportional to the wavelength and inversely proportional to the sine of θ. The smallest fringes that can be created are just half a wavelength apart. The width of one of those fringes (full width half maximum - FWHM) is about one quarter a wavelength of light.

Since SI is ultimately limited (in resolution) to the scale of features that can be created in the illumination, SI using interference fringes should, in principle, be capable of resolutions as fine as a quarter the wavelength of light. In fact, this possibility is the key motivation for the development of a set of IPSII related techniques over the past couple of decades (and one of the motivations of our own method).

One of the earliest IPSII implementations was a hybrid SI and traditional imaging technique referred to as structured illumination microscopy, or SIM. This technique was developed as a way of enhancing the resolution of traditional microscopes by using finely spaced interference fringes.
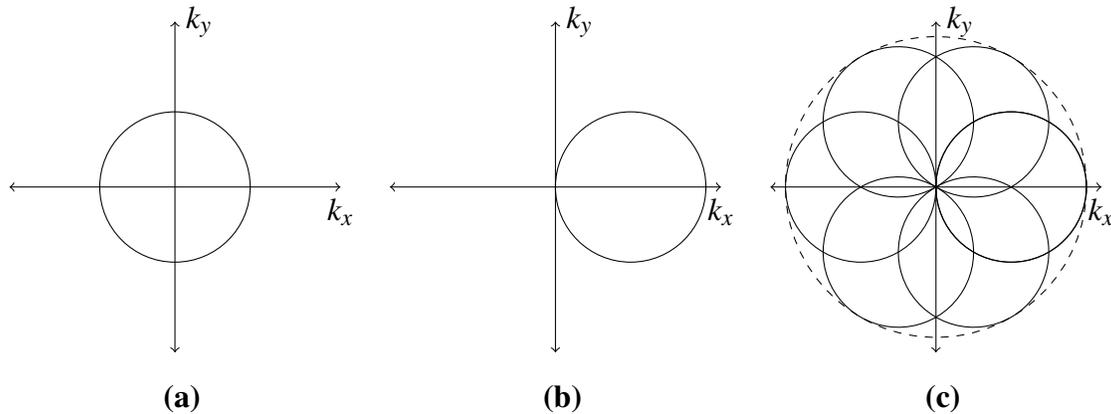
Figure 1.2 Microscope k-space bands. (a) The information that can be measured by a traditional microscope is limited to the area inside a circle in k-space centered on the origin. (b) If the object is spatially modulated by illuminating with a sinusoidal pattern (e.g. with an interference pattern) the band of the microscope is shifted by an amount corresponding to the k-value of the modulating fringes, though the area remains the same. (c) By taking multiple images with different pattern orientations, a new effective k-space band (dashed circle) is established with double the radius, effectively doubling the resolution.

SIM is often describe in terms of spatial modulation.

If we consider a microscope in k-space, the resolution limit of the microscope is equivalent to a low-pass cutoff. In other words, there is a circle, centered on the origin, in the Fourier domain beyond which the microscope cannot measure any information. This circle, or 'band' depends on the numerical aperture of the microscope objective and, ultimately, on the wavelength of light.

By illuminating an object with spatially modulated light (such as the fringes in a sinusoidal interference pattern), the band of a microscope is translated away from the origin of k-space in the direction of the k-vector of the fringes (see Fig. 1.2). The fringes are engineered to translate the band of the microscope by its radius, so that the edge of the band crosses the origin of k-space. The point furthest away from the origin is then twice as far as what was originally accessible, so the resolution of the microscope is effectively doubled. Multiple images are required, of course, with patterns at different orientations to fill in sufficient information to reconstruct the object at this new doubled resolution.

Reconstruction of SIM images is slightly complicated because the intensity modulation causes the microscope to simultaneously measures two bands translated in opposite directions from the origin in k-space. However, this information is separable if the phase of the fringes is carefully controlled, and images at multiple phases are acquired.

One of the limitations on SIM is the fact that the interfering light passes through the imaging lens, and therefore SIM is still subject to all the same fundamental imaging constraints imposed by the lens on working distance, resolution and DOF, except for the (not-insignificant) factor of 2 improvement in resolution. It also makes SIM subject to lens aberrations and imperfections.

Since the fringes in SIM are the primary source of high resolution information, there is no inherent reason why many of the imaging properties need to be tied to the imaging lens at all. This was the motivation for the work done by Mermelstein et al. with their multibeam IPSII technique [15–18]. By illuminating the sample with beams that do not pass through the microscope objective, their method was able to partially decouple resolution from the imaging objective.

The Mermelstein multi-beam method uses 31 fixed beams arranged to form a cone. Each pair of beams generates a slightly different pattern spacing and orientation, such that over 900 patterns may be formed. This effectively allows each pixel from the low resolution traditional microscope to be further divided into as many sub-pixels, thus extending the resolution of the microscope far beyond the capability of the low NA imaging objective. Because the imaging objective has a low NA, this also allows for a much greater DOF than would normally be possible. Basically, the resolution is set by the effective NA of the cone of the illumination beams, whereas the DOF is set by the traditional imaging objective. However, the cone and the imaging objective also need to be properly matched to avoid aliasing within individual pixels, such that there is still a minimum requirement on the pixel count and resolution of the traditional imaging elements, or the IPSII elements would fail.

Because IPSII allows, in principle, arbitrary points in k-space to be measured there is no inherent need for a traditional imaging setup at all. This has been amply demonstrated by Feldkhun et al.

with their IPSII based methods, DEEP and $\mathscr{F}$-basis [19–21]. These use an acousto-optic modulator to quickly scan the angle of a laser. This setup can generate a diverging beam pair, but to bring the beams back together a lens is, unfortunately, necessary. DEEP appears to be the first example of single pixel IPSII, or what could be viewed as a form of single pixel SIM. It does not require an imaging objective, and is also the first to demonstrate IPSII without the need for any traditional imaging optics. However, the need for a lens in the projection system still ties DEEP and $\mathscr{F}$-basis to many of the familiar lens based constraints. Their work is important, however, as it shows the potential of IPSII to be of practical use. By multiplexing the signals from multiple beam pairs into the detector frequency spectrum (similar to the multi-beam approach described above), $\mathscr{F}$-basis is capable of measuring up to 10^5 measurements in a single spectrum measurement from the detector, meaning that high voxel count 3D volumes can be measured in seconds (faster than conventional 3D volumetric microscopy techniques).

Various other methods related to IPSII have been demonstrated as well, such as SPIFI [22, 23] which uses custom spinning patterns to form *spatially* modulated illumination patterns, which then multiplex *spatial* information onto the frequency spectrum of the detector (similar to how $\mathscr{F}$-basis effectively multiplexes spatial *frequency* information onto the temporal signal spectrum). More recent work in this line (CHIRPT [24, 25]) has demonstrated how some coherent imaging techniques can be used if coherent illumination is used, even if the detected light is not coherent (e.g. Fluorescent based imaging). Other related work includes axial IPSII [26], and various modern lines of inquiry into advanced SIM techniques, such as SIM with non-sinusoidal patterns [27], etc.

1.6 MAS-IPSII

I have so far described the development and motivation for various imaging techniques utilizing interference patterns as a resolution enhancing source. IPSII has been demonstrated with a lens only

in the imaging optics, or a lens only in the projection optics, but has not been demonstrated without a lens (or other focusing device) anywhere in the system. I have also discussed the limitation that such a focusing device places on imaging systems, as well as the limitations on what few truly lensless imaging modalities do exist.

To completely remove the need for a lens from IPSII we have developed a mechanical angle scan IPSII (MAS-IPSII) method. This uses only flat optics—no lens is required in structured illumination pattern formation, imaging, or light collection. The method is in principle capable of arbitrary FOV, and resolution down to a quarter wavelength. The FOV is limited only by the size of the beams used and the precision of the mechanical angle scan, while the resolution is limited by the wavelength and the range of the mechanical angle scan (i.e. the effective NA).

MAS-IPSII uses a set of motorized mirrors and beams splitters to interfere two laser beams on an object at arbitrary computer controlled angles. Light from the interference pattern scatters off or through the object and is measured by an optical detector. This detector effectively measures a single spatial frequency of the object in k-space. The angle is scanned and data is taken to fill in a grid of k-space values. When this process is complete a simple, quick, inverse Fourier transform algorithm is applied to the data resulting in an image of the object.

MAS-IPSII is unique among imaging methods, even compared to other IPSII methods. It is the first demonstration of IPSII without any lenses. Compared to other IPSII methods, it also uses a greatly simplified set of optics (e.g. no acousto optics or scanning grating patterns are needed). It is the only imaging method we are aware of that has the potential for sub-wavelength imaging without a lens, while maintaining a reasonable working distance (i.e. much greater than a wavelength).

The fact that MAS-IPSII requires only flat mirrors and beam splitters makes it a promising candidate for difficult wavelength regimes such as DUV or X-ray. An X-ray MAS-IPSII device using a fairly small angle scan (eg. 15°), such as what we have demonstrated optically, would be capable of resolutions much higher than state of the art X-ray microscopy.

Another use of MAS-IPSII is to explore IPSII related issues that can be of benefit to other IPSII implementations. These issues include wavefront distortions, the effect of shadows in the interference pattern on resulting reconstructions, large FOV imaging and related constraints such as aliasing, k-space position error, and dynamic range. MAS-IPSII is well suited for this because in many ways it is more simple and controlled than other IPSII methods. For example, the multibeam method, DEEP, and other methods using acousto-optics are affected by how the acousto-optics distort the wavefronts, on top of any other distortions introduced by optics etc. With MAS-IPSII, however, the two beams are well defined and separated so we can manipulate them in more controlled manners.

1.7   My Research at BYU

The main topic of this dissertation is my work on imaging, which has resulted in one patent pending and three peer reviewed publications (two conference proceedings and an article published in Optics Express—see Appendix A.1). However, in addition to the work presented in this dissertation, I also worked on several other research projects as well, some of which have also resulted in publications (see Appendix A.1 for a summary). I would like to take some space here to summarize my graduate research activities.

My original research was focused on building a matterwave ion interferometer experiment. This project led to work we did on the Hanle effect, though the interferometer concept it self was eventually abandoned in favor of more productive lines of research.

The directional Hanle effect is a phenomena we encountered while working on the interferometer project and needed a way to 'see' magnetic fields. We felt this phenomena was interesting enough in its own right to pursue, and ultimately I wrote my masters thesis on it. After my masters degree was complete, however, we made important improvements to our theory and understanding of this

effect, as well as our understanding of the background literature. As a result we spent a significant amount of time reworking the theory, calculations, and taking new data. All of this resulted in a paper which is currently under review.

Another side project was a method of using pairs of imperfect waveplates together to achieve the same result as a single waveplate for some use cases. These results were published (see Appendix A.2) in a paper which described the use of pairs of waveplates with a polarizing beam splitter to achieve near ideal variable light splitting (i.e. 0-100%), even with waveplates made for very different wavelengths.

I have also spent a significant amount of time mentoring undergraduate and summer REU students. These students were working on various projects, including early versions of IPSII, a color sensor wavelength measurement device, and some laser stabilisation techniques. The IPSII project eventually got to the point where Dr. Durfee and I felt it was worth pursuing in earnest, and made it the focus of my own research as well. The color sensor project has produced a few senior theses and one published paper, which I have included in Appendix A.3.

Our work with IPSII originated from a term project I did for a medical engineering class I took with Dr. Neal Bangerter (then of the Electrical Engineering department at BYU). The class allowed us to come up with our own idea for a project, and I chose to simulate the process used in magnetic resonance imaging with an optical analog using front or back projection and a single pixel detector (we have since learned that my project was nearly identical to work published in Nature Communications a couple years previously [7]). After the class was over I talked to my advisor about the possibility of doing the same thing with interference patterns, and we were able to come up with a practical design to do so, leading to the work that is the main topic of this dissertation.

The IPSII project has required a significant amount of work to get up and running. I surveyed the literature, went to a couple conferences and talked to researchers in similar fields, and worked out the theory for what we conceptually wanted to do. I designed and built motorized mirrors with

3D printed parts (Appendix B) to give us the numerical control we needed. I wrote all the software and drivers necessary to control the experiment and take the data, as well as software to analyze the data, including developing a digital lock-in method that could function with a non-linear phase ramp (i.e. a frequency varying reference signal). I wrote and submitted our first paper on the subject (which is currently under review), and am now mentoring several undergraduate students who are working on related projects.

We have only recently gotten to the point in our IPSII related research where we are getting publishable data, and our first paper is in review. We have outlined and are now writing a second paper on phase distortions, and the potential use of distortions to reduce the required dynamic range or enhance compressive sensing. We already have the theory, simulations and data to back this paper. We have outlined a third paper on the effects of k-space position error for which we have theory and preliminary data. We have outlined a fourth paper on alias unwrapping using multiwavelength data for which we already have data, but are lacking the analysis and rigorous theory. We have plans for a fifth paper we would like to do on the potential use of IPSII for complex imaging (transmission holography), as well as some preliminary data demonstrating proof-of-concept.

1.8   Dissertation Overview

In Chapter 2 I will give a conceptual description and a signal equation describing IPSII in a general way. I will then present various experimental designs we have used or proposed for taking advantage of the possible forms of imaging apparent in the signal equation, as well as results from various experiments we have performed with MAS-IPSII.

In Chapter 3 I will derive the signal equation, demonstrate its relationship with the Fourier transform, and describe various possible imaging methods that result from it. I will also discuss potential modifications and limitations of the signal equation for various measurement purposes,

and derive some basic imaging properties.

In Chapter 4 I will discuss various practical issues facing IPSII implementations, and give full or partial solutions where available.

In Chapter 5 I will give my concluding remarks.

Chapter 2

MAS-IPSII Implementation

Our implementation of lensless IPSII is simple in concept. When two coherent beams interfere at an angle they form sinusoidal fringes, which are used to illuminate an object (see Fig. 2.1). A detector then measures the light reflecting off, or transmitting though the object, effectively measuring a single spatial frequency component of the object. This signal must be measured at multiple phases, which can be done by making multiple discrete measurements (as is typical in SIM), or by recording the signal while sweeping the phase (typical to other IPSII based methods). The resulting amplitude and phase measurements effectively gives one complex pixel of the transformed object image in k-space, the alternate basis of the structured illumination. One just needs to measure enough pixels and do an inverse transform to get an object space image.

More formally, IPSII can be summarized by a simple equation in the form of a Fourier transform that describes the signal $\widetilde{s}$ from an optical detector,

$$\widetilde{s}(k_x, k_y) = \int_{-\infty}^{\infty} \int_{-\infty}^{\infty} M \widetilde{A}_1 \widetilde{A}_2^* e^{i(k_x x + k_y y)} dx dy. \tag{2.1}$$

where $M(x, y)$ describes the object (e.g. the transmission or reflection profile), $k_{x,y}$ are the spatial frequencies of the interference pattern, and $\widetilde{A}_{1,2}$ describe the complex profiles of the beams. The function $\widetilde{s}$ is a time independent complex function whose modulus and phase represent the amplitude
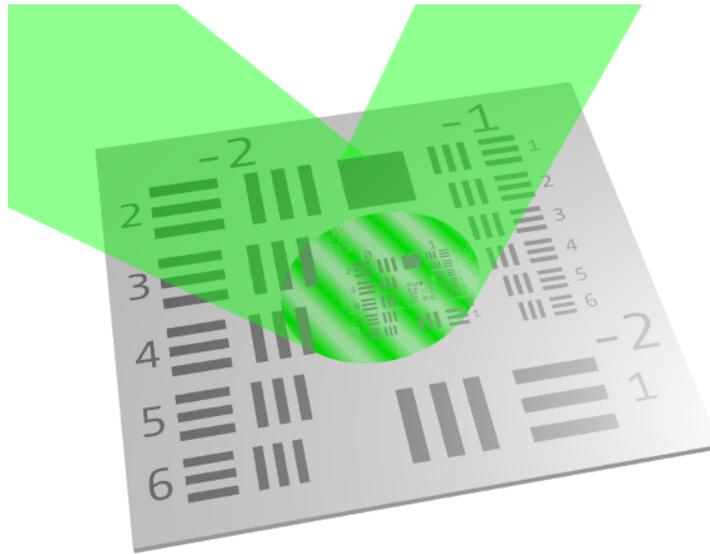
Figure 2.1 Illustration of IPSII. Two beams overlap to form a interference pattern on an object.

and phase of a time dependent, oscillating, real valued signal *s*.

The important thing to note is that this equation is just a Fourier transform of the object multiplied by the profile of the illumination, and evaluated at (k_x, k_y). To image an object we simply need a way to scan the angle between two illuminating laser beams, scan the phase between the two beams (causing the interference pattern to oscillate), and measure $\widetilde{s}$ at each point on a grid in k-space. The object image may then be obtained by transforming the k-space data back into object space. A full derivation of the signal equation, and a discussion of its implications are given in Chapter 3.

2.1 MAS-IPSII Design Requirements

While lensless IPSII is simple in concept, there are some challenges in implementation. Attempting pure SI imaging with interference patterns—without augmenting with any traditional imaging methods—means that we need to measure the signal from at least one pattern per pixel (barring the

use of compressive sensing techniques). For reasonable, useful images this means making tens of thousands of measurements, at least. For this we need some way to continuously vary the angle of the two beams.

Past IPSII implementations have mostly used a fixed set of angles, due to the difficulty in physically altering the interference angle. These methods, however, are capable of only a small number of IPSII measurements, are not easily scalable to higher pixel counts, and thus require augmentation with traditional imaging techniques. Standard SIM for example, could be viewed as an IPSII technique limited to 4 pixel images. However, by combining it with a traditional imaging objective and detector, each pixel of the traditional image is broken up into 4 new pixels, thus the factor of two resolution improvement.

The multi-beam approach employed at MIT [18] took this further by having 31 fixed beams, with 62 unique pairings. Such a setup could, in principle, perform lensless imaging—but would be limited to a 62 pixel image, which is roughly 8 pixels square (not very useful by itself). Even if the beam arrangement could be optimally designed so that every possible beam pair would produce a unique and useable signal, at best 31 beams could produce about a 21x21 pixel image—which is still not very useful. Generally, such a multi-beam approach is limited to, at best, $N(N-1)/2$ pixels, where N is the number of beams (and proportional to the number of optics). As such, this method is not scalable to higher pixel counts, which is why this approach (and SIM) must be augmented by traditional imaging methods.

The obvious solution to the scaling problem with IPSII is to use a method that scans the angle of the beams continuously, rather than using a fixed number of beams at different angles. This is itself a challenge, because the angle between the beams must be scanned while keeping the beams overlapping. For example, DEEP and $\mathscr{F}$-basis [19–21] use an AOM to scan angles, and CHIRPT accomplishes a similar feat using a custom spinning diffraction grating [24, 25], but all of these produce diverging beams, which must be brought back together with a lens. However, as noted in
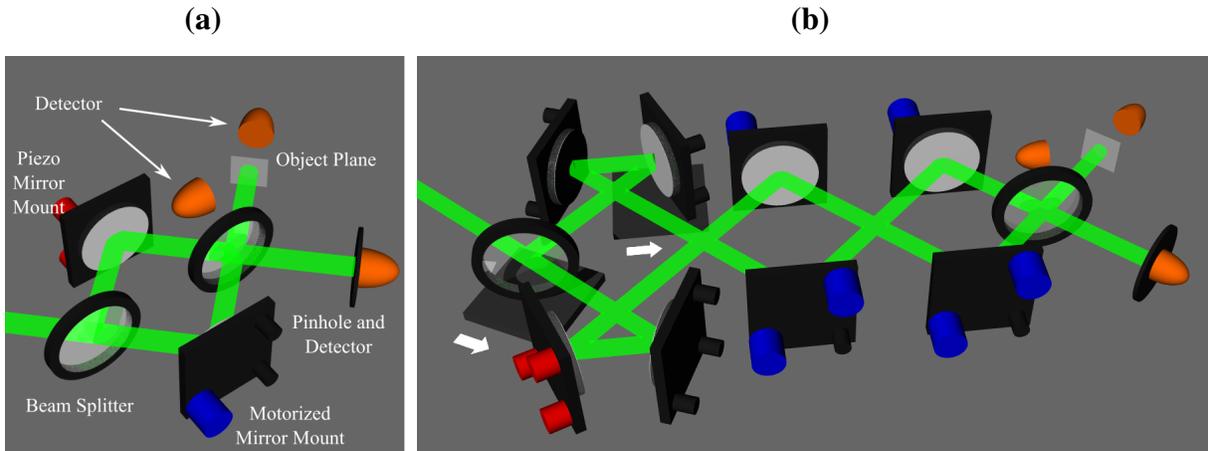
Figure 2.2 Renderings of Mach-Zehnder interferometers used to for imaging. Left: working setup with minimal set of optics—see Section 2.2. Right: a more complex optical layout for an interferometer with better beam control and path-length tuning—see section 2.3.

the introduction, this use of a lens in the pattern formation imposes many of the same limits on this form of IPSII as other lens based imaging methods.

Our work attempts to solve this problem without use of a lens, acousto-optics or fixed beams, and in a way that can scale to arbitrary pixel counts. To do so we mechanically scan the angle between interfering beams using motorized mirrors in optical layouts based on a Mach-Zehnder interferometer (see Fig. 2.2).

Another necessary aspect of IPSII is the phase measurement. As mentioned, this may be done discretely or continuously as the phase is scanned. Other IPSII methods (aside from SIM) typically do this by offsetting the frequency of the two beams (equivalent to a phase sweep) with acousto-optics. This makes sense because they typically already use the acousto-optics to split the laser and scan beam angles. It also allows for large frequency offsets, which means individual measurements can be made very quickly. On the other hand, acousto-optics are in many ways even more restrictive than lenses. They are not available at extreme wavelengths, are very limited in size, introduce distortions in the laser wavefronts and increase the cost of the imaging system.

We sweep the phase using piezo mounted mirrors. The main downside of this approach is the effective frequency shift is much smaller which slows down the data taking process. However, it avoids the need to introduce any further optics in the path of the lasers, making it more widely applicable since the only requirement is a reflective surface.

As the phase is swept, the signal from the object detector will oscillate. The phase of this oscillation (relative to the phase ramp) is the most crucial piece of information measured. However, in the optical layouts we use to scan the beams, the phase of the interferometer is effectively randomized with each angle change due to large (relative to the wavelength) changes in the optical path-length with the movement of mirrors. Phase drifts of the interference pattern resulting from frequency drift of the laser, thermal expansion of the apparatus, mechanical drift, etc. over the course of imaging would also be a problem unless an exceptionally stable laser, optical system and environment were used. These problems combine to make the directly measured phase of the oscillation signal meaningless without some sort of reference.

The easiest way to solve the problem of phase drift and randomization is to directly measure the phase of the interference pattern relative to some fixed point in object space. One way to do so would be to image the pattern and calculate its phase—but that would defeat the whole point of lensless imaging. Our solution is to use a pinhole (or a slit for 1D imaging) placed in the interference pattern of the second output of the interferometer (see Fig. 2.3). As the fringes are scanned across the pinhole, a detector placed behind the pinhole measures an oscillating signal that can be used as a phase reference. The pinhole just needs to be smaller than any fringes which are used during the full scan. We have used 1-15 μm pinholes (or slits) in our imaging setups.
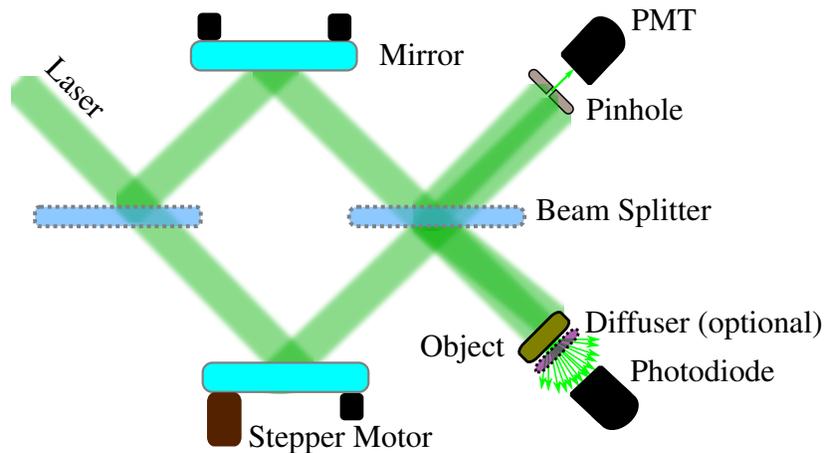
Figure 2.3 Simple 1D MAS-IPSII implementation using a single motorized axis on a mirror in a Mach-Zehnder interferometer to scan the angle between output beams.

2.2 Simple MAS-IPSII Interferometer

Our first experiments were done with a simple Mach-Zehnder interferometer (see schematic in Fig. 2.3). While there are some obvious problems with this design (discussed below), it serves as the basis for other designs we have implemented and considered, and as such is worth consideration first. In this design only two flat mirrors and two beam splitters are required. The angle between beams is swept a with a motorized adjuster on one mirror, and the phase is swept by ramping the voltage on the piezo mounted mirror. In our first implementation only one mirror axis was motorized, as we only used this setup to conduct proof of concept 1D tests. Extending to 2D would be a simple matter of motorizing the second mirror axis.

Making a 1D 'image' follows the process in Fig. 2.4. First, a linear ramp is applied to the piezo mounted mirror, causing a corresponding linear ramp of the phase of the interference pattern. The result is fringes that appear to be sweeping across the object (when slowed down sufficiently to see by eye). While the phase is swept the signal from photodetectors on the object and the slit are recorded. The object signal is compared to the slit signal to extract the amplitude and phase relative to the reference. The mirror is then moved to the next angle, and the process repeats. When finished,

an inverse Fourier transform is applied to the data.
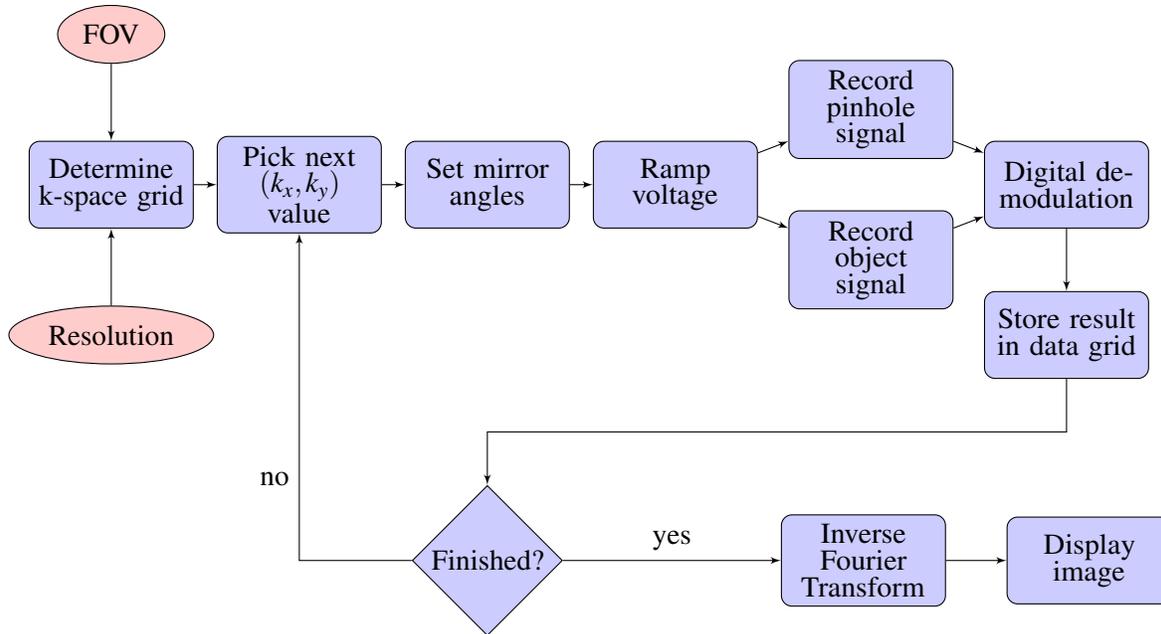
Figure 2.4 IPSII Process

The pinhole reference signal must be combined with the object signal to produce a useful k-space data point. This is done with a digital quadrature demodulation (also known as lock-in detection) process.

This process could also be done with analog electronics, which would greatly reduce the post-process computation required, though doing so would require a faster phase sweep than our current equipment allows for. See Fig. 2.5 for examples of the raw data and the process of reconstructing a 1D image (the shadow of a pair of wires).

The problem with this simple setup is that only the angle of the beams can be controlled independently. Even if both mirrors were motorized, changing the angle between beams also moves the beams off the object and each other. For low resolution imaging this is not a problem, since only small angle changes are required. However, if smaller beams, long working distances or higher resolutions are desired, the simple setup is not a good design.
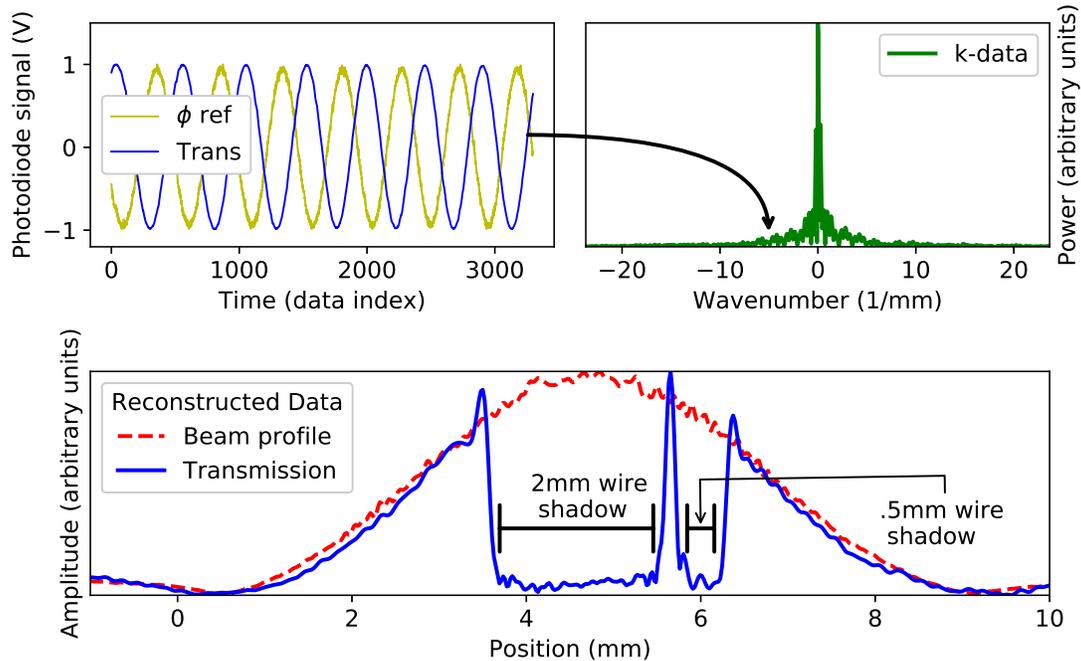
Figure 2.5 Simple 1D demonstration of IPSII data taking and analysis. Top left: raw data from slit detector, and detector behind object. Top right: power spectrum of resulting 1D k-space data. Bottom: 1D object space reconstruction, showing the laser beam profile with the shadow of two wires, one 2mm wide and the other .5 mm wide.

There are a couple ways the simple Mach-Zehnder layout could be modified to be more generally useful. One of them is to add an extra motorized mirror in each arm of the interferometer, so that the angle and position of each beam can be controlled. This is the route we took (see Section 2.3). Another method would be to motorize the beam splitters in addition to the mirrors. Each beam (considered at either output) is reflected off one beam splitter and one mirror, so there are enough degrees of freedom to control the position and angle of each beam at one of the interferometer outputs (which guarantees the beams in the other output will also be aligned). This method would be a little more difficult to implement in practice, since the electronics used to motorize the beam splitter would need to be kept out of the beam path. However, it would also require that each beam interacts with only three flat optics, which might make it a more attractive option when working
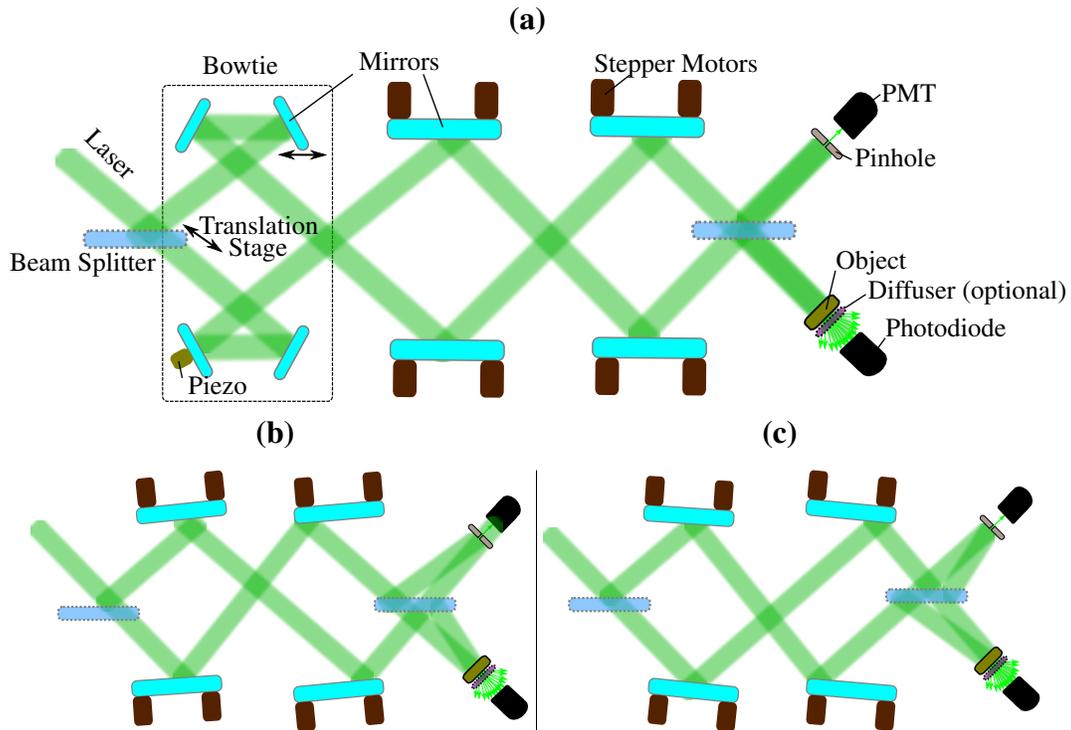
Figure 2.6 Two-stage interferometer. This implementation adds another pair of mirrors to keep the beams centered during the angle scan, and adds a bowtie configuration, [only shown in (a)] to help balance the path lengths. The arrows in the bowtie indicate translation stages. The interferometer is shown with $\theta = \phi = 0$ in (a). The limits of its angle range are shown in (b) and (c), and correspond to the positive and negative k-space measurements for the maximum spatial frequency magnitude that can be measured.

with extreme wavelengths, or in compact devices.

2.3 Two-Stage Interferometer

Our second generation interferometer, the one we have used for most of our experiments, is the

Mach-Zehnder interferometer illustrated in Fig. 2.6. It has pair of mechanically scanned mirrors

in each beam to allow control of both the angle and position of the beams. This allows us to keep

the beams overlapping, even while scanning to larger angles. Having motorized mirrors in both

arms also allows us to do symmetric scans. All of this allows for larger angles and correspondingly

higher resolution imaging compared to the first-generation interferometer.

Balancing the path-lengths of the interferometer arms is necessary if the temporal coherence length of the laser is less than the optical path-length in the interferometer (e.g. due to multi-mode operation, mode hopping or a large linewidth). We have included a 'bowtie' configuration in the design to allow the interferometer to be more easily balanced (only shown in Fig. 2.6a). In the bowtie, translation stages are placed under the beam splitter and the first mirror in the path of the reflected beam. The path-length is tuned by adjusting both translation stages together such that the output of the interferometer (overlap position and angle) is unaffected.

Balancing can be further simplified with proper orientation of the translation stages in the bowtie. For example, if the interferometer is aligned so that the beams reflect at 45° angles from the beam splitters and motorized mirrors, the translation stage on the beam splitter is placed at a 60° angle from the vertical, and the translation stage on the mirror is oriented parallel to the beam splitter, then an equal and simultaneous adjustment to both translation stages will adjust the path-length difference without affecting output. More generally, for any given orientation of the input beam into the interferometer, the orientation of the translation stages may be calculated, or calibrated by adjusting the relative orientation of the translation stages until equal adjustments to both do not affect the overlap of the output.

2.3.1 Geometry

The ideal geometry of the interferometer layout depends on the use case. Some key parameters, as labeled in Fig. 2.7, are the angle θ_m between the mirror normals and output beams at the $k_{x,y} = 0$ position, the distance L_0 between mirrors, the distance L_1 between the second mirror in each arm and the second beam splitter, the effective working distance L_2 from the beam splitter to the object (and pinhole), the distance $L_3 = L_1 + L_2$ between the second mirror and the object, and the diameters D_m of the mirrors and D_{BS} of the beam splitter.

The effective aperture of the device is $D_m \sin \theta_m$, and the effective numerical aperture is

$$NA_{\text{eff}} = \frac{1}{\sqrt{\left(\frac{2L_3}{D_m \sin \theta_m}\right)^2 + 1}}.$$ (2.2)

This assumes the beamsplitter is sufficiently large ($D_{\text{BS}} >= D_m L_2 / L_3$), so that the mirror is the limiting aperture. To maximize the numerical aperture, it may be desirable to make θ_m as close to normal incidence as possible, while avoiding clipping of the beams going to the object (or pinhole) by the mirrors on the opposite side of the interferometer.

Calibration

Ideally, maintaining proper alignment during the angle scan is a simple matter of moving the first mirror in each arm by some fraction of the movement of the second mirror. This fraction is half the ratio of the distance between the second mirror and the object to the distance between the first and the second mirror. The resulting change in angle of the beam is the sum of the two mirror angle adjustments. In practice, it is useful to perform a calibration step to determine this ratio experimentally, and also to correct for non-ideal kinematic coupling in the mirrors (for example,
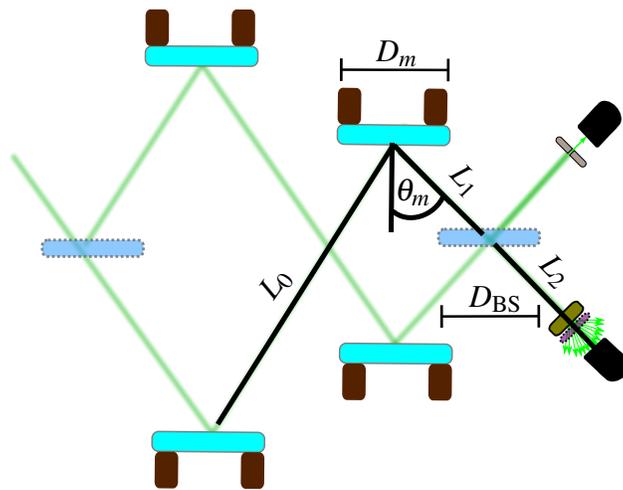
Figure 2.7 Key parameters of the geometry in the two-stage design.

imperfect isolation of vertical and horizontal angle changes). In this case, given an angle of the first mirror $(\theta_{H1}, \theta_{V1})$ then the angle of the second is set to

$$\begin{pmatrix} \theta_{H2} \\ \theta_{V2} \end{pmatrix} = M \cdot \begin{pmatrix} \theta_{H1} \\ \theta_{V1} \end{pmatrix}, \tag{2.3}$$

where

$$M = \begin{bmatrix} m_{11} & m_{12} \\ m_{21} & m_{22} \end{bmatrix} \approx -2\frac{L_3}{L_0} \begin{bmatrix} 1 & 0 \\ 0 & 1 \end{bmatrix}. \tag{2.4}$$

Calibration is the process of determining the exact m_{ij} coefficients of the matrix M.

A simple procedure to calibrate the interferometer to a particular working distance L_3 (somewhat analogous to adjusting a focus) is as follows. An iris placed before the interferometer is used to make the beams as small as possible at the interferometer output. A marked piece of paper or an aperture is placed at the desired working distance and beam position. Then the first mirror is adjusted by some random amount, and the second mirror adjusted to bring the beam back to the marked location. This is repeated for as many measurements as desired, but at least two such points must be measured if assuming ideal mirrors mounts (i.e. mounts with no cross talk between the horizontal and vertical axis), and at least 4 measurements must be made when correcting for non ideal mirrors (i.e. allowing m_{12} and m_{21} to be non-zero). Then the m coefficients are determined with a simple set of linear regressions on the resulting data (see Appendix C). This process is done for both arms, so two matrices M_1 and M_2 are recorded.

Ultimately, the calibration needs to be used to set an arbitrary angle $(\theta_{HB}, \theta_{VB})$ of the beam from the normal at the object plane. To do so, the mirrors in the interferometer are set according to

$$\text{Mirror 1 adjustments:} \quad \begin{pmatrix} \theta_{H1} \\ \theta_{V1} \end{pmatrix} = (M+I)^{-1} \cdot \begin{pmatrix} \theta_{HB} \\ \theta_{VB} \end{pmatrix}, \tag{2.5}$$

$$\text{Mirror 2 adjustments:} \quad \begin{pmatrix} \theta_{H2} \\ \theta_{V2} \end{pmatrix} = (M^{-1}+I)^{-1} \cdot \begin{pmatrix} \theta_{HB} \\ \theta_{VB} \end{pmatrix}. \tag{2.6}$$
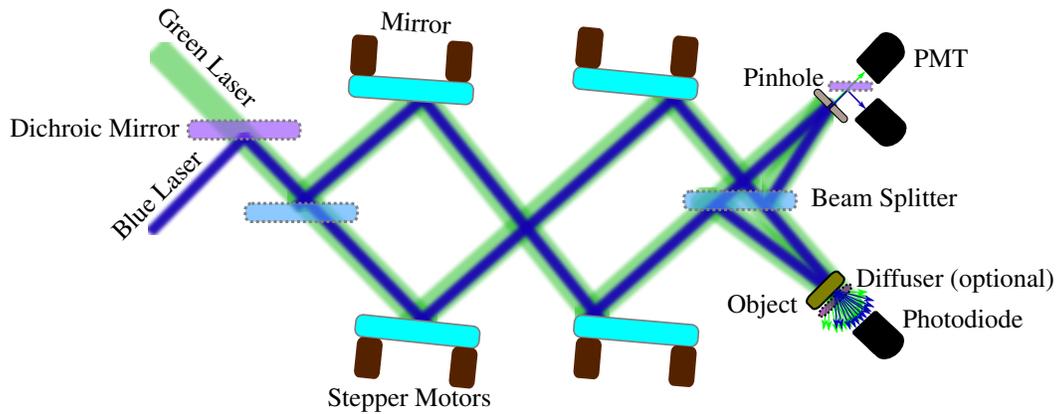
Figure 2.8 Multi-wavelength setup. Multiple wavelengths can be used simultaneously by overlapping beams before the interferometer and separating out the phase reference signals as shown (note the two PMTs after the pinhole).

This is done for the mirror pair in each arm using the *M* matrix for that arm and the desired angle for that beam. The resulting net interference angle is then just the difference between the two beam angles.

2.4   Dual Wavelength Setup

Another idea we have tested is dual-wavelength imaging. This principle could easily be extended to full color RGB imaging (i.e. triple-wavelength imaging), or more generally, to multispectral imaging with any number of wavelengths. Our layout for dual wavelength imaging, as shown in Fig. 2.8, is mostly the same as the two-stage interferometer described in Section 2.3. As long as the beam-splitters and mirrors have broadband coatings, any number of beams at different wavelengths can be used simultaneously in the interferometer. However, you then need a way to separate out the signals from the individual wavelengths.

The most straightforward way to do multi-spectral imaging would be to use dichroic mirrors to separate out the signals after the pinhole and object, and have a separate detector for each. However, doing so after the object is tricky because ideally we want to capture as much of the light passing

though the object as possible. It turns out that having a separate object signal is not really necessary, however, because during the phase ramp each wavelength will oscillate at a different frequency. We can separate the signals during processing. However, we still need a phase reference for each signal.

We believe it may be possible to also do away with the separate phase reference for each signal, since the different phase changes result from path-length differences, which are common to all wavelengths used in the interferometer. If the interferometer is sufficiently well balanced and each laser used is stable enough that phase drift resulting from frequency drifts can be ignored, then one reference should be good enough to derive a phase reference for all other wavelengths. In this case, only one reference detector would be used, with a narrow line filter used to filter out all but one of the wavelengths in the interferometer. Another possibility would be to measure all reference signals with one detector, and then digitally separate the different frequency components.

2.5   High NA Imaging

One of the main problems with the interferometer–based setups is that they limit the effective numerical aperture. This limit is much less constraining than the limit on a traditional lens based system at large working distances, since the NA is set by the size of a flat mirror or beam splitter rather than the size of a lens (see Section 2.3.1). However, the aperture of MAS-IPSII need not be limited at all by the size of any individual optics.

One potential method of decoupling effective NA from optic size is shown in Fig. 2.9, in which motorized mirrors would move along tracks. The effective NA of such a system would depend on the working distance and the track length, such that very high numerical apertures could easily be obtained even at relatively large distances (compared to traditional microscopes or cameras). Either the tracks or the object would also need to be rotated about the imaging axis to do 2D imaging.

The problem with such a system is that the angle cannot be continuously changed through zero,
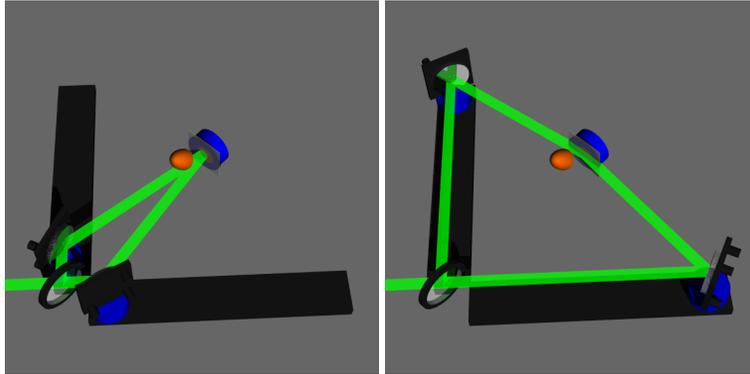
Figure 2.9 Proposed setup for high NA imaging. Two mirrors would move along tracks, and rotate to keep beams centered on object. The effective NA depends only on the length of the tracks and distance to the object.

but is instead limited to some minimum angle θ_{min}. This means that some values in the center of k-space cannot be reached, and 'negative' k-space values can not be measured. However, the negative k-space values only add information when measuring a complex function (see sections 3.5 and 4.2). Also, it turns out that the $k_{x,y} = 0$ (or 'DC' term), could also be measured in other ways (e.g. it could be calculated from the DC offset in the signal of every other measurement), so if the inaccessible k-space region is smaller than the discrete spacing, such that

$$\sin \theta_{min} \leq \frac{\lambda}{2 \, n \, \text{FOV}}. \tag{2.7}$$

then no information is lost. Even if some data is missing, the lack of data in the center effectively would act as a high pass image filter (similar to that used in edge detection), so in many cases this may not be a problem.

2.6 Implementation Details

Most of our work has been done with a particular experimental implementation based on the dual wavlength two-stage interferometer design discussed above. We used standard, easily obtainable optical components, lab electronics, 3D printed parts, and built our own motorized mirrors (see

Appendix B) to get the range and precision we need, and to save on cost. A parts and price list is given in table 2.1.

Part	Number	Price	Item Sub	Description
NewFocus U200-A	2	$141.00	$282.00	Mirror mounts without actuators
NewFocus U200-A-LH	2	$141.00	$282.00	Mirror mounts without actuators
NewFocus AJS254-0.5H-NL	8	$55.00	$440.00	Ultra-fine Hex Adjustment Screw, 254 TPI
Thorlabs BB2-EO2	4	$152.00	$608.00	2in mirrors
3D printed parts	4	~$10.00	$40.00	Printed pieces needed for one mirror
28BYJ-48 ULN2003	2	$13.00	$26.00	Stepper motor (5 pack) with driver kits
Mirror power supply	1	$12.00	$12.00	A variable switching supply works well
Wiring	1	$15.00	$15.00	4-pin motherboard header cables
Thorlabs KM200	2	$80.00	$160.00	Kinematic mounts for beamsplitters)
Thorlabs Piezo	1	$180.00	$180.00	Piezo for phase scan
Viking VP7210-00B150G	1	$550.00	$550.00	Piezo Driver
Laser	1	$20.00	$20.00	Inexpensive green hobby laser
BeagleBone Black rev c	1	$57.00	$57.00	Mini linux computer with lots of output pins
Labjack T7	1	$429.00	$429.00	Data aquisition unit
Thorlabs P2H	1	$129.00	$129.00	Pinhole
Thorlabs FDS1010	1	$54.00	$54.00	Detector for object signal
Pinhole detector	1	~$500.00	$500.00	931B PMT + HV Power supply
Total			$3,784.00	

Table 2.1 Price list for parts needed for single wavelength interferometer. Equivalent parts are listed in some cases (where the part we used is unavailable), and estimates, where exact prices were not available, are indicated with $\sim$. Common lab elements such as posts, mounts, screws, etc. are not included. We used a more expensive lab laser that we had on hand, but for our purposes an inexpensive green laser should work just as well.

2.7   Results

We have been able to successfully image with a working distance of about 10 cm, resolutions of up to 2.5μm and a FOV of up to 3 mm. We have not imaged at maximum resolution and maximum FOV simultaneously, however, due to current limitations on imaging speed, though there is nothing (other than time constraints) that would prevent us from doing so. We have performed various imaging tests with a USAF1951 resolution test target, for which the widths of the lines are shown in Table 2.2. See Fig. 2.10 for various images of the resolution test target, and Fig. 2.11 for an image

of another, custom made, test target. Also see Fig. 2.12 for an example of imaging of a biological specimen. In these test images you can see various artifacts (ghosting, blurring in areas, etc.). Most of these issues are understood, and result from various limitations in our current hardware that will be corrected for in future iterations of our designs. These issues, and potential solutions and workarounds for them are discussed further in Chapter 4.

Imaging artifacts aside, note that the observable resolution matches the expected resolution (i.e. the pixel size, as determined by the discrete Fourier transform) in each image. All images are included in lossless PNG format, so you can zoom in and see the individual pixels, as long as your document viewer does not smooth (interpolate) images, and have an unedited version of this document.

	Group Number							
Element	2	3	4	5	6	7	8	9
1	125.00	62.50	31.25	15.63	7.81	3.91	1.95	0.98
2	111.36	55.68	27.84	13.92	6.96	3.48	1.74	0.87
3	99.21	49.61	24.80	12.40	6.20	3.10	1.55	0.78
4	88.39	44.19	22.10	11.05	5.52	2.76	1.38	0.69
5	78.75	39.37	19.69	9.84	4.92	2.46	1.23	0.62
6	70.15	35.08	17.54	8.77	4.38	2.19	1.10	0.55
	Line Widths (μm)							

Table 2.2 Line widths for USAF 1951 Resolution test target. Resolution limit is determined by finding the first element in an image where individual lines are no longer distinguishable, and looking up that group on the chart.
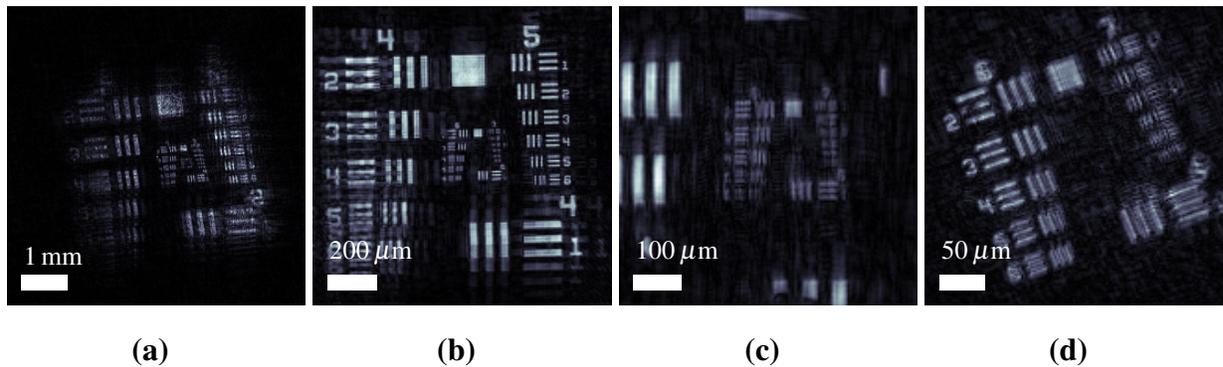
Figure 2.10 Object image reconstructions from various scans of a Negative USAF1951 Resolution Test Target.
(a) Groups 2 and 3. FOV: 6.5x6.5 mm — pixel size: 24 μm — 271x271 pixels
(b) Groups 4 and 5. FOV: 1.2x1.2 mm — pixel size: 6.3 μm — 191x191 pixels
(c) Groups 6 and 7. FOV: .6x.6 mm — pixel size: 4.2 μm — 151x151 pixels
(d) Groups 6 and 7. FOV: .43x.43 mm — pixel size: 2.0 μm — 161x161 pixels
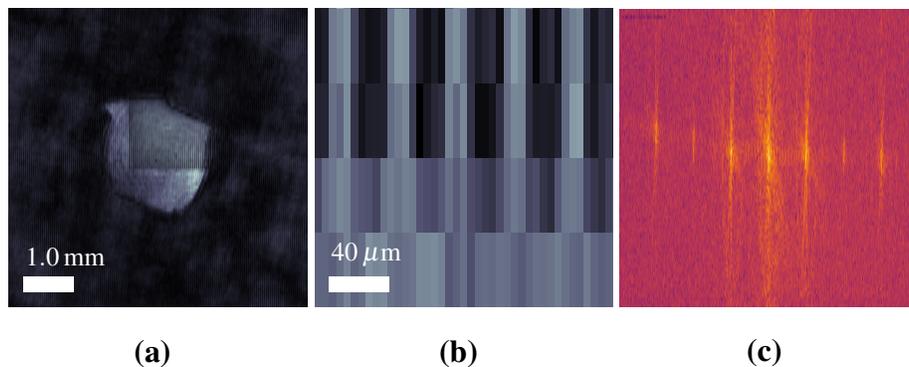
Figure 2.11 A scan of a custom target for testing resolution in 1D, containing 20μm lines. The scan was done with a target resolution (pixel size) of 5.0x66.65 μm.
(a) FOV: 6x6 mm, 1201x91 pixels. The corner of the target is visible through an aperture made by poking a hole in aluminum foil (necessary to prevent aliasing). Note that the image has a much higher x-resolution than y-resolution (pixels are not square).
(b) Zoomed area (41x4 pixels) of the image at the tips of a few of the lines, showing the pixel width of lines, and the difference in resolution in the *x* and *y* dimensions (the rectangular pixels).
(c) Absolute value of k-space data.

(a)

(b)
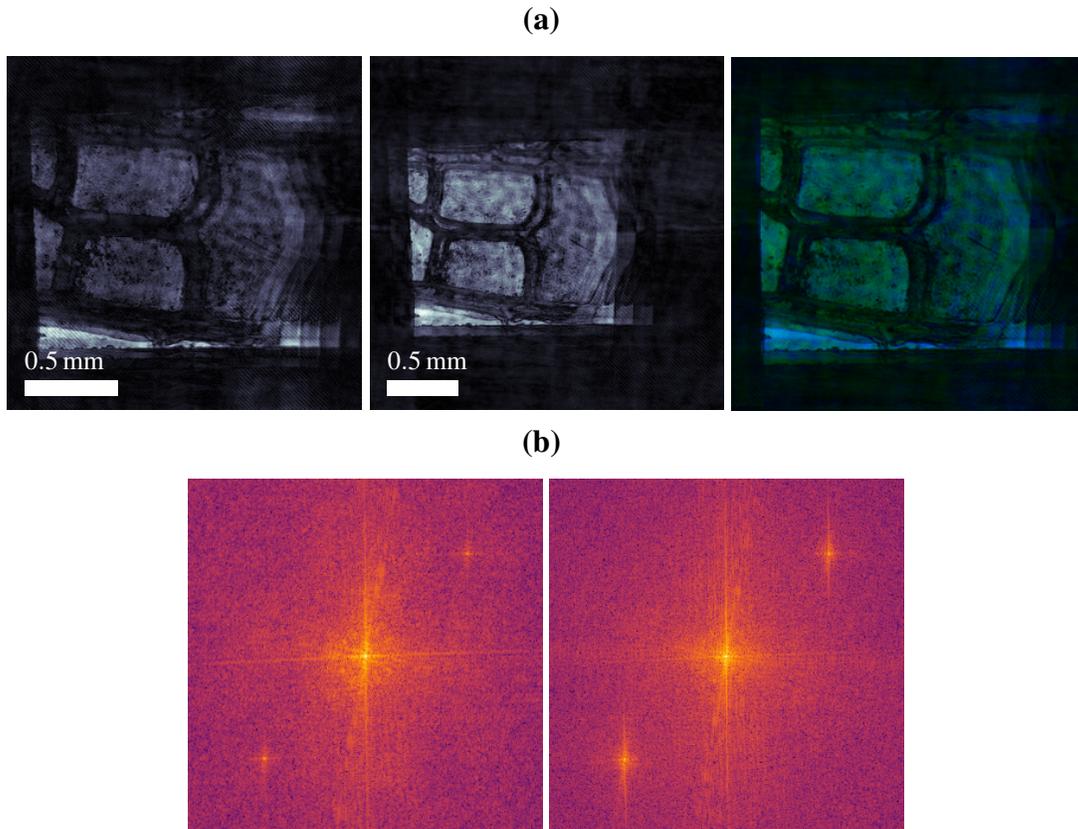
Figure 2.12 Dual–wavelength image of a grasshopper wing. The FOV and resolution are different because they are both wavelength dependent, but both sets of data were taken in the same mechanical scan. The inverse transform results in complex data, the absolute value of which is displayed as the image.
Green FOV: 2.5x2.5 mm — pixel size: 8.3x8.3 μm — 301x301
Blue FOV: 1.9x1.9 mm — pixel size: 6.3x6.3 μm — res 301x301
(a) Left to right: image from green laser, image from blue laser, combined image. The FOV and resolution are different because they are both wavelength dependent.
(b) Absolute value of the raw k-space data for the blue (left) and green (right) images.

2.7.1   Working Distance

One of the motivations of this work (as indicated in the introduction) was to decouple working distance, resolution and optic size, especially for the purpose of ultra long working distance microscopy. The resolution of our current experimental design is still limited by optic size, though this could be avoided with a setup such as the one shown in Fig. 2.9. However, the optics in question are flat mirrors and beam splitters, making large apertures much easier to obtain than large aperture high NA lenses.

While we hope to explore the use of MAS-IPSII for long working distance microscopy further in future efforts, our current device is already close to the effective aperture limit of high resolution commercial devices. This is shown in Fig. 2.13, where a set of commercial objectives are plotted according to their resolution (assuming 532 nm illumination) and working distance, along with the demonstrated and theoretical maximum working distance of our current device. Note that high NA solutions are not generally available with effective apertures of more than 40 mm, though research into methods of extending these limits is ongoing (including previously mentioned synthetic aperture techniques, as well as large physical lens solutions [28]). Even with our current setup, effective apertures of over 50 mm could easily be obtained using larger (but still readily available) optics.
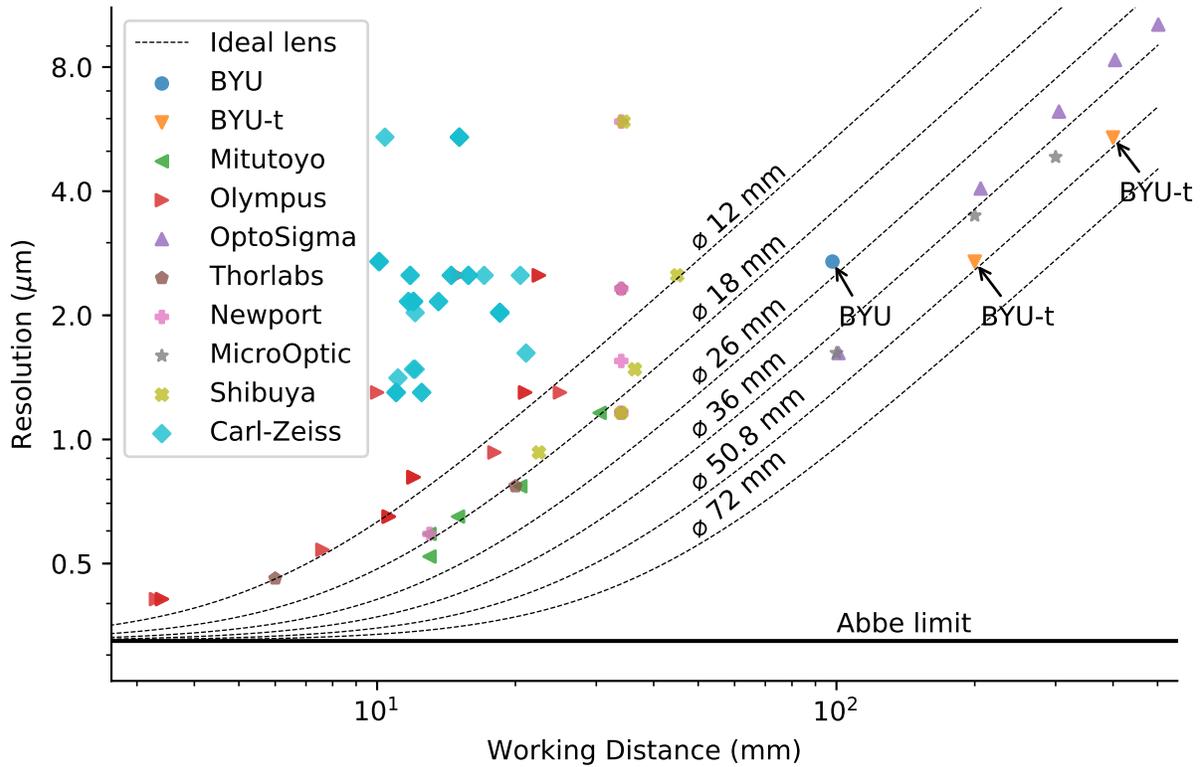
Figure 2.13 Working distance of MAS-IPSII compared to commercial long working distance objectives. Each objective in a list of microscope objectives advertised as 'long working distance' (collected by hand) is plotted as a symbol (corresponding to the commercial brand of the objective) at a location corresponding to its maximum working distance and its resolution at that distance (assuming 532 nm illumination). Also plotted are various curves corresponding to ideal lenses of a given diameter. These curves show the maximum resolution for an ideal lens at a given working distance and aperture. The Abbe resolution limit is indicated with a horizontal line (i.e. for NA=1). The current equivalent resolution and working distance of our MAS-IPSII device is labeled 'BYU'. Two points labeled 'BYU-t' indicate the maximum equivalent numerical aperture our current device could obtain in theory. Even larger effective apertures could be obtained if larger mirrors were used.

Chapter 3

Theory

In Chapter 2 I introduced a 'signal equation' in which the imaging potential of MAS-IPSII is apparent. In this chapter I will derive that equation, discuss its implications, and derive some similar equations for various experimental modifications to the basic approach described in chapter 2.

3.1   Signal Equation Derivation

In its most general form, IPSII could be done in a variety of ways. The core concept is that an interference pattern is created from more than one wave source, with some controllable variable that allows the interference to be modified. The main requirement is that the set of interference patterns that can be generated span the space in which you want to image. They do not necessarily need to be orthogonal, and in some cases do not even need to be completely known (see 3.5). Imaging could be done, in principle, in 1, 2 or 3 dimensions.

When the interference patterns are used to illuminate an object, a detector placed directly behind or at an angle in front of the object will detect a signal s, which depends on the position of the detector, the object, the form of the interference pattern and the phase of the pattern (wich is scanned in time). The goal of this section is to derive an analytical form for the signal s. To derive a useful

signal equation, I need to narrow the scope to a less general version of IPSII, and make some experimental assumptions, but I will keep the derivation as general as I believe practical to make it easier to see potential high level modifications that can be done to the experiment (as discussed in following sections).

For this derivation I will assume a 2D target and two monochromatic wave sources with the controlling variables being wavelength and angle. I also assume a small frequency offset $\Delta\omega$ between the sources. The results may, with some restrictions, be extended to 3D and to multi-spectral sources (see sections 3.1.1 and 4.6). Use of more than 2 sources simultaneously, as has been done in some related cases [17, 29] also could have several benefits, but I leave this as a subject for future research.

I will assume the sources are laser beams, but the same derivation could apply to other forms of waves as well. I also assume that the wavefront features of each source are sufficiently large, in the object region, to not appreciably diffract within that region (i.e. we neglect changes in the beam profile as it propagates). Experimentally, this means the laser only needs to be collimated on the scale of the object. Depending on the desired FOV, this is a relatively non-restrictive condition and allows for beam modes with non-Gaussian shapes and phase distortions. With these assumptions, we describe the two beams as plane waves (e.g. $\exp(i\mathbf{k} \cdot \mathbf{r} - i\omega t)$) multiplied by transverse mode functions. The mode functions take the form,

$$\widetilde{A}_{1,2}(x_{1,2}, y_{1,2}) = A_{1,2}(x_{1,2}, y_{1,2}) e^{i\varphi_{1,2}(x_{1,2}, y_{1,2})}, \tag{3.1}$$

where $x_{1,2}$ and $y_{1,2}$ are the transverse beam coordinates (i.e. displacement from an axis in the beam propagation direction), the real functions $A_{1,2}$ are the transverse field amplitudes of the modes, and the $\varphi_{1,2}$ functions represent the position dependent phases of the modes.

I assume polarization vectors are all parallel and can be safely neglected, so only the electric field amplitudes are needed. The resulting description of an arbitrary laser that satisfies the conditions
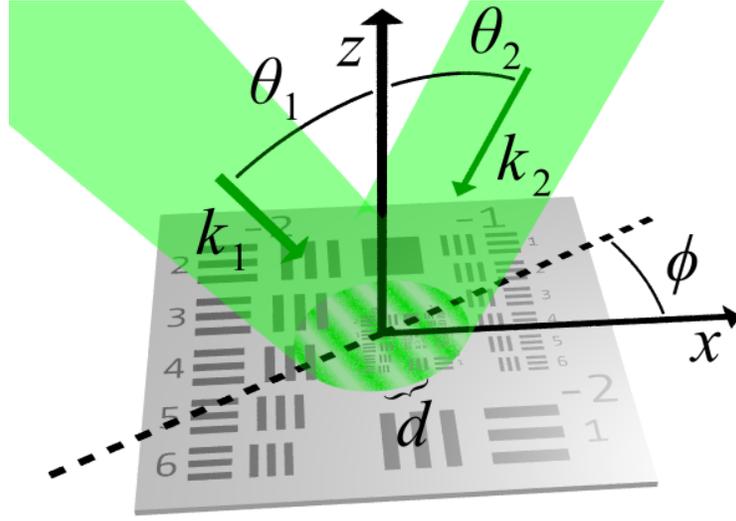
Figure 3.1 Illustration of IPSII. Two beams overlap to form a interference pattern on an object.

set above is,

$$E_1(x_1, y_1, t) = \widetilde{A}_1(x_1, y_1)e^{i\mathbf{k}_1 \cdot \mathbf{r} + i\omega t} \tag{3.2}$$

$$E_2(x_2, y_2, t) = \widetilde{A}_2(x_2, y_2)e^{i\mathbf{k}_2 \cdot \mathbf{r} + i(\omega + \Delta\omega)t}, \tag{3.3}$$

where $\mathbf{k}_{1,2}$ are the individual beam wave vectors,

$$||\mathbf{k}_1|| = ||\mathbf{k}_2|| = k_l = \frac{2\pi}{\lambda}. \tag{3.4}$$

The beams are assumed to come in at symmetric angles to the object (non-symmetric angles are discussed in Section 3.5), such that both $\mathbf{k}_{1,2}$ vectors are at an angle θ from the object normal, and oriented at an angle ϕ and $\phi + \pi$ around the object normal (see Fig. 3.1). I also assume that the two waves always overlap on the object such that $x = y = 0$ at the same point in space where $x_1 = y_1 = 0$ and $x_2 = y_2 = 0$. For small beam angles, this is true for all coordinates (not just the origin), such that $x \approx x_1 \approx x_2$ and $y \approx y_1 \approx y_2$ everywhere in the object plane. The intensity of the interference

pattern created by the two overlapping waves can then be calculated on the plane of the object as

$$
\begin{aligned}
I(x,y;k_x,k_y) &= \frac{\varepsilon_0 c}{2}\left(A_1^2 + A_2^2 + 2\,\mathrm{Re}\left\{\widetilde{A}_1\widetilde{A}_2 e^{i(\mathbf{k}_1\cdot\mathbf{r}-\mathbf{k}_2\cdot\mathbf{r}-\Delta\omega\, t)}\right\}\right) \\
&= \frac{\varepsilon_0 c}{2}\left(A_1^2 + A_2^2 + 2\,\mathrm{Re}\left\{\widetilde{A}_1\widetilde{A}_2 e^{i(k_x x + k_y y + \Delta\omega\, t)}\right\}\right),
\end{aligned}
\tag{3.5}
$$

where $k_x = 2k_l \sin\theta\cos\phi$ and $k_y = 2k_l \sin\theta\sin\phi$. Note that the 'intensity' of a field E, as I use it in this document, is just defined as $I = \varepsilon_0 c E E^*/2$, which is proportional to the square of the amplitude of the oscillating field, time averaged on time scales on the order of $1/\omega$ or longer, but notably *not* on time scales of $1/\Delta\omega$, which is assumed to be much greater. The fringe spacing of the interference pattern (ignoring any contributions from $\widetilde{A}_{1,2}$) is given by

$$
d = \frac{\lambda}{2n\sin\theta} = \frac{2\pi}{\sqrt{k_x^2 + k_y^2}},
\tag{3.6}
$$

When this pattern is used to illuminate an object, some form of interaction modifying the field amplitude or intensity will occur. This interaction is described by a complex amplitude function $m(x,y)$, which would describe either the transmission or reflection of the object in the direction of the detector. For example, if a detector placed behind the object is sufficiently large, then m is equivalent to the amplitude transmissivity of the target, and $M(x,y) = m(x,y)m(x,y)^*$ is the intensity transmission of the object, such as what you would measure with a conventional back illuminated microscope. In the case of interactions best described directly in terms of intensity, such as a fluorescent target, or diffuse reflection, the object is better described directly as a real function $M(x,y)$ giving the proportional amount of intensity incident on a point that is sent in the direction of the detector. For example, $M(x,y)$ would be proportional to the image taken by a conventional camera positioned at the same spot as the detector, if the object were uniformly illuminated.

The signal s on the detector is proportional sum of the intensity of light coming from different points in the image plane. In the case of a complex object m, the object must be multiplied by the electric field first, and then the intensity is calculated and summed,

$$
s(k_x,k_y,t) \propto \int_{-\infty}^{\infty}\int_{-\infty}^{\infty} |m(x,y)E_1(x,y) + m(x,y)E_2(x,y)|^2 dx\,dy
\tag{3.7}
$$

however, since *m* is common to both terms *in this case* we can calculate its absolute value independently, and the result is just the product of *M* and *I* (see Sections 3.5 and 3.6 for modifications where this is not the case). This is also what we get directly if we start with an intensity interaction *M*. So, in either case, the signal is

$$
\begin{aligned}
s(k_x, k_y, t) &\propto \int_{-\infty}^{\infty} \int_{-\infty}^{\infty} M(x,y) I(x,y;k_x,k_y;t) \, dx \, dy \\
&= 2 \operatorname{Re} \left\{ e^{i \Delta \omega \, t} \int_{-\infty}^{\infty} \int_{-\infty}^{\infty} M \widetilde{A}_1 \widetilde{A}_2^* e^{i(k_x x + k_y y)} \, dx \, dy \right\} + C(A_1, A_2).
\end{aligned}
\tag{3.8}
$$

where *C* is a constant in time. Note that for brevity I have stopped specifically calling out the spatial dependence of *M* and $\widetilde{A}_{1,2}$.

The last step is to model quadrature demodulation (lock-in detection) of this time oscillating signal—a process that extracts the quadrature components of a signal or, equivalently, its phase and amplitude). The result is a complex signal function, using standard phasor notation to keep track of the phase and amplitude of the signal. The demodulation is done at a frequency $\Delta \omega$, and the result is,

$$
\begin{aligned}
\widetilde{s}(k_x, k_y) &\equiv \int_{-\infty}^{\infty} \int_{-\infty}^{\infty} M \widetilde{A}_1 \widetilde{A}_2^* e^{i(k_x x + k_y y)} \, dx \, dy \\
&= \int_{-\infty}^{\infty} \int_{-\infty}^{\infty} \widetilde{M}'(x,y) e^{i(k_x x + k_y y)} \, dx \, dy
\end{aligned}
\tag{3.9}
$$

where $\widetilde{M}'(x,y) = M \widetilde{A}_1 \widetilde{A}_2^*$ represents a combination of the object and illumination profiles. For example, $\widetilde{M}'(x,y)$ represents the actual image you would get when taking a picture of the object under nonuniform lighting ($\widetilde{A}_{1,2}^*$) from the location of the detector, except that it is complex since it includes the spatial phase of the modes. However, note that the phase of the object itself was lost (Eq. 3.7-3.8).

The key thing to note in Eq. 3.9 is that it is simply the 2D Fourier transform of $\widetilde{M}'(x,y)$ evaluated at k_x and k_y, with some qualifications (see Section 3.4). Keep in mind, however, that it also represents the physical signal (e.g. voltage or current) measured on the detector, and that $k_{x,y}$ are determined by controllable experimental variables. We thus have a way to directly experimentally measure spatial frequency components (i.e. components of the Fourier transform) of the object in k-space.

3.1.1 3D Imaging

With the assumption of a weakly interacting object, the signal equation can be easily extended to 3D imaging. The interference pattern between two beams have depth, and are constant along a vector of symmetry that is the average of the two beam wave vectors. Given an angle θ_s between the vector of symmetry and some fixed axis of the object, the description of the interference pattern in 3D space could be modified to,

$$I(x,y,z;k_x,k_y,k_z) = \frac{\varepsilon_0 c}{2}\left(A_1^2 + A_2^2 + 2\operatorname{Re}\left\{\widetilde{A}_1\widetilde{A}_2 e^{i(k_x x + k_y y + k_z z + \Delta\omega\, t)}\right\}\right), \qquad (3.10)$$

where $k_x = 2k_l\sin\theta\cos\phi\cos\theta_s$, $k_y = 2k_l\sin\theta\sin\phi\cos\theta_s$ and $k_z = 2k_l\sin\theta\sin\theta_s$. This, of course, modifies the signal equation in the same way,

$$\widetilde{s}(k_x,k_y,k_z) = \int_{-\infty}^{\infty}\int_{-\infty}^{\infty}\widetilde{M}'(x,y)e^{i(k_x x + k_y y + k_z z)}dxdy. \qquad (3.11)$$

Obtaining a full 3D object image is then just a matter of filling in data with a 3D scan (i.e. scanning k_z along with k_x and k_y), and performing a 3D discrete inverse Fourier transform.

Of course, to obtain 3D information would require a way to scan θ_s, but this could be easily be done in multiple ways. For example, the object could be rotated relative to the beam scanning apparatus or vice versa. With a setup such as the interferometers described in Chapter 2, some 3D information could be obtained simply moving the mirrors asymmetrically, to change the angle of the interference patterns.

This 3D treatment depends on the assumption that the interference pattern interacting with any one point in the object will be unaffected by any other point on the object. While this is true for 2D objects, very thin or weakly interacting objects (i.e. having only a small effect on the amplitude or phase of passing light), and very sparse objects, it is obviously not true for more general objects. Shadows cast from one part of an object, for example, completely break this assumption. Even a very transparent object, though, could still have a strong affect on phase, effectively casting 'phase shadows' that also break down the assumption. It is left as a topic of future research to develop

a more robust theory for 3D imaging, though some success with 3D imaging has already been demonstrated with a similar IPSII related method [19].

3.2 Imaging Possibilities

There are several imaging possibilities apparent in Eq. 3.9. Since the signal equation is essentially the Fourier transform of the product of three functions (M, $\widetilde{A}_1$, and $\widetilde{A}_2$), any one, or the product of any two of those may be measured, if the others are known or set to a constant. There are three such combinations that could be useful for imaging or measurement.

Object Imaging

The first and most obvious method is the direct measurement of an object [i.e. $M(x,y)$]. This may be done by setting the beam modes $\widetilde{A}_{1,2}$ to a constant (over the desired FOV) by using high quality beams with flat wavefronts. Then a 2D scan measures the Fourier transform of M, after which a simple inverse transform reconstructs the actual image of M. This is the type of imaging we have concentrated on testing.

Beam Profiling

The second option is a simple measurement of the intensity profile of the laser beams. This method works if $\widetilde{A}_1 = \widetilde{A}_2$, as is the case in our interferometer based experiments. If m is set to a constant (by using a blank screen or no object at all), then the function measured reduces to $\widetilde{A}_1\widetilde{A}_2^* = A_1(x,y)^2 = A_2(x,y)^2$. A k-space scan and inverse transform can give the intensity profile of the laser, but phase information is lost. An example of this is method was used in Fig. 2.5 to show the beam profile.

Complex Imaging and Holography

The third, and possibly most exciting possibility, is to set *m* and one of the beam modes to a constant, and measure the complex beam mode of the other beam. Since this measurement gives full phase and intensity information about the beam, it can be used for imaging of complex objects, or transmission holography. See Section 3.3 for a discussion of these possibilities.

3.3   Imaging Properties

Many of the properties and limitations of imaging with these techniques are readily apparent in equations from the previous section, and from the basic properties of a discrete Fourier transform. For example, resolution and FOV in object space are related to their opposites in k-space—i.e. object space resolution is set by k-space FOV, and object space FOV is set by k-space resolution. I will list below some of the inherent or practical limitations on imaging with MAS-IPSII.

Resolution

For a 2D scan in k-space having a maximum angle $2\theta_{\max}$ between interfering beams, the resulting maximum k-space value is obtained by plugging this value into the fringe spacing Eq. 3.6 and taking the inverse. This sets the following limit on resolution:

$$dx_{\min} = \frac{1}{2k_{max}} = \frac{\lambda}{4n\sin(\theta_{\max})} \tag{3.12}$$

It may be surprising that the maximum resolution (as $\theta \to \pi/2$) is $\lambda/4$, which is about a factor of two better than conventional resolution limits (usually stated to be $.47\lambda - .61\lambda$ as NA$\to 1$ depending on the resolution metric). Furthermore, this factor of two holds for any given angle (i.e. IPSII with a given angle limit can achieve twice the resolution as conventional imaging with an objective lens that subtends the same angle). This factor of two improvement was the primary motivation for the development of SIM microscopy.
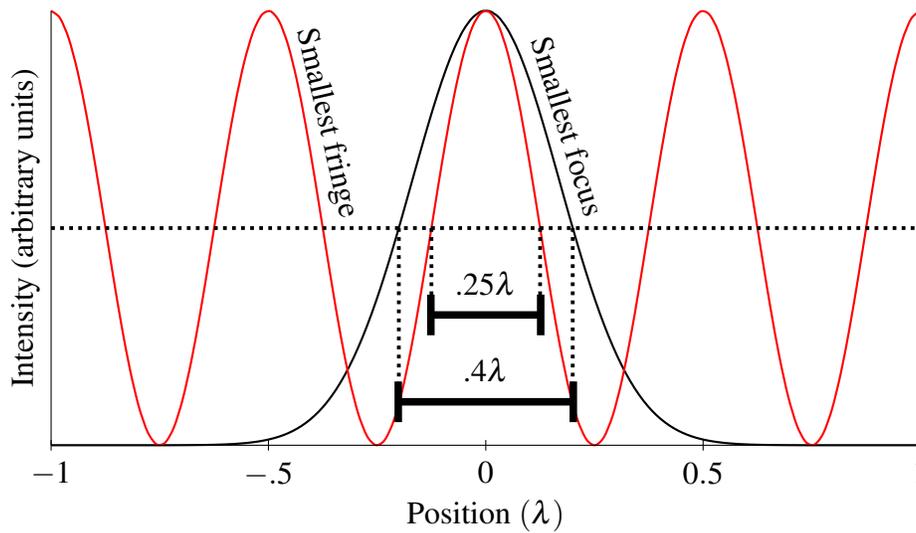
Figure 3.2 Laser focus width compared to fringe width. The tightest possible focus of a laser is shown superimposed on the smallest possible fringes of a standing wave from the same laser. Note that the fringe spacing is about equal to the width of the Gaussian, such that the fringe width is noticeably smaller.

One way to understand the resolution improvement is to compare the width of an interference fringe to the width of a focused point of light. The smallest possible size of a focused laser beam is set by the diameter of the lens, and determines the maximum resolution in confocal scanning microscopy. The smallest laser focus possible is about $\lambda/2$ in width (FWHM), though with some exotic polarization profiles can be as small as $.4\lambda$ [30–32]. Compare this to the minimum fringe width of a standing wave (see Fig. 3.2). At an interference angle of π the interference fringes will have a spacing of $\lambda/2$, and the width (FWHM) of a single fringe will be $\lambda/4$. It is this difference between the minimum fringe width and the minimum beam width that leads to the improvement in resolution.

Field of View

The object space field-of-view $\text{FOV}_{\mathfrak{F}}$ resulting from a discrete inverse Fourier transform from a 2D scan in k-space is similarly obtained by plugging the angle step size of dk into the fringe spacing

Eq. 3.6 and taking the inverse. Of course dk is limited by the minimum angle step $\Delta\theta$ possible. While the relationship between dk and $\Delta\theta$ is non-linear, the more confining limit on dk occurs in the linear small angle region—at larger angles, the same dk step can be made with a larger $\Delta\theta$. For most cases, though, the FOV will be limited by the smallest k-space step that can be obtained consistently throughout k-space, which in turn is the step size obtained in the small angle limit. This sets the following practical limit on $\mathrm{FOV}_{\mathfrak{F}}$:

$$\mathrm{FOV}_{\mathfrak{F},\mathrm{max}} = \frac{2\pi}{dk_{\mathrm{min}}} = \frac{\lambda}{2n\sin(\Delta\theta_{\mathrm{min}})}. \tag{3.13}$$

Since there is no fundamental limit on $\Delta\theta$, there is no fundamental limit on $\mathrm{FOV}_{\mathfrak{F}}$. The precision of a motorized mirror does, however, set a practical limit on $\mathrm{FOV}_{\mathfrak{F}}$. For example, typical commercial motorized mirror mounts have repeatable angular precisions in the range of .1 - 10 arcsec (.5-50 μrad), which would set a practical $\mathrm{FOV}_{\mathfrak{F},\mathrm{max}}$ limit of .5-50 cm (with a 532nm green laser).

Of course, the effective FOV is also limited by various other practical considerations, including beam size and effective detector coverage. Either of these can be fairly easily controlled by using an aperture before or after the object. The detector coverage also has a natural FOV based on the area and directionality of the detector, and its distance from the object. It is important to use some such method to limit the effective total area $\mathrm{FOV}_{\mathrm{det}}$ contributing to the detector signal to be equal to or smaller than $\mathrm{FOV}_{\mathfrak{F}}$, the limit imposed by the discrete Fourier transform, or aliasing will occur (see Section 4.5).

Depth of Field

Since this form of IPSII uses collimated beams, the concept of a DOF is not really applicable. There is no focusing of waves to measure the focus of. However, as DOF usually describes an effective imaging depth, we can consider similar effects. The only such direct limitations with MAS-IPSII are the depth of the interference pattern and the spatial coherence of the laser. The depth of an interference pattern just depends on the diameter of the beams and the maximum beam angle (see
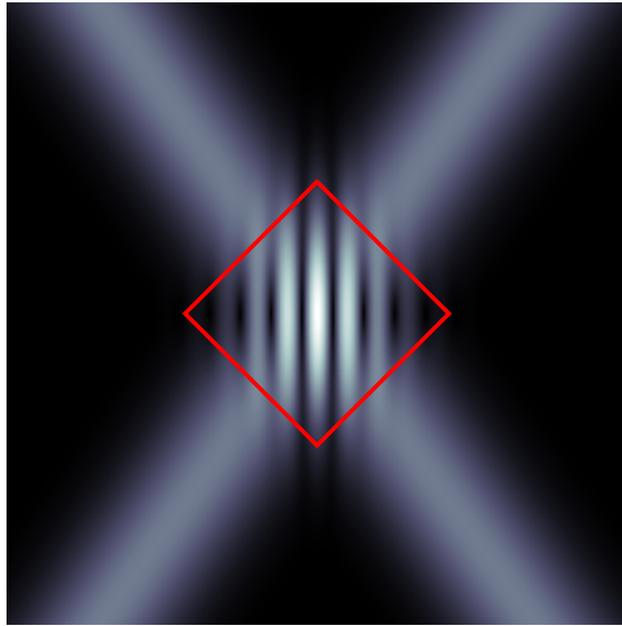
Figure 3.3 Effective DOF. Imaging depth is only limited by the region in which the interference fringes are high contrast, which in turn is limited to about the width of the beams used.

Fig. 3.3). While this means effective DOF is less at higher resolutions (i.e. scans that need to go to higher angles), the effective depth is never any smaller than the beam size, which has no fundamental limit. This is radically different from traditional imaging techniques, which at high resolutions (i.e. NA approaching 1) have DOFs on the order of the resolution—only a very thin slice is in focus.

Speed

Possibly the biggest drawback to MAS-IPSII is the inherent difficulty in reaching high imaging speeds due to the mechanical scan. Before I get into that, however, I would like to note that fundamental limit on imaging speed due to photon efficiency is no different from other techniques for 2D imaging. If local intensity is also a constraint (e.g. due to photo-bleaching, saturation effects, etc.) it has the same limit as other 2D wide field techniques, and is better by a factor of the pixel

count N than raster scanning techniques (such as lidar or confocal microscopy). For 3D imaging, IPSII theoretically has an advantage over even other wide field techniques, since all the photons are used in every measurement (as opposed to throwing away all the out of focus light). In theory this should improve photon efficiency by a factor $\sqrt[3]{N}$ vs other widefield techniques (such as optical slicing) for the same given illumination levels.

In the form we have described (measuring one k-space component at a time), the speed of a scan is ultimately limited to the speed of the mechanical scan (assuming sufficient illumination such that photon statistics are not a limiting factor). Given a pixel count of N and a step size of $\Delta\theta$, a scan must cover approximately $N\Delta\theta$ radians, assuming an efficient scan pattern. Given a maximum angular speed of $v = \Delta\theta/dt$, the minimum time to complete a scan is $N\Delta\theta/v$.

For example, using a commercially available mirror mount (Thorlabs KS1-Z8) with a maximum angular velocity of about .04 rad/s, and a 1mm FOV, a 100×100 image (i.e. 10 kPixel) could be obtained in about 1 min. Keeping the same FOV, but moving to 1000×1000 (i.e. 1 MPixel - 1μm resolution) would require about 2 hours. Our custom built mounts are much slower than even that, so the scan for the images shown in this dissertation (generally about ~ 100 kPixels) took a couple of days complete. The next iteration of our experiment will replace the motors we have been using to drastically speed up this imaging time. There are also various methods that could be used (at the cost of increased engineering or data analysis complexity) to increase imaging by several orders of magnitude. An overview of potential improvements to speed is given in Section 4.6.

3.4 Inconvenient Angle Dependencies

During the derivation of the signal equation, some approximations were made which I will reconsider here. Depending on the nature of light interaction, m may also depend on the illumination angle (e.g. consider how the glare on a shiny object would change as the illumination angle changes). Adding

to this problem, the mode functions ($\widetilde{A}_{1,2}$) also change at large angles due to the transform from the transverse beam coordinates to the object coordinates (i.e. $x_{1,2}$ and $y_{1,2}$ to x and y—consider how a circular mode would appear elongated when shown on a flat object at an angle). In other words, m, $\widetilde{A}_{1,2}$ and by extension $\widetilde{M}'(x,y)$ may also technically be functions of k_x and k_y—$\widetilde{M}'(x,y;k_x,k_y)$, etc. Even if this dependence is known, this completely changes the nature of Eq. 3.9. I know of no general way to invert such a transform, though for particular models of the $k_{x,y}$ dependency, analytical or iterative solutions may be possible.

The good news is that $k_{x,y}$ dependencies in $\widetilde{M}'(x,y)$ can be experimentally eliminated under the appropriate conditions. For example, most of these effects are second order in angle, whereas the fringe spacing is first order, so they can be neglected at small angles. They can also be greatly reduced or eliminated, even at large angles, with appropriate experimental design. Some of the $k_{x,y}$ dependence in m comes about because of changes in the direction of scattered light (e.g. the glare when looking at a shiny object, or refracted light coming out of a crystal or piece of glass at odd angles). With transmission imaging this can be solved simply by placing a large detector close behind the object to capture a solid angle close to 2π, making spatial dependence of the refracted light no longer important. In the case of diffuse reflection, this should not be a problem either. If an appreciable amount of specular reflection also occurs, however, averaging multiple detectors or using an integrating sphere (with slots cut out to allow illumination in) could also be used to largely negate the issue.

The $k_{x,y}$ dependence in $\widetilde{A}_{1,2}$ is easier (in concept) to remove. The illuminating beams just need to be made uniform on the scale of the imaging FOV, such that they are constant over the object. The 'stretching' that occurs as the beams are moved to larger angles will then only have the effect of diminishing the overall illumination intensity (and therefore signal) by $\cos\theta$. This can easily be compensated for experimentally or computationally. Keeping the wavefronts perfectly flat such that the phase of the beam modes is also uniform across the object is a more significant

challenge (though not beyond the capabilities of accessible technology). The problems introduced by imperfect wavefronts are addressed in Section 4.2.

With these appropriate considerations, the $k_{x,y}$ dependence can be almost completely removed. One remaining effect is that the transmissivity and reflectivity coefficients of a material generally also depend on angle. This should mostly be a problem for smooth surfaces (i.e. specular reflection and transmission), and at large angles. We have not yet explored this particular issue in any depth.

Many of these issues (glare, shadows, angle-dependent scattering, etc.) are also present in, and affect the results of conventional imaging. However, they are more of a problem with IPSII because they change when the illumination changes, resulting in a different glare, etc., being measured with each wavenumber. The net effect on the reconstructed object space image can be difficult to predict, but we are working on some numerical simulations and measurements to better understand these effects. These efforts could benefit a variety of other structured illumination techniques as well.

3.5   Complex Imaging

One of the interesting results from Section 3.1 is that the signal equation depends on the complex mode functions, not just their intensity distributions. This can be taken advantage of to measure the mode functions themselves. To do so, we would just need to set *m* and one of the beam modes to be a constant, while allowing the other to be arbitrary. This could be done by using a high quality laser beam with very flat wavefronts, and removing the object from the beam path, or replacing it with a blank screen. The other beam $\widetilde{A}_2$ may have an arbitrary complex profile. The resulting signal equation is

$$\widetilde{s}(k_x, k_y) = \int_{-a}^{a} \int_{-b}^{b} \widetilde{A}(x,y) e^{i(k_x x + k_y y)} dx dy \tag{3.14}$$

such that the components of the Fourier transform of the complex mode function are directly measured.

One possible use of this would be to profile a laser beam and perform wavefront measurements. Doing so would require a second beam with a quality spatial mode (which could be obtained from the same source via spatial filtering, or from a separate phase locked laser).

Other possible uses include transmission or reflection holography and imaging of complex objects. If an object with complex profile is placed in just the second beam, before the overlap region, then the beam mode is altered at the location of the object to

$$E_2(x_2, y_2, t) = m(x, y)\widetilde{A}_2(x_2, y_2)e^{i\mathbf{k}_2 \cdot \mathbf{r} + i(\omega + \Delta\omega)t}. \tag{3.15}$$

If both beams initially have flat constant wavefronts, and overlap directly on a detector or blank screen, then the signal equation becomes

$$\widetilde{s}(k_x, k_y) = \int_{-a}^{a} \int_{-b}^{b} m'(x, y)e^{i(k_x x + k_y y)} dx\, dy \tag{3.16}$$

where $m'(x, y)$ is $m(x, y)$ propagated to the detector location. Since full phase information would be recorded, recovering $m(x, y)$ should be a simple back propagation calculation. Furthermore, all the advantages possible with digital holography should be applicable, such as computational refocusing, optical sectioning (to obtain a 3D image), etc. See Fig. 3.4 for a low resolution proof-of-concept hologram with back projections (note, though, that this work is in its early stages).

For this method of complex imaging to work, especially at larger angles, the beam being imaged would need to not change in angle relative to the imaging plane so as to avoid distorting the complex mode being imaged. In this case, the maximum angle between the two beams is cut in half. Furthermore, since the fringes in 3D space are no longer perpendicular to the imaging plane, their projection in the imaging plane is stretched out a little as a function of angle, so that the fringe spacing (from Eq. 3.6) is modified to

$$d = \frac{\lambda}{2n \sin\theta \cos\theta} \tag{3.17}$$

resulting in modified expressions for the pattern wavenumbers, $k_x = 2k_l \sin\theta \cos\theta \cos\phi$ and $k_y = 2k_l \sin\theta \cos\theta \sin\phi$.
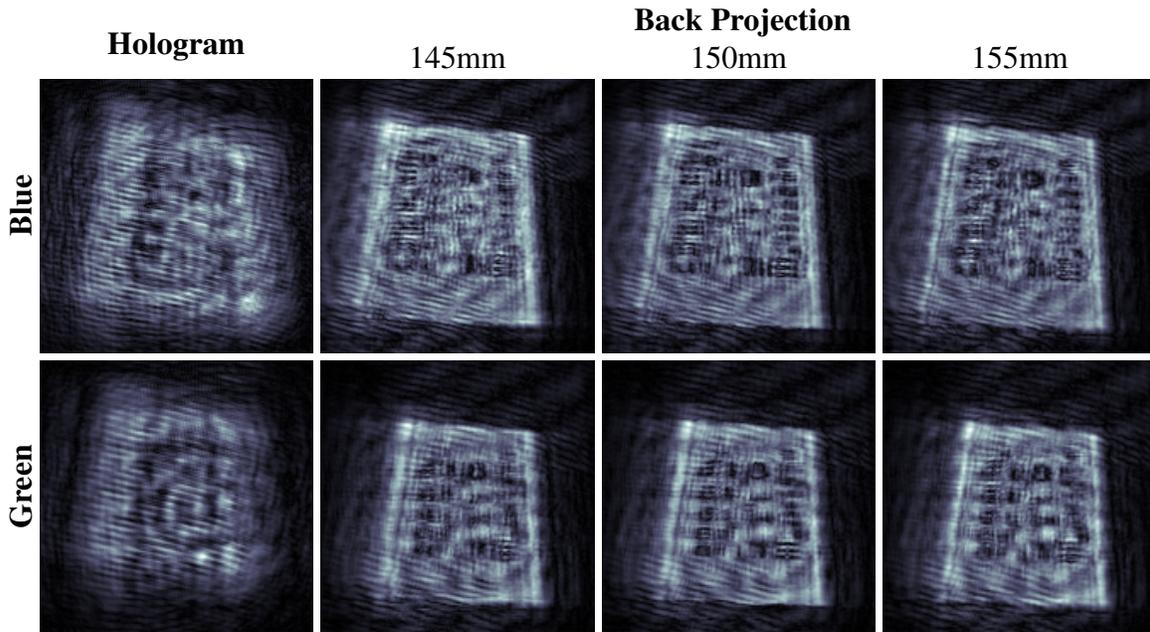
Figure 3.4 Transmission holography and back projection. Images from a dual-wavelength (407nm and 532nm) scan show the diffraction of a positive resolution test target placed in one arm of the interferometer about 15cm away from the detector. Back projections to various image planes are shown. Only the second, unobstructed, beam was scanned.

3.6 Filtered Imaging

One of the experimental constraints we face is a potentially very large DC offset $C(A_1, A_2)$ (see Eq. 3.8) of the signal detector. While this offset is removed in the demodulation step, it has some negative effects before that point in the experiment, including reduced SNR and a much greater dynamic range requirement from the detector and electronics than would otherwise be necessary (dynamic range is already an inconvenient issue when measuring in a sparse domain such as k-space—see Section 4.7). Because the analog signal coming from the detector is very large, the trans-impedance gain is limited to prevent saturation and non-linear effects of the photo-detector. This makes it difficult to separate the desired signal from electronic noise. Even with ideal equipment, this effect inherently limits the SNR due to photon noise, since the useable signal comes from a small component of the overall light incident on the object.
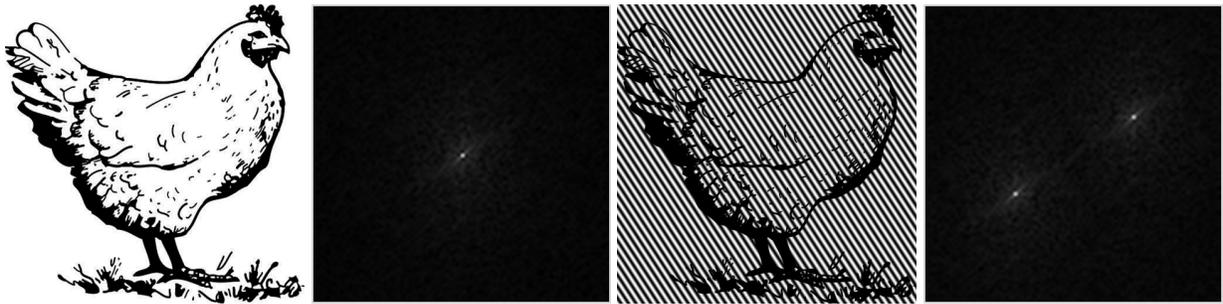
Figure 3.5 Spatial modulation illustration. From left to right: an image of a chicken, the Fourier transform of the chicken, a modulated chicken, and the Fourier transform of the modulated chicken. Note that for the modulated chicken, the peaks in k-space occur away from the center where the detector would be placed using the method described in this section.

One possible method of removing the offset, somewhat analogous to darkfield microscopy, would be to optically filter out the DC component of the signal. In theory this could be done in transmission images simply by placing the detector so as to measure only diffracted light, and not the light coming straight through parallel to one of the beams. This could be done by placing the detector on the imaging axis far away from the detector, by using a small detector, or by placing the detector behind a pinhole—the important parameter being the solid angle subtended by the detector. This would, of course, result in significant changes to the theoretical signal equation.

Conceptually, the idea is similar to Fourier imaging, but only the center of the diffraction pattern is measured with each measurement. The full diffraction pattern is measured by modulating the pattern with each step, and effectively shifting the interference pattern, so that what was the center of k-space (along with the large DC offset that it carries) is shifted away from the measurement region, and a different region of k-space is shifted to the center to be measured. An illustration of this is demonstrated in Fig. 3.5.

In this section I will derive a signal equation for this kind of a fourier 'filtered' detection setup, which will follow a similar process to the derivations above. It turns out that this method is also another way to perform 'complex' imaging, since the resulting signal equation depends on $m(x,y)$

instead of $M(x,y)$.

At the object plane (after light has been transmitted) the amplitude of the light field is

$$E_{\text{obj}}(x,y) = m(x,y)(E_1(x,y) + E_2(x,y)). \tag{3.18}$$

We assume the detector is far enough away that we can use the Fraunhofer diffraction equation to calculate the field at the point of the detector (or pinhole).

$$E_{\text{det}}(x',y') \propto \int_{-\infty}^{\infty}\int_{-\infty}^{\infty} E_{\text{obj}}(x,y)e^{-i\frac{k_l}{z}(x'x+y'y)}dxdy, \tag{3.19}$$

where the primed coordinates are the coordinates on the plane of the detector, and the unprimed coordinates are on the plane of the object. Note that this is just a Fourier transform of the field. To calculate a signal s, we then need to average the intensity incident on the detector. To do so we take the intensity of the field multiplied by a function representing the detector area, which we assume is small enough to approximate as a Dirac-delta function:

$$\begin{aligned} s &\propto \int_{-\infty}^{\infty}\int_{-\infty}^{\infty} \delta(x',y') \left| \int_{-\infty}^{\infty}\int_{-\infty}^{\infty} E_{\text{obj}}(x,y)e^{-i\frac{k_l}{z}(x'x+y'y)}dxdy \right|^2 dx'dy' \\ &= \left| \int_{-\infty}^{\infty}\int_{-\infty}^{\infty} E_{\text{obj}}(x,y)dxdy \right|^2 \\ &= \left| \int_{-\infty}^{\infty}\int_{-\infty}^{\infty} m(E_1+E_2)dxdy \right|^2, \end{aligned} \tag{3.20}$$

Note that this equation is almost identical to Eq. 3.7, except that the absolute value is taken *after* the integral instead of *before* it. Expanding $E_{1,2}$ we get,

$$s = \left| e^{i\omega t} \int_{-\infty}^{\infty}\int_{-\infty}^{\infty} m(\widetilde{A}_1 e^{i\mathbf{k}_1 \cdot \mathbf{r}} + \widetilde{A}_2 e^{i\mathbf{k}_2 \cdot \mathbf{r} + i\Delta\omega t})dxdy \right|^2 \tag{3.21}$$

$$= \left| e^{i\omega t} \int_{-\infty}^{\infty}\int_{-\infty}^{\infty} m(\widetilde{A}_1 e^{ik_{1x}x+k_{1y}y} + \widetilde{A}_2 e^{ik_{2x}x+k_{2y}y+i\Delta\omega t})dxdy \right|^2, \tag{3.22}$$

where $k_{(1,2)x}$ and $k_{(1,2)y}$ are the x and y components of the wave vectors of the individual beams. Note that we again have the form of a Fourier transform in each term inside the absolute value.

With the 2D Fourier transform of f evaluated at (k_X, k_y) denoted as $\mathfrak{F}\{f\}(k_x, k_y)$, we have,

$$s = \left| \mathfrak{F}\{m\widetilde{A}_1\}(k_{1x}, k_{1y}) + \mathfrak{F}\{m\widetilde{A}_2\}(k_{2x}, k_{2y}) e^{i\Delta\omega t} \right|^2 \tag{3.23}$$

$$= \left| Be^{i\phi_1} + De^{-i\phi_2} e^{-i\Delta\omega t} \right|^2 \tag{3.24}$$

$$= B^2 + D^2 + \mathrm{Re}\left\{ BDe^{i(\phi_1 - \phi_2 - \Delta\omega t)} \right\} \tag{3.25}$$

where B, D and $\phi_{1,2}$ are introduced to shorten later equations and represent the magnitude and phase components of the Fourier transform terms.

After temporal demodulation we get,

$$\widetilde{s} = BDe^{i(\phi_1(k_{1x}, k_{1y}) - \phi(k_{2x}, k_{2y}))}. \tag{3.26}$$

Note that we have two sets of k-values now (as opposed to one, the $k_{x,y}$ values, in Section 3.1). There are multiple ways to extract the phase and amplitude values for individual spatial frequencies (i.e. determine B, D, ϕ_1 and ϕ_2). As a theoretical proof of concept I will lay out below one way it might be done, but will leave it to future work to determine if this is practical, or if there are other methods which give better results.

The amplitudes can, in principle, be extracted from a single measurement. Let $\bar{s}$ be the time average value of the raw signal (before demodulation). Then

$$\bar{s} + |2\widetilde{s}| = (B+D)^2$$

$$\bar{s} - |2\widetilde{s}| = (B-D)^2$$

$$\Rightarrow$$

$$\begin{aligned} B &= \frac{\sqrt{\bar{s} + 2|\widetilde{s}|} + \sqrt{\bar{s} - 2|\widetilde{s}|}}{2} \\ D &= \frac{\sqrt{\bar{s} + 2|\widetilde{s}|} - \sqrt{\bar{s} - 2|\widetilde{s}|}}{2} \end{aligned} \tag{3.27}$$

Recovering the phase functions $\phi_{1,2}(k_x, k_y)$ is a little trickier because only a phase difference $(\phi_1 - \phi_2)$ is ever measured. One way to do it would be to just pick a fixed angle (other than $\theta = 0$)

for the second beam through the whole scan. Then ϕ_1 is determined relative to an arbitrary global phase (ϕ_2). Imaging a complex object m is then just a process of scanning k_{1x}, and k_{1y} to obtain $\mathfrak{F}\{m\widetilde{A_1}\}(k_{1x}, k_{1y})$ and performing an inverse transform.

Chapter 4

Imaging Issues and Solutions

There are various issues which can affect image quality when using MAS-IPSII. These include potential experimental problems as well as more fundamental problems. In this chapter I will give an overview of issues that we have encountered or considered. In cases where we have observed the image artifacts or distortions resulting from the issue, I will include data and images to demonstrate the problem, and in cases where we have found a solution or a workaround I will describe that as well.

See also Appendix D for a list of k-space images showing more trivial scan errors and data corruption issues we have encountered during 2DFT MAS-IPSII scans.

4.1   Parallels with Magnetic Resonance Imaging

While the use of Fourier transforms in image and data processing is very common, there are relatively few experimental techniques that involve making complex (i.e. phase and amplitude) measurements directly in k-space. Perhaps the largest body of literature that deals with this type of measurement is magnetic resonance imaging (MRI). The physics of MRI measurements is, of course, wholly unrelated to IPSII, but many of the problems encountered in MRI related to k-space measurements

are very similar to what can happen with MAS-IPSII measurements and reconstructions. As a result, many techniques and algorithms developed for MRI can also apply directly to MAS-IPSII. Some of the ideas used in this chapter were inspired by their MRI counterparts, and I will point to the relevent literature where appropriate.

4.2   Phase Distortions

One of the first questions one might consider about the practical implementation of a phase sensitive imaging method such as IPSII is the effect that phase distortions in the beam wavefronts will have. Obtaining a uniform illumination intensity is relatively simple, but obtaining a source with perfectly flat wavefronts is much more difficult, experimentally. In practice small phase distortions are likely to result in interference patterns such as those displayed in Fig. 4.1. To what degree are imperfections like these in the phase of the beam mode going to affect or limit MAS-IPSII?

No distortion   Random   Lens   Lens ($\theta = 0°$)   Small Lens   Lens+Random
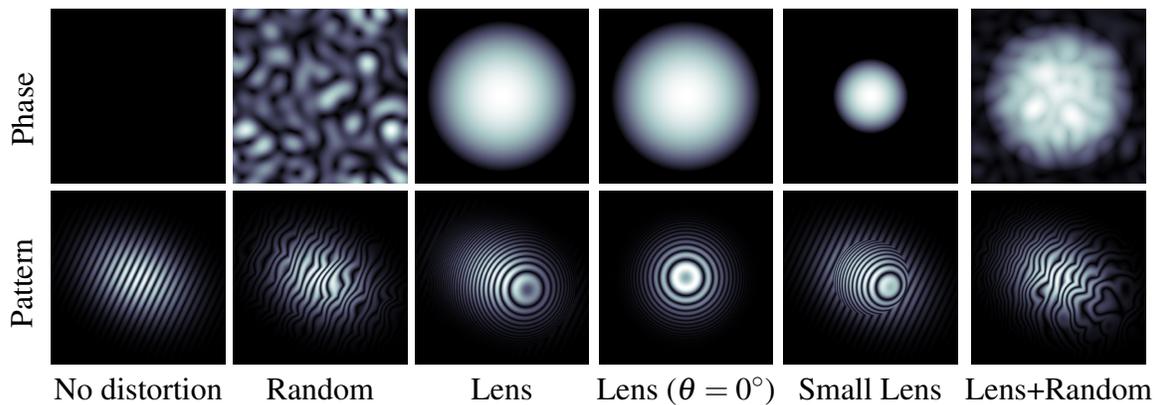
Figure 4.1 Simulations of non-sinusoidal illumination patterns. Interference patterns are generated between two Gaussian beams, one with flat wavefronts and the other with phase distortions from a spherical lens, an uncollimated source beam, or a pseudo-random phase surface. A large input wavelength was used to make fringes easily visible. Top row: phase plot of distorted beam. Bottom row: resulting interference pattern with a $\theta = 45°$ beam angle (unless otherwise noted) and an orientation of $\phi = 45°$. The simulations of a lens in one arm are also equivalent to a path-length imbalance coupled with an uncollimated beam. Note that the distorted illumination patterns are not simple 2D sine waves.

It is partly in anticipation of dealing with this question that the signal equation was derived using complex exponentials and put in terms of a Fourier transform instead of a real valued sine transform. If one considers the interference patterns to be 2D sine functions (which with ideal beams, they are), then the signal equation could just as easily be described in terms of a sine transform. In this case the idea of 'negative' spatial frequencies, and of 'negative' beam angles would be meaningless, and scanning the beam angles from $-\theta_{\text{max}}$ to θ_{max} would give redundant information compared to a scan from 0 to θ_{max}. This information redundancy in the spatial spectra of a real object can also be seen in a complex Fourier transform. As long as the function being transformed is real, the transformed function has complex symmetry,

$$F(k_x, k_y) = F^*(-k_x, -k_y). \tag{4.1}$$

The difference between a sine transform and a complex transform is more apparent when phase distortions are introduced. Starting from a sine transform, this would be properly accounted for by adding a spatially varying phase to the sine terms, resulting in basis functions which are far from simple sine waves (see Fig. 4.1 for some examples), and a transform that is mathematically intractable. With a complex transform, the phase variations can be separated from the complex exponentials, and instead considered to be part of the object—i.e. the complex function $\widetilde{M}'(x, y)$ introduced in Chapter 3—so that we still have a reversible Fourier transform.

Even if the object function is not real (or equivalently, the basis functions are not sinusoidal), we can generate conjugate symmetry by using half of k-space to fill in the other half, and use the resulting image reconstruction to get an idea of how good or bad the assumption of a real object is. In cases where the object function is close to real, this will have little effect on a reconstructed image, but in cases with large phase distortions the distortions this process introduces int the object will become more pronounced.

Large Angles

In Section 3.4 I pointed out that the inconvenient $k_{x,y}$ dependence in the mode functions $(\widetilde{A}_{1,2})$ can only be neglected if the beam wavefronts are constant *or* when small angles are used. Since we are discussing phase distortions, the mode functions are inherently *not* constant, so small angles must be assumed to get any useful analytical insight. Unless noted otherwise, the following discussions and solutions assume the maximum scan angle is sufficiently small to ignore these issues.

Properly dealing with the effects of phase distortions at larger angles where $k_{x,y}$ dependence in the beam modes must be accounted for is a more complicated problem that remains unsolved for now. Imaging at larger angles can still be done, but will require high quality beams with flat wavefronts. Further work is needed to determine under what experimental conditions and angles the results from the small angle assumption are no longer applicable, and how else one might resolve distortion issues in that case.

Types of Distortions

Phase Distortion Categories		
	Constant (during scan)	**Changing**
Common (to both beams)	Bad mode quality or uncollimated beam. Imperfect optics before first beamsplitter.	Unstable laser mode.
Different	Unbalanced interferometer. Imperfect optics after beamsplitter, but before scanning mirrors.	Imperfect optics between first pair of scanning mirrors and second beamsplitter.

Table 4.1 Likely sources of phase distortion sorted into categories. Green cell (top left): No direct affect on imaging. Blue (bottom left, top right): does not affect imaging in some cases. Red (bottom right): Effectively adds noise to k-space data which cannot be removed or compensated for with any known method.

Phase distortions can be categorized into those that are constant throughout the scan versus those that are not, those that are common to both beams versus those that are not, and those that are

known versus those that are unknown. Likely sources of distortion are divided into intersections of the first two categories in table 4.1. Some examples of distortions which affect only one beam but are constant during a scan are shown in Fig. 4.1. These distortions are particularly interesting since they can have a drastic effect on the illumination patterns, effectively changing the SI imaging basis to something wholly different (and unknown), and yet, a quality object image can still be obtained.

Constant Distortions

Constant phase distortions that are common to both beams are the easiest distortions to deal with. So long as the interferometer is well balanced, and properly aligned (such that the beam modes perfectly overlap) they have no effect on the resulting interference pattern, and should have no appreciable effect on imaging. This is readily apparent when simplifying the integrand from the signal equation (Eq. 3.9) using the expanded definition of $\widetilde{A}_{1,2}$ (Eq. 3.1) and setting the spatial phases $\phi(x,y)$ of both beams equal:

$$
\begin{aligned}
\widetilde{M}'(x,y) &= M\widetilde{A}_1\widetilde{A}_2^* \\
&= MA_1A_2 e^{i(\varphi_1(x,y)-\varphi_2(x,y))} \\
&= MA_1A_2.
\end{aligned}
\tag{4.2}
$$

For a phase distortion that is not common to both beams the phase does not cancel out, but adds a complex phase $\Delta\varphi = \varphi_1 - \varphi_2$ to the measured function $\widetilde{M}'$. After completing a 2D scan and performing the inverse transform one can simply take the absolute value of the result and this phase goes away:

$$
\begin{aligned}
|\widetilde{M}'(x,y)| &= M|\widetilde{A}_1\widetilde{A}_2^*| \\
&= MA_1A_2|e^{i\Delta\varphi(x,y)}| \\
&= MA_1A_2.
\end{aligned}
\tag{4.3}
$$

Non-constant Distortions

Phase distortions which are not constant but are common to both beams (such as mode hopping, assuming a well balanced interferometer) still experience the same cancellation as in Eq. 4.2. Distortions that are not constant and different between beams, however, cannot be eliminated as in Eq. 4.3. The changing dependence can be thought of as a dependence on angle, or equivalently $k_{x,y}$, even if the phase distortion is a function of time (e.g. mode hopping with an unbalanced interferometer), since the scan maps $k_{x,y}$ to time. This leads to the following signal equation:

$$\widetilde{s}(k_x,k_y) = \int_{-\infty}^{\infty} \int_{-\infty}^{\infty} MA_1 A_2 e^{i\Delta\varphi(k_x,k_y;x,y)} e^{i(k_x x + k_y y)} dxdy \tag{4.4}$$

This transform is no longer generally reversible, though for particular forms of the $\Delta\varphi(k_x,k_y;x,y)$ function it may be possible to remove it.

For example, if the phase is separable in the form $\Delta\varphi = \alpha(k_x,k_y) + \beta(x,y)$, and the α term is known, then the $k_{x,y}$ term comes out of the integral and can be divided out of the signal. Of course this is a relatively trivial dependence, one that would account for something like a slight change in the relative path-length of the two interferometer arms due to imperfect symmetry in optical layout or motor movements. This correction is not necessary for our setup because the way our reference signal is derived already eliminates such phase offsets. It could be useful, however, if there were some slight (known) movement of the pinhole relative to the object during the scan, or if the reference signal were derived in some other way. In principle, with an extremely stable or small measurement setup, it should be possible to use an independent reference rather than a measured (e.g. pinhole) reference. In this case it would almost certainly be necessary to correct for phase shifts occurring due to mechanical movement throughout the scan.

Other, more interesting, $k_{x,y}$ dependencies may be possible to deal with on a case by case basis. A particularly interesting case would be the mode distortion (i.e. stretching) introduced by going to large angles. In this case the $k_{x,y}$ dependence is well known and understood since it simply

shows up in the transformation of $(x,y)_{1,2} \rightarrow (x,y)$ coordinates as a dependence on the beam angles. Unfortunately, we have not yet found a simple way to account for this dependence in the signal equation, and instead need to either control the wavefronts so that such distortions are not a problem, or stick to smaller angle (and lower resolution) scans.

Some examples of phase distortion data are shown in Fig. 4.2 and Fig. 4.3. These figures show image reconstructions of a negative and a positive, respectively, USAF1951 resolution test target. In these figures various objects were used to deliberately distort the wavefronts of one of the lasers inside the interferometer, to introduce a large $\Delta\varphi$. When full k-space data is used (i.e. including positive and negative spatial frequencies, from corresponding positive and negative angles), the resulting image reconstruction (obtained by taking the absolute value of the inverse Fourier transform of the k-space data) is shown to be relatively robust against beam distortions. Images constructed using only half of k-space, with an assumption of conjugate symmetry being used to fill in the other half, are shown for comparison. These are similar to what would be obtained if the (incorrect) assumption were made that that the interference patterns were all nicely sinusoidal and a discrete sine transform were used. An image reconstructed from half of k-space with no attempt to fill in the other half is also shown for comparison. The last column of the table shows the phase of the complex image obtained from the full k-space data, which clearly shows the phase structure of the object used to obstruct the beam, as described in Section 3.5.

The limits of our ability to deal with distortion in the beam are clear in the last row of Fig. 4.3, where the beam was distorted so badly that the amplitude was also visibly affected (noisy and diffuse, with a grainy texture), and the reference signals were noisy and demonstrated characteristics indicating interference fringe widths that were sometimes on the order of the pinhole radius.
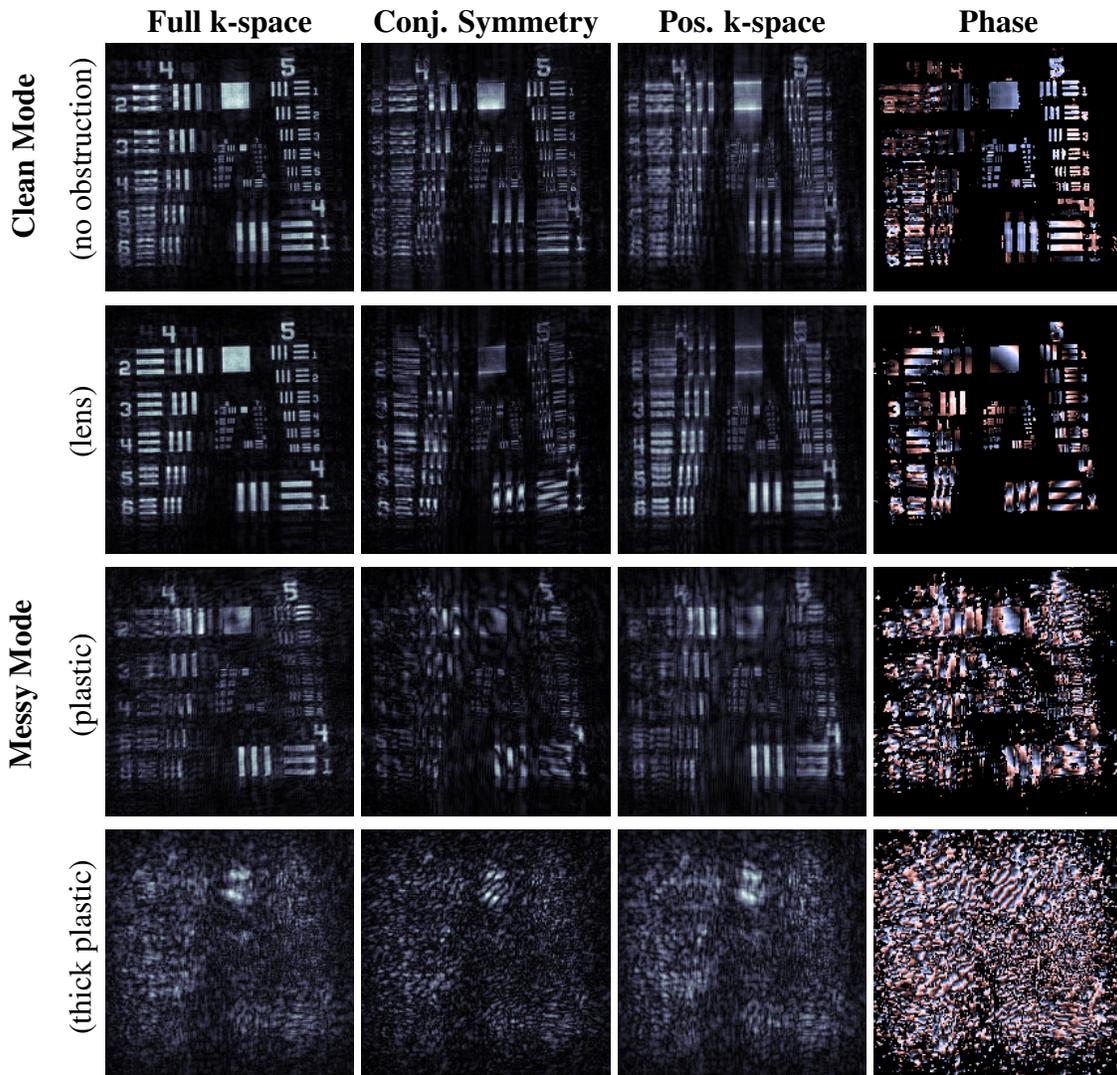
Figure 4.2 Images of a negative resolution test target made with a distorted wavefronts. Images have a 1.67x1.67 mm^2 FOV. Four scans were taken in which the mode of the laser beam in one arm of the interferometer was distorted up by inserting various 'phase' objects (such as a lens or clear piece of plastic) . The first column gives the image reconstruction obtained using full k-space data. In the second column, only half the k-space data was used, with the other half being filled in using conjugate symmetry. In the third column, only half of k-space data is used, with the other half set to zero. The fourth column shows the phase. The phase image is blacked out in areas with low values where the complex phase is mostly just due to noise.
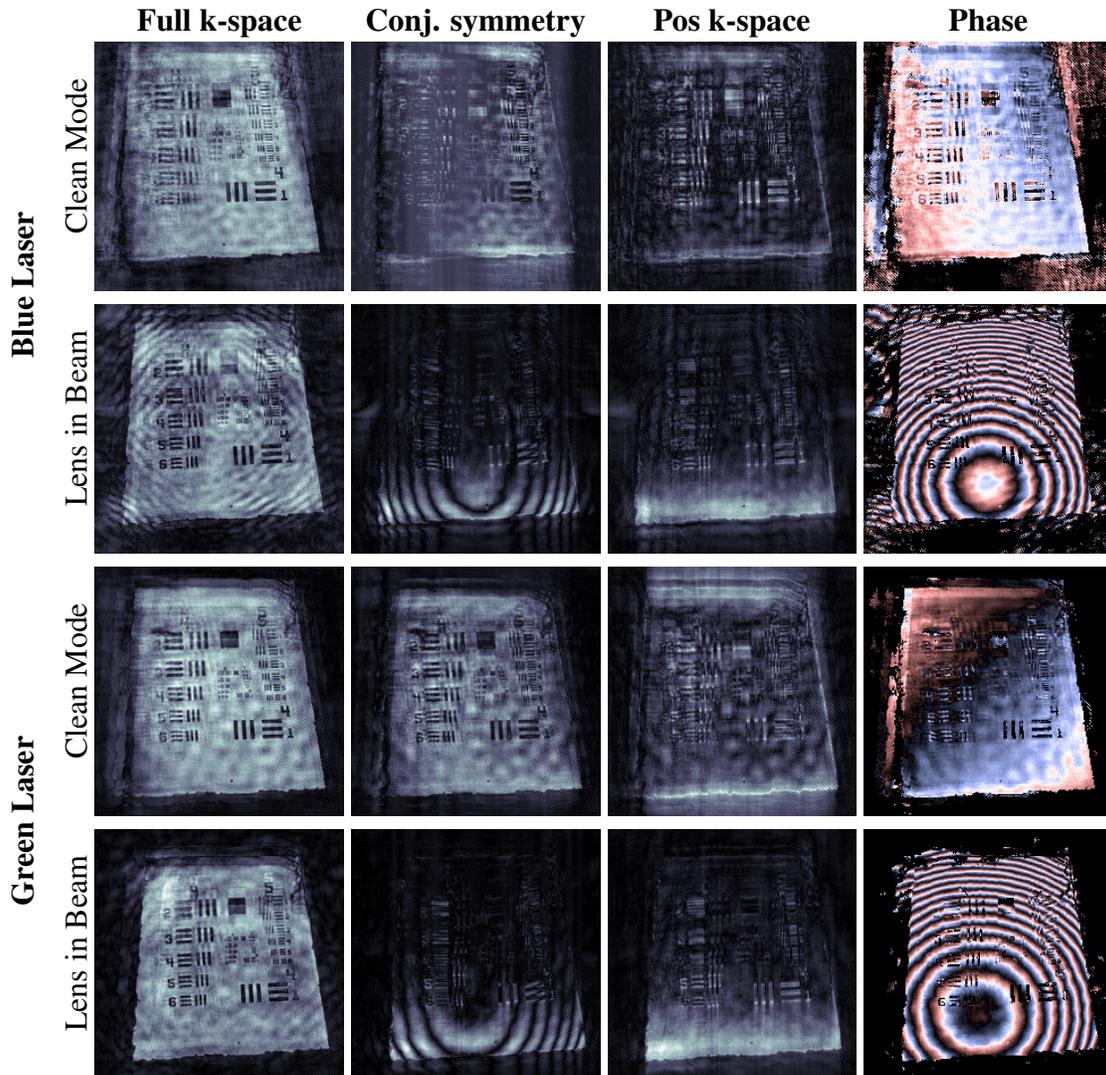
Figure 4.3 Images of a positive resolution test target made with a distorted wavefronts. Images are from two dual wavelength scans (532nm and 407nm). In the first scan both lasers have relatively clean modes, as is visible in the phase images in the last column. In the second scan a lens was placed in the beam path of one arm of the interferometer. Note that the circular rings in the phase images show the curvature of the wavefronts caused by the lens.

4.3   Amplitude Distortions

Another issue which can affect image reconstructions is an amplitude in either beam which is not constant over the imaged area, or an 'amplitude distortion'. Similar to phase distortions, dealing with amplitude distortions is an intractable problem at large angles. For small angles, however, it has the same effect as non-uniform lighting does in conventional imaging, and similar to conventional imaging, it can be easily compensated for if measured. The reconstructed image, after removing phase distortions (i.e. taking the absolute value) is just $M(x,y)A_1(x,y)A_2(x,y)$, so if $A_{1,2}$ are known, they can be divided out of the image anywhere they are not close to zero. Measuring $A_{1,2}$ is a simple matter of imaging a blank object (see Section 3.2). Unlike the phase distortions, however, amplitude distortions cannot be removed without prior knowledge of the distortion.

4.4   K-space Position Errors

Section 3.3 introduced the theoretical FOV constraints imposed by a minimum angle $\Delta\theta_{\text{min}}$. In our setup the minimum relative angle step size can be much smaller than our absolute angular accuracy. Because of this, we can easily do a scan where the angular step size $\Delta\theta$ is comparable in size to angular error, meaning that each time we take a data point we measure a spatial frequency that is slightly offset from the one we intended to measure. This error may be parameterized as α, where α is the ratio of the maximum error in k-space to d_k. See Fig. 4.4 for an illustration of periodic or random k-space position errors with $\alpha = 0.2$.

Errors arise due to mechanical error in the angle scan (or measurement error if a closed loop system were to be used). We believe our system is subject to some amount of both random and periodic error arising in the gearbox of our stepper motors. It is possible that both of these could be significantly lowered by using higher-quality stepper motors, or using optical encoders to make closed loop angle adjustments.

(a)   **(b)**   **(c)**
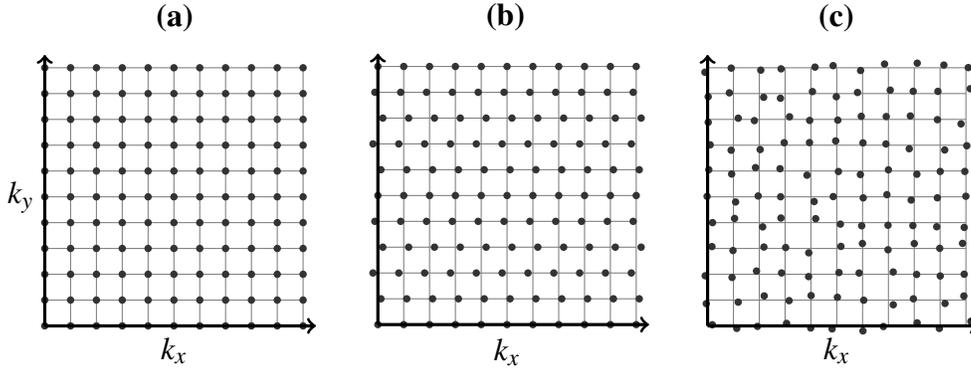
Figure 4.4 Types of k-space position error. The light grey grid represents the points at which a measurement is supposed to be made (i.e. the k_x, k_y coordinates corresponding to the beam angles as they were set or measured). The dots represent the point where the measurement was actually made. In (a) there is no k-space error. In (b) the k-values are off periodically, and in (c) the k-values are off by a random amount. Both (a) and (b) have an error parameter of $\alpha = .2$.

The result of k-space position errors depends on the type and magnitude α of the errors. These errors impose another effective field-of-view limit,

$$\text{FOV}_{\text{err}} = \frac{2\pi}{(\alpha+1)dk}. \tag{4.5}$$

This limit is centered around the position of the pinhole, and is the only reason why positioning the pinhole and the object close to the same relative positions in the two interferometer outputs is important. Outside of FOV_{err} noise and image artifacts will cover up and distort the image beyond recognizability, but regions in the image that are well within FOV_{err} should be mostly unaffected by the k-space errors.

Position errors in k-space can be categorized as random, periodic and constant. A small constant shift has little effect on the resulting image, and can be undone by re-centering k-space data. Random errors show up in the image reconstruction by increasing noise as a function of distance from the pinhole (see random error simulations in Fig. 4.5), while periodic errors cause a stretching and ghosting effect (see periodic error simulations in Fig. 4.6). Acutal image reconstructions demonstrating what we believe are the effects of random or periodic errors in our experiment are
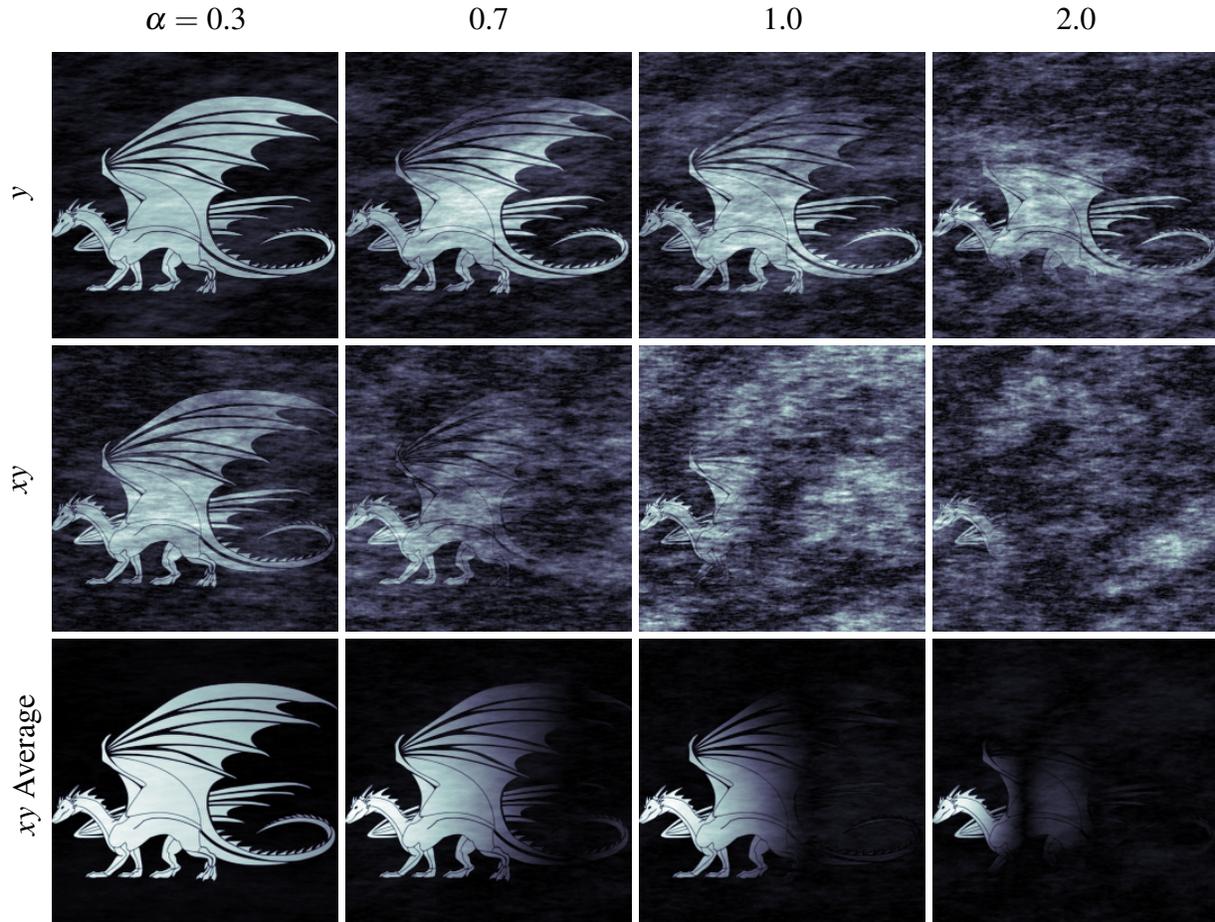
Figure 4.5 Random k-space position errors. Position of points in k-space is randomly offset in either the *x* direction or the *x* and *y* directions. Error in either direction is uniformly distributed in the range $(-\alpha dk, \alpha dk)$, where *dk* is the discrete k-space spacing. The simulated origin (i.e. where the pinhole would be) is by the dragons head. The last row shows averages of 100 image reconstructions made with each α random error (in both directions). In this row, it is clear that the average effect of the error is to effectively limit FOV as expected—e.g. $\alpha = 1.0$ is effectively equivalent to doubling *dk*, and halving the FOV.

shown in Fig. 4.7. The location of the pinhole is also indicated in each image. As expected, the images are clearer in a region around the pinhole location.

The ghosting effect caused by periodic errors occurs in the direction of the periodic error (especially near or outside of FOV_{err}). The brightness of the 'ghost', and the amount it is shifted
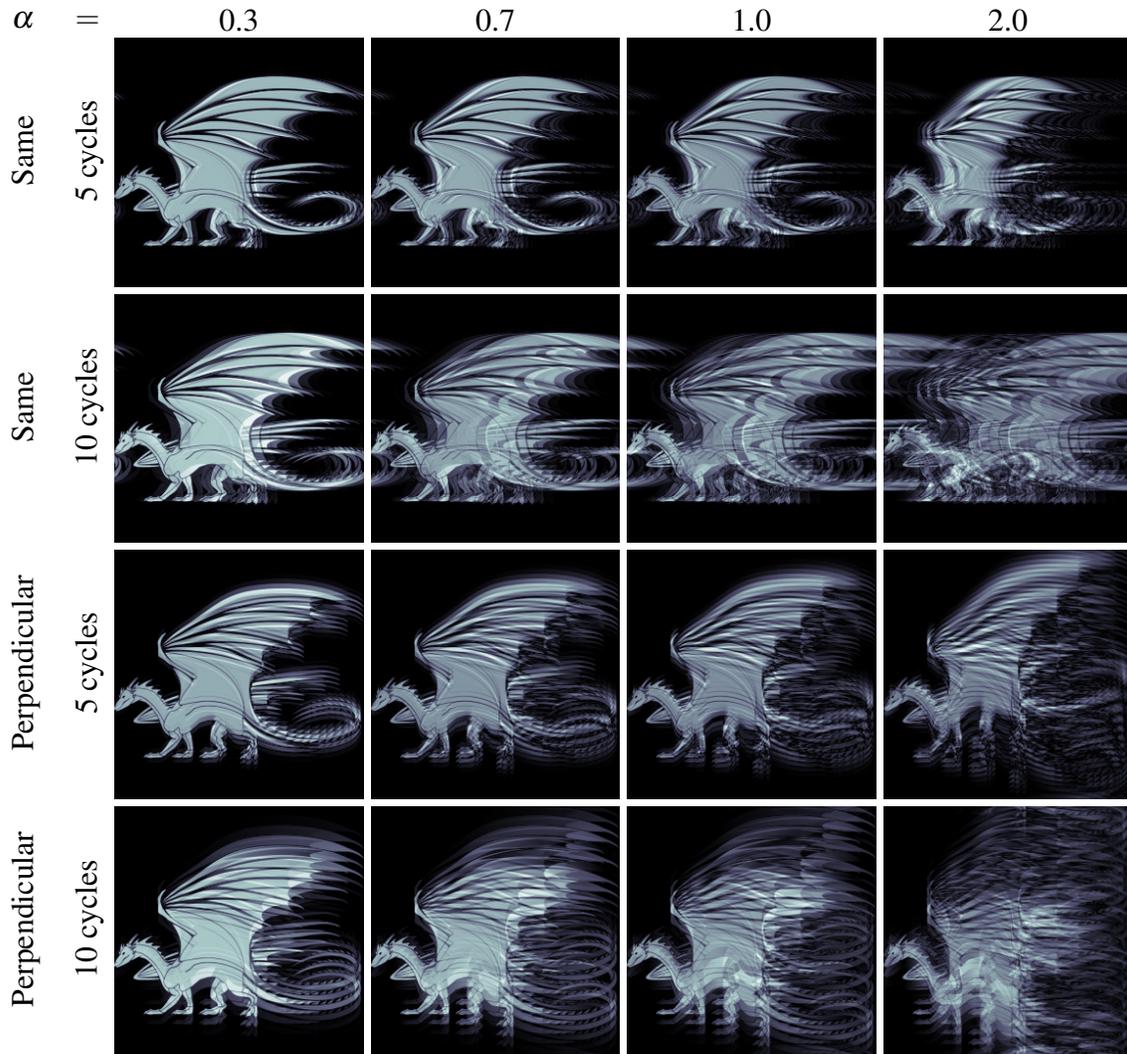
Figure 4.6 Periodic k-space position errors. The magnitude of the error offsets are periodic in x, and the direction of the offsets is in either the same ($\hat{\mathbf{x}}$) or the perpendicular ($\hat{\mathbf{y}}$) direction (i.e. position error with a period T was modeled as $\sin(2\pi x/T)\hat{\mathbf{x}}$ or $\sin(2\pi x/T)\hat{\mathbf{y}}$). This causes stretching and ghosting that gets worse towards the right (where x is large), but the ghost images are shifted in the direction of the offsets (either $\hat{\mathbf{x}}$ or $\hat{\mathbf{y}}$). The error parameter α is equal to the ratio of the error amplitude to the discrete k-space spacing dk. Then simulated origin (i.e. where the pinhole would be) is on the dragons head. The frequency of the error is give in cycles/image width.
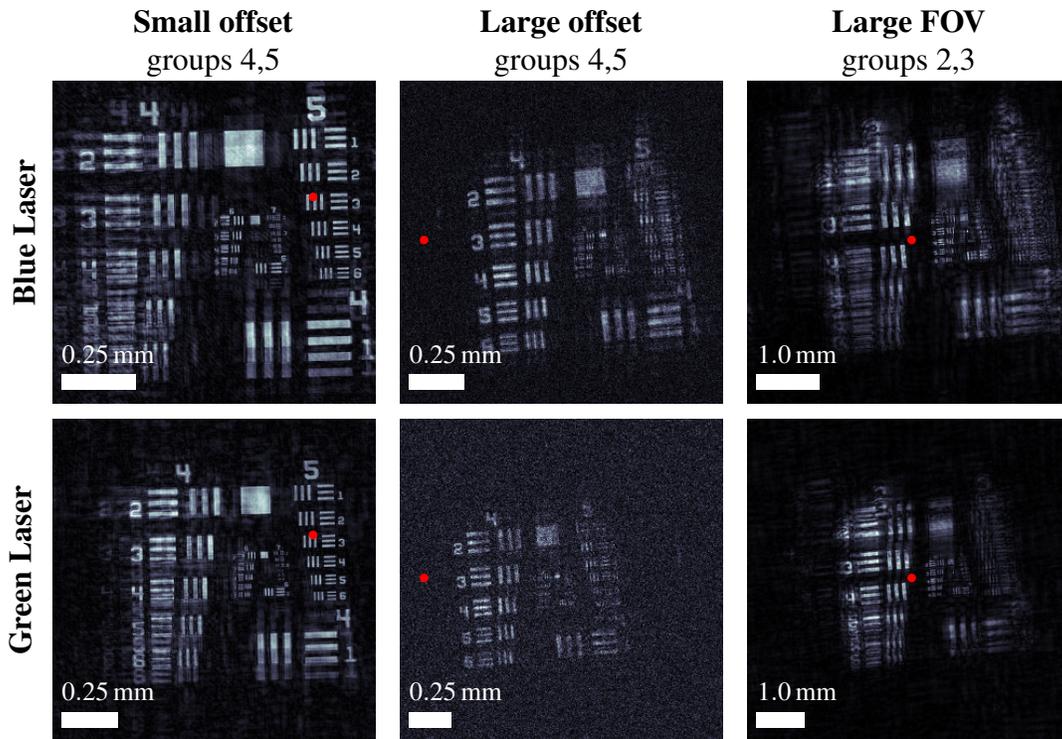
Figure 4.7 Demonstration of k-space position error effects. Images from three dual wavelength (532nm and 407nm) show the corruption of image data far from the effective pinhole location. The relative location of the pinhole (which is in the other output arm of the interferometer) is shown with a red dot in each image. The precision of our angular movement limits us to a clear image up to about 0.5 mm from the pinhole, corresponding to an angular accuracy of about 100 arcsecs (or about 50 arcsecs per mirror—5 times worse than we had measured independently). The ghosting caused, presumably, by periodic errors is clearly visible in the first image (look closely next to the label for group 4). Similar to the blurring and fading caused by random errors, the ghosting effect also gets more pronounced with increasing distance from the pinhole.

(relative to the main image) depends on the amplitude and period of the periodic error. This ghosting error is very similar to a well known phenomenon in MRI [33–35] in which ghosting occurs because of periodic movement. The k-space position error is related, because it has a similar effect of causing small periodic phase shifts to k-space measurements. Of course, the exact equivalent phenomena could also occur with MAS-IPSII if the object were to move periodically in sync with the scan. For example, rapid scans with rotating mirrors, etc. could cause vibrations that would also give rise to ghosting artifacts.

4.5 Aliasing

As discussed in Section 3.3, $\text{FOV}_{\mathfrak{F}}$ (the field of view of an image from a discrete inverse Fourier transform) depends on the spacing dk between points in k-space. A separate limit, FOV_{det}, is the field-of-view of the detector—the extent of the area contributing to the detector's signal. FOV_{det} is determined by the area of the illumination, the spatial response of the detector, and may also be controlled with additional optics such as an iris or other aperture placed before or after the object, or lenses. If $\text{FOV}_{\mathfrak{F}} < \text{FOV}_{\text{det}}$, then aliasing will occur, causing ghosting artifacts where areas from outside the $\text{FOV}_{\mathfrak{F}}$ appear superimposed in the image, such as demonstrated in Fig. 4.8.

| | **Full Data** | **Half k$_x$** | **Half k$_{x,y}$** | **One third k$_{x,y}$** |

Pixels: 301x301   151x301   151x151   101x101
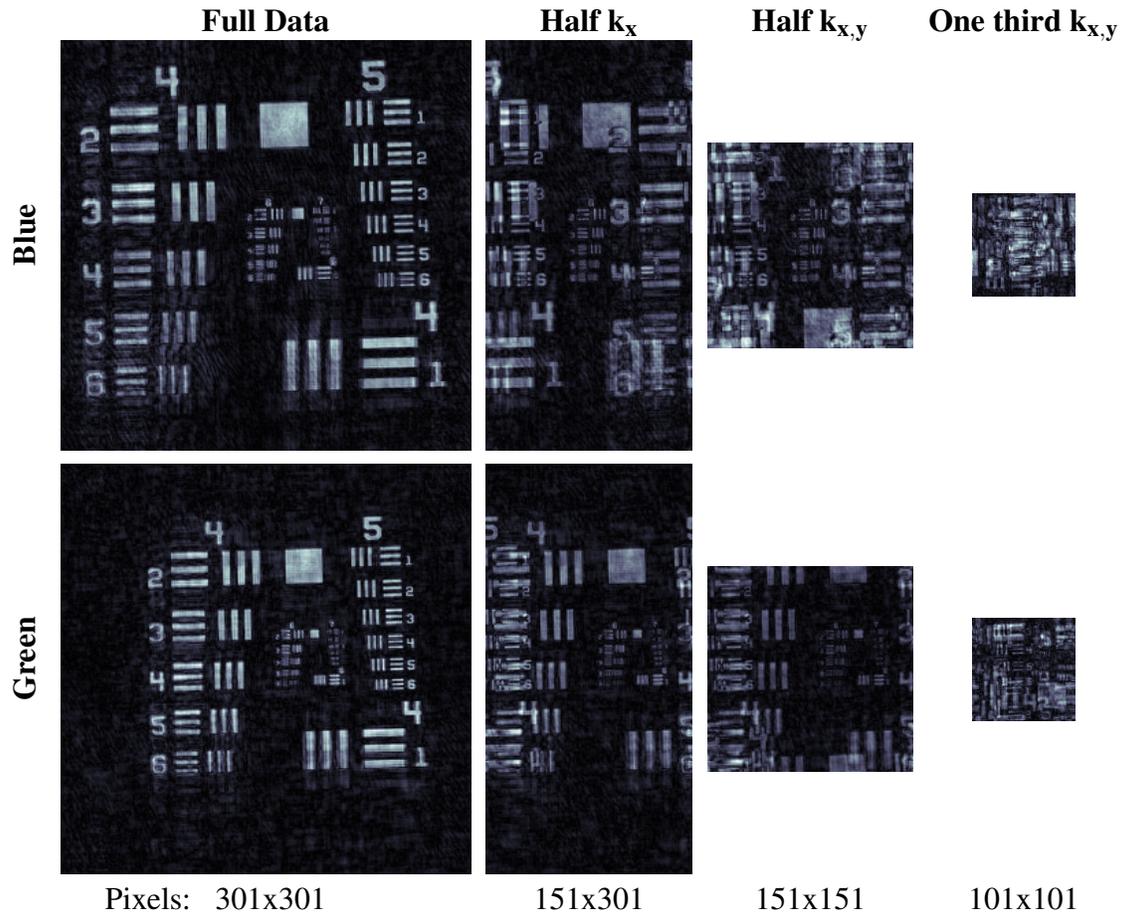
Figure 4.8 Demonstration of aliasing from incomplete data. The first column shows images formed from a complete k-space dataset from a single dual-wavelength scan. The proceeding columns show the result of skipping every other column (i.e. using half the k-space data), every other row and column (i.e. using one quarter of the data) or skipping 2 out of 3 rows and columns (i.e. using one ninth the total data). The top row contains images from data corresponding to blue (407nm) laser, and the bottom row contains data from a green (532nm) laser.

4.6 Potential Improvements to Imaging Speed

The limits on imaging speed discussed in Section 3.3 are only the limit if using a design such as what we presented in Chapter 2. This design was intended to make the experiment and data gathering as simple and controllable as possible, while demonstrating the feasibility of fully lensless IPSII. It was not designed for speed. Much faster designs could be used to drastically speed up MAS-IPSII (and would most likely be necessary for practical applications). I will lay out a few potential methods for improving the scan speed of MAS-IPSII, as well as some tricks that could be used to speed up any IPSII method. While we have not yet implemented most of these methods (due to the added complexity in engineering or data analysis they would require), I believe it is important to enumerate some of the ways it could be done, since our current research would likely be of little utility if MAS-IPSII were fundamentally limited to the speeds which we have demonstrated. The methods I will introduce are continuous rapid scans (instead of discrete steps), parallel imaging, multi-wavelength imaging, and compressive sensing.

Continuous Rotation

One method to drastically increase speed would be to precisely measure the angle instead of trying to precisely control it, enabling the use of much faster (but less controlled) methods of producing mechanical angle changes—for example, galvos or high speed motors. Of course the frequency shift would need to be much faster (fast enough that many oscillations occur between each k-step). Alternately, it may be possible to image without a separate phase scan at all, since the motion of the mirrors tends to sweep the phase as well.

One example of a design implementing a rapid continuous scan would be to mount the mirrors in an interferometer setup (such as Fig. 2.2) on motors with a rotational axis through the vertical axis of the mirror, and spin the mirrors as fast as possible. Keeping the two beams overlapping requires two mirrors be moved proportionately together (as discussed in Section 2.3.1), such that
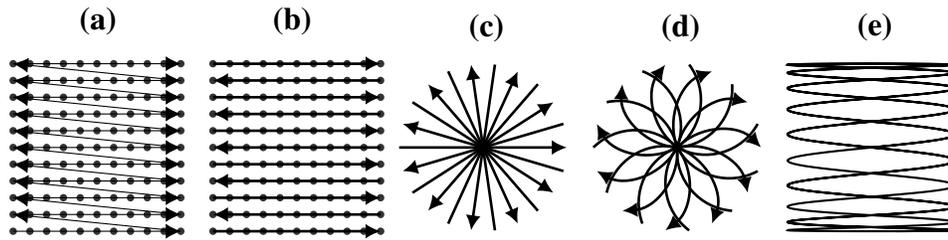
Figure 4.9 Various types of scan patterns discussed in the text. a) 2DFT Grid scan. b) 2D Grid scan, alternating direction—faster, but more prone to backlash errors in a mechanical scan. c) Spokes with uniform point spacing—requires regridding of data or a different inverse transform (basically a filtered back projection). e) Curved spokes—requires regriding of data. d) Lissajous figure—requires regriding of data.

for continuous motion, they could be locked together with an appropriate gear ratio, or sufficiently accurate software control. With such a setup, only a fraction of each rotation would result in proper positioning of the beams (i.e. before the beam falls off the second mirror), but during this portion of each rotation a full 1D scan through k-space could be recorded. In this case, rotation speeds of 10,000 rpm or greater could easily be obtained, with each rotation giving one row in k-space. To gather 2D data would require either rotating the object around the interferometer output axis, or vice versa.

Using a continuous scan pattern with continuous rotating mirrors would result in altered scan patterns. For example, if the object were rotated, with the object rotation paused before each 1D scan, the resulting scan pattern would be spokes in k-space (see Fig. 4.9), similar to what is obtained in CAT scans when performing filtered back projection. The same inverse transform could be applied here to recover an image of the object. If the rotation of the object were constant in time, the result would effectively be that of spiraling spokes, and the inverse transform would be somewhat more complicated. Alternately, the mirror could be made to swivel within the rotating mount to give simpler scan patterns at the cost of increased engineering complexity. In this case, a regular 2D scan could be obtained by incrementing the vertical angle a discrete amount before each scan. Higher speeds could potentially be obtained by scanning mirrors sinusoidally, which would result

in a Lissajous pattern in k-space.

The speed of any such imaging system would be orders of magnitude faster than our current setup. At 160 rotations/s (i.e 10,000 rpm, a fairly manageable speed for even inexpensive high speed electric motors) a 1 MPixel image could be taken in 6 s—fast enough to be practical in many microscopy applications.

Partial Fourier Reconstruction
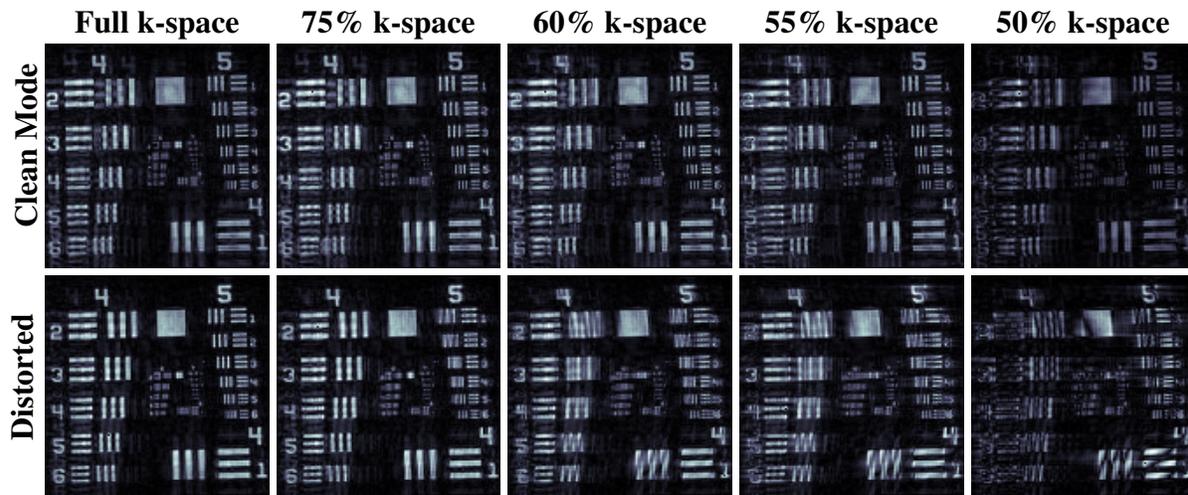
Figure 4.10 Partial k-space reconstruction. Shown are two sets of image reconstructions using only partial k-space data, one from a scan with a clean mode (interference patterns were from the Fourier basis) and one from a scan with a mode distorted up by a lens (patterns were from some distorted basis). Note that even with the distorted mode, a decent image can be formed with only 60% of k-space. These images were made by re-centering the k-space data (by moving the brightest pixel to the middle) and then using conjugate symmetry to fill in the bottom half of k-space. More advanced partial Fourier reconstruction algorithms should get even better results.

One way to speed up imaging is to just measure half of k-space (see the discussion around Eq. 4.1 in Section 4.2), but this can cause unwanted effects due to the phase distortions in the illuminating beams (such as in the middle two columns of Fig. 4.2 and 4.3). If these phase distortions are slowly changing in space, however, it is possible to get good results by scanning just a little more than

half of k-space, and then filling in the rest using conjugate symmetry. Using a technique from MRI called Partial Fourier Reconstruction [36], a partial data set can be further improved on by using the symmetrically sampled part of the data to fill in the missing data in k-space using an algorithm akin to the conjugate symmetry approach, but that also accounts for the phase variations in object space. This works because the data towards the center is sufficient to resolve the slowly varying phase distortions in the beam. The net result is that a good image can be reconstructed with about 60% of k-space, even when phase distortions are present (more or less data is needed depending on the spatial bandwidth of the phase distortions).

Parallel Imaging

Another potential method of speeding up MAS-IPSII (or other forms of IPSII) is parallel imaging. This method would use multiple detectors to effectively measure multiple small FOV images which are then combined into one large image. Examples of this idea include hybrid techniques that combine IPSII with traditional imaging systems. SIM is one example of this where each pixel of the imaging detector effectively measures a 2x2 pixel image, and these are all combined to make and image with double the resolution of what the imaging system alone could accomplish.

This idea can be taken farther, however, to work with an arbitrary FOV and detector pixel count. The IPSII k-step would just need to be small enough to make the IPSII FOV about the size of one pixel. An example of this is the multibeam technique employed at MIT [17].

Using auto-calibrating parallel imaging algorithms used in MRI such as SENSE or GRAPPA [37–39], parallel imaging could be done even with overlapping and unknown detector regions. This would allow for parallel imaging that would be unaffected by lens distortions and blurring between pixels in the conventional imaging system. Completely lensless parallel imaging could also be done in this manner if multiple detectors could be made to have distinct spatial responses (such as by placing a detector array close to the object, using a micro aperture array, or both—note though, that

this would not be constrained the same as other on-chip microscopy techniques, because diffraction between the object and the detector is less important).

Parallel imaging with N detectors could increase the speed of MAS-IPSII by up to a factor of N, though it may be somewhat less than N if auto-calibrating algorithms are used, and depending on the overlap of information between detectors. For example, if a low resolution traditional imaging system were used, such as a 128x128 pixel array, then arbitrary FOV and pixel count could still be obtained using IPSII, but 16,384 times faster than single pixel IPSII. This could be particularly powerful when combined with modern smart-pixel detector arrays [40–45] such as correlation sensors, which could do the analog lock-in detection on chip. Such sensors have been developed with some impressive processing capabilities, but are too limited in pixel count to generally be useful in conventional imaging systems. Combining them with IPSII techniques, however, would make good use of their capability without limiting the resolution or pixel count of the final image.

Multispectral Imaging

Another way to speed up IPSII is to image with multiple wavelengths at the same time. Examples of this include our own dual wave setup described in Chapter 2, as well as DEEP and $\mathscr{F}$-basis [19, 20]. This could increase the speed of a system by a factor of N where N is the number of wavelengths used within a spectral band over which the object does not change. For example, when measuring a monochrome (black and white) object, a red, blue and green laser could be used in the same mechanical sweep to measure the object 3 times faster. (With a full color object the speed would not be increased, but full color information could be obtained.)

If wavelengths very close together were used, such that they did not produce interference patterns with appreciably different k-values, they would need to be scanned separately somehow to measure k-space components far enough apart to be useful. This would likely be less useful with MAS-IPSII (which would need a separate scanable interferometer for each beam), but is a key

component of $\mathscr{F}$-basis, and the primary reason it can be so fast (along with acousto-optic controlled angle changes). For MAS-IPSII multiple beams could be used in the same interferometer to speed up a scan as long as they are separated in wavelength to change dk sufficiently to measure unique data.

Compressive Sensing

IPSII is also naturally suited to a set of techniques referred to as 'compressive sensing', which allows an image to be taken with fewer measurements than the pixel count of the final image. Compressive sensing requires some prior knowledge about the object to be imaged, which is an assumption that the image will be 'sparse' in some known image basis (i.e. will contain a large number of near zero values in that basis). It turns out that nearly all types of object images we are interested in have this property in Fourier related domains (and some others). By contrast, an image with little to no sparsity in the Fourier domain would most likely appear to be random noise to us. Compressive sensing works by transforming a partial dataset (with less than N points of data) to the known sparse domain (with N points of data). Because there are more points in the transformed basis than the initial dataset, there is not a unique solution. Instead, a solution with a high amount of sparsity, but still consistent with the data from the original dataset is found. This is then transformed to the object domain to recreate the object image.

Compressive sensing techniques have been applied with great success in MRI [46], where the data is taken on a randomized grid in k-space and the sparsity is minimized on a regular grid (even though both basis sets are composed of sinusoidal functions, they are different because of the chosen k-values). Due to the similarities between MAS-IPSII and MRI, the same approach and algorithms used in MRI could be applied. Unlike MRI, MAS-IPSII could also easily use non-sinusoidal basis functions to potentially optimize speed even more [47–49]. In other imaging fields where it has been applied, compressive sensing can often cut the number of measurements needed by a factor of

3 to 10 without visually degrading the resulting image reconstruction.

Combined Speed Improvements

All of these methods could be used together, resulting in the imaging speed increasing by the product of the speed improvement factors of the individual methods. For example, 4 lasers with slightly different wavelengths could be used with 4 high speed detectors, partial Fourier reconstruction, and compressive sensing with a modest compressive factor of 3 to improve the imaging speed by a net factor of $4 \times 4 \times 1.7 \times 3 = 82$. This would change the previously quoted example of a continuous rotation scan from a 6s scan time for a 1 MPixel image to only 73 ms, or about 14 frames/s—fast enough for many video microscopy applications. All of this could be done without the use of any lenses. Note, however, that this is just given as an example of what I believe is technically possible. We have not implemented some of these methods, so I can not comment on the technical difficulty of engineering such a system.

4.7   Dynamic Range

Dynamic range can be more problematic when imaging in the Fourier basis. Real life images tend to be relatively 'sparse' in the Fourier basis, meaning most of the k-space values are near zero, with a handful that are very large (relative to the image average). Experimentally, this means the signal on the detector will be very, very small for most measurements. It can not be amplified much, however, or the signal will saturate when measuring values near the center of k-space. The small values away from the center of k-space are where all the high resolution data is contained, though. Because of this, IPSII (similarly to MRI) requires sensors with a large dynamic range.

We have found that phase distortions in the interfering beams can significantly reduce the sparsity of the image in the Fourier domain (you can also think of this as changing the basis to one

in which the image is less sparse). The result is to effectively 'spread' the image energy around in k-space, drastically reducing the required dynamic range. This is demonstrated in Fig. 4.11, in which raw sensor data was truncated to various bit depths before analysis and image reconstruction. The resulting image reconstructions demonstrate, qualitatively, that the image made with the distorted beam requires 2-3 fewer bits, indicating dynamic range was reduced by a factor between 4 and 8. The reason for this is demonstrated in 4.12, which contains a histogram of the two k-space data sets, as well as k-space plots. Various quantitative estimates for dynamic range (e.g. comparing max value to the .1 percentile, or the non-zero min) indicate a dynamic range decrease by a factor of 3 to 7 in the distorted k-space data relative to the undistorted data (in agreement with the qualitative factor mentioned above).
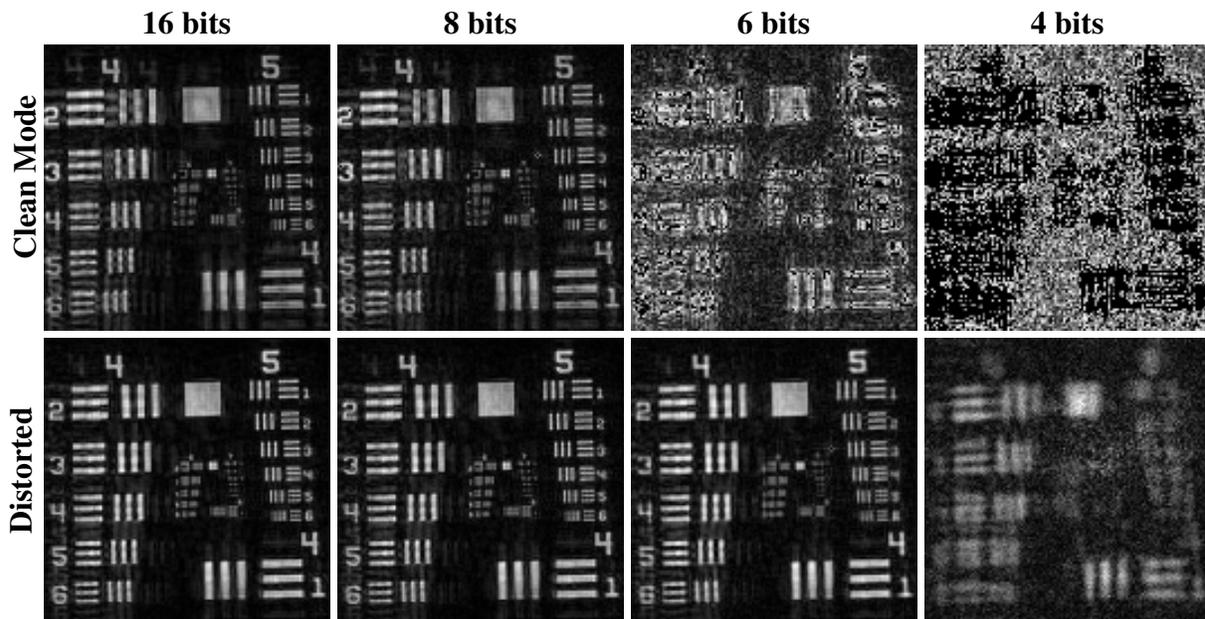
Figure 4.11 Bit depth and dynamic range. Shown are the resulting image constructions after truncating the raw signal data to a given number of bits. The reconstructions from the distorted imaging basis are much better at lower bit depth, demonstrating that they require a much lower dynamic range. See also Fig. 4.2.
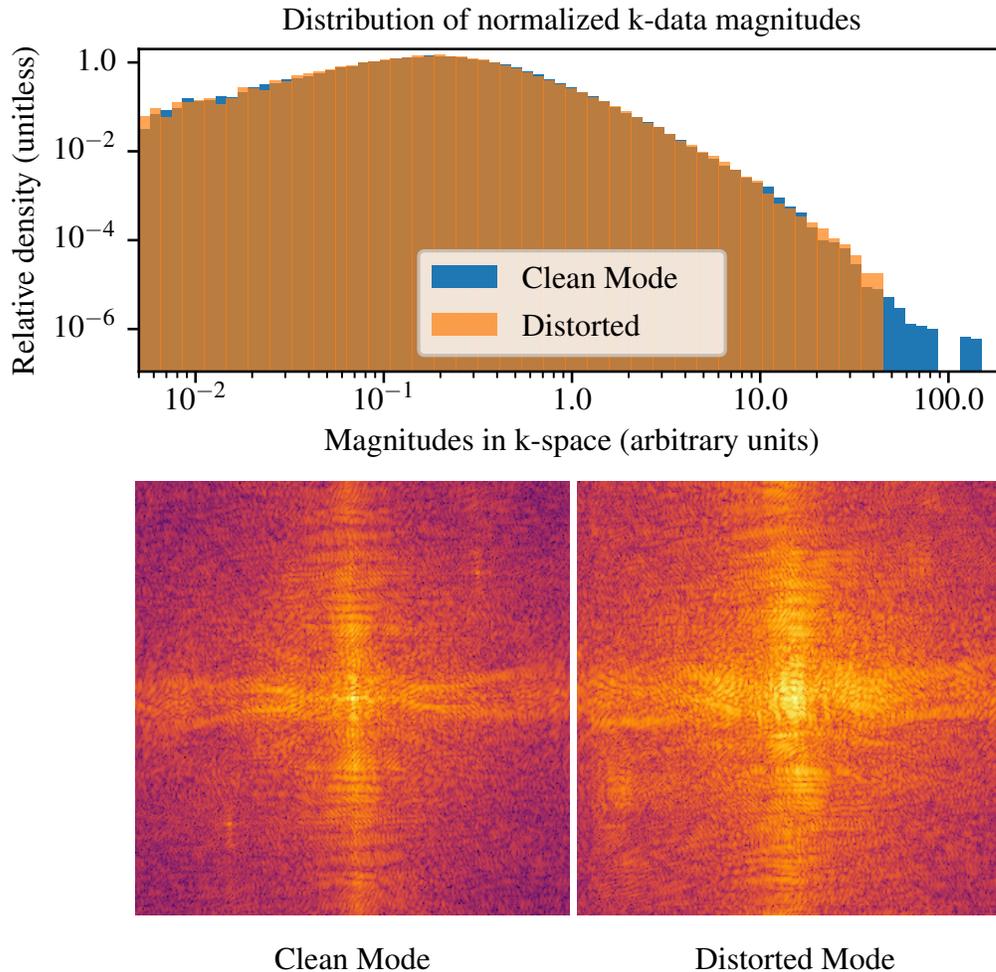
Figure 4.12 Effect of distortions on k-space sparsity. K-space magnitude density distributions are plotted (above) along with k-space magnitude images (below) from two scans, one with clean beam modes, and the other with one mode distorted by a lens (see Fig. 4.11 for corresponding image reconstructions). The axes and bins of the histogram are all logarithmically scaled. Note that distribution of values for the distorted mode is cut off at the high end, relative to the clean mode. The small number of measurements that fit into this area for the clean mode correspond to the peak in the center of k-space, and are responsible for the high dynamic range. Note how these areas of k-space appear smeared, or spread out in the k-space spectrum of the distorted mode.

Chapter 5

Conclusion

In this dissertation I have proposed and demonstrated a novel type of lensless imaging referred to as MAS-IPSII. This imaging technique can be done with nothing but flat optics, a single pixel detector, and a coherent wave source. No curved mirrors, lenses or other refractive focusing optics are required anywhere in the system. This leads to a singularly unique set of features: the ability to decouple working distance from resolution, even at subwavelength resolutions, and without a lens.

The theoretical limit of resolution of MAS-IPSII is $\lambda/4$. The fact that MAS-IPSII can be done without any lenses, and still achieve subwavelength resolution means that it could feasibly be used to improve on the state of the art resolution in areas of the spectrum where focusing devices (particularly those with high NA) are difficult or impossible to manufacture, such as the UV or x-ray regimes. Requiring only a single pixel detector is an additional benefit in these regimes.

Another advantage of MAS-IPSII is that it decouples resolution, optic size and working distance. It could be used to perform subwavelength imaging at arbitrarily large distances without arbitrarily large optics. This is very different from conventional imaging with focusing optics, which require an optic on the same scale as the working distance to reach resolutions on the order of the wavelength. Because lens size is very limited in practice (high NA focusing optics are only available up to a few centimeters in diameter), even state of the art microscopy can only be done at very close distances.

MAS-IPSII could be done from meters away. This is also very different from other lensless imaging techniques, which require even shorter working distances than conventional imaging to reach wavelength scale resolutions.

I also showed how to derive a signal equation summarizing the theory of 2D MAS-IPSII, and showed how this signal equation could be used in various types of 2D imaging. Those imaging types include measurements of an object, measurements of the intensity of a beam, or even a full complex measurement of a light field on a plane (i.e. a hologram). I showed data from proof-of-concept experiments performing each of these types of measurements.

In chapter 4 I discussed and quantified various practical issues that could arise with MAS-IPSII. Many of these are problems that we have dealt with, and I described solutions or workarounds to most of them.

Appendix A

Publications

A.1 MAS-IPSII

Our published works related to MAS-IPSII include a patent application [50] two peer reviewed conference proceedings [51, 52], and article in Optics Express [53].

A.2 Light Splitting with Imperfect Wave Plates

Abstract: We discuss the use of wave plates with arbitrary retardances, in conjunction with a linear polarizer, to split linearly polarized light into two linearly polarized beams with an arbitrary splitting fraction. We show that for non-ideal wave plates, a much broader range of splitting ratios is typically possible when a pair of wave plates, rather than a single wave plate, is used. We discuss the maximum range of splitting fractions possible with one or two wave plates as a function of the wave plate retardances, and how to align the wave plates to achieve the maximum splitting range possible when simply rotating one of the wave plates while keeping the other one fixed. We also briefly discuss an alignment-free polarization rotator constructed from a pair of half-wave plates. [54]

A.3 Laser Wavelength Metrology with Color Sensor Chips

Abstract: We present a laser wavelength meter based on a commercial color sensor chip. The chip consists of an array of photodiodes with different absorptive color filters. By comparing the relative amplitudes of light on the photodiodes, the wavelength of light can be determined. In addition to absorption in the filters, etalon effects add additional spectral features which improve the precision of the device. Comparing the measurements from the device to a commercial wavelength meter and to an atomic reference, we found that the device has picometer-level precision and picometer-scale drift over a period longer than a month. [55]

A.4 Magneto-Optical Trap Field Characterization with the Directional Hanle Effect

Abstract: We demonstrate the use of spatial emission patterns to measure magnetic fields. The directional aspect of the Hanle effect gives a direct, visual presentation of the magnetic fields, in which brighter fluorescence indicates larger fields. It can be used to determine the direction as well as the magnitude of the field. It is particularly well suited for characterizing and aligning magneto-optical traps, requiring little or no additional equipment or setup beyond what is ordinarily used in a magneto-optical trap, and being most sensitive to fields of the size typically present in a magneto-optical trap. [56]

Appendix B

Motorized Mirrors

We found that commercial motorized mirror mounts were lacking in either range or precision, i.e. they lack an effective 'dynamic angular range' (the ratio of the angular range to the angular precision). They are also very expensive (a single mirror would cost more than the rest of our setup combined). The dynamic range issue could, perhaps, be overcome by combining some commercial parts (i.e. a motorized adjustment screw with long range, and a compatible mirror mount), but we decided to make our own solution to get the range we need and save on cost. To do so we used standard manual kinematic mirror mounts, and 3D printed an attachment module used to mount inexpensive stepper motors on the commercial mirror mounts (see Fig. B.1). We used ultra fine threaded adjustment screws (254 TPI) to generate extra precision in our angular motions. The performance of these mounts is shown in Fig. B.2.
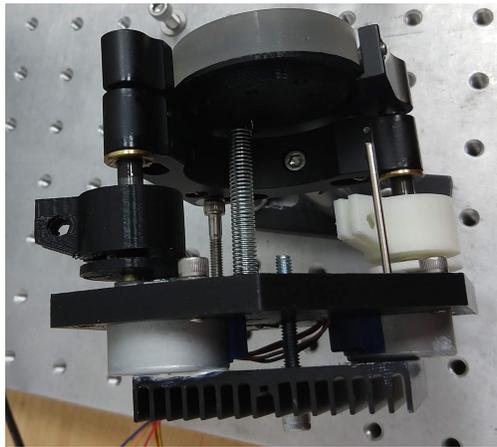
Figure B.1 Motorized mirror mounts. These mounts are made by using 3D printed parts to attach stepper motors to high TPI actuators placed in a 2 in kinematic mirror mount.
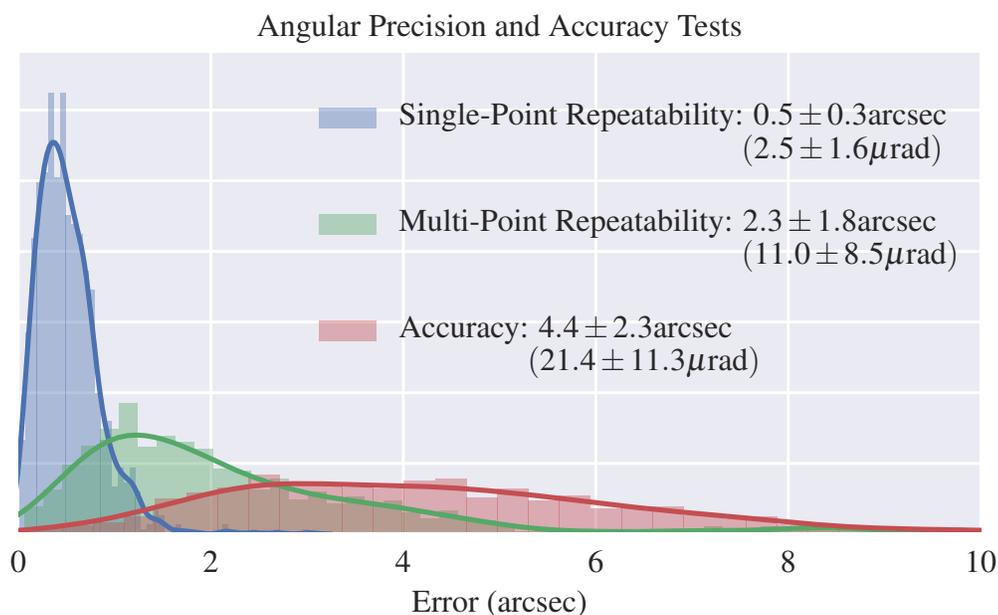
Figure B.2 Mirror performance. These data were taken by focusing a laser onto a CCD detector, with the lens placed before a motorized mirror. The position of the spot on the CCD detector was calculated to sub-pixel precision by calculating the first moment of the image. The position was then used to calculate the angular position of the spot relative to the mirror. Repeatibility was tested by adjusting the mirror from a measured point to a random position and back again, and measuring the net change in the position (which ideally should be 0). This test was done for a single randomly chosen point, and for a set of 10 randomly chosen points. The motor was then calibrated by using linear fit between motor position and physical angle. The accuracy of the calibration was tested by picking a random point, setting the corresponding motor position, and measuring the error between set and the measured spot location. Each test was done with 1000 measurement, and a distrubution of the errors of each test is displayed. Note that the repeatability is about 10x better than the accuracy. This is because non-linear couplings between the motor steps and the physical angle changes, which could theoretically be calibrated for if enough position data were measured.

Appendix C

Calibration Code

Python code:

```python
import numpy as np

# This code helps find the calibration numbers to move mirrors in sync
# The goal is that each arm of the intf should be able to change angle without
# changing the beam position *at the plane of the object*
#
# Unfortunately, the axis are not independent, which means a horizontal
# adjustment in one mirror requires horizontal and vertical adjustments in the
# second. However, this effect is small, so if the intf is set up symmetrically,
# and the object is about the same distance away as mirror 2 is from mirror 1,
# then the correction should be close to a factor of -2 in the same axis. i.e. if
# m1 is set to angle (a,b) then mirror two should be set to angle (-2a, -2b).
# This is a good starting point for what to expect.
#
# points are in this format:
# [ mirro1_position, mirror2_position ]
# = [(h1,v1), (h2, v2)] (where h1, etc. absolute steppermotor positions, or angles)
#
# To find calibration, make beam small (with iris), put an iris directly in
# front of a detector at the object location, connect to o-scope. Move m1 (mirror1) to
# maximize signal. Reset home coordinates. Set m2 to some angle (towards edge of
# range. manualMove(m1) to get the beam back on center and maximze signal again.
# Copy coordinates from:
#
```

```
#    [m1,m2,m3,m4] = intf. mirrors
#    [(m.stepperH. position , m.stepperV. position )  for  m in  [m1,m2]]
#
# Repeat  for  several  angles . Paste  points  below  in  an  array . Run array  through
# code  for  linear  regression   fits . This  will  tell  you the   calibration   values , as
# in  if  m1 is  set  to  (a,b)  the  m2 should be  set  to
#          (a2,  b2)  =  (h1*a+v1*b+c1, h2*a+v2*b+c2)
# The  fit  values  should  be  close  to  (h1,  v1,  h2,  v2) = (2,  0,  0,  2)
# The  resulting  beam angle  is  approximately  (a2−a1, b2−b1)
#
# Then this  whole process  should  be  repeated  for  arm2 (m3 and m4)
#
# Note,  the   fit  is done twice , once  allowing  for  a  fit   offset , c,  which should be
# close  to  0 ( if  you  started  at  the  right   position ), and once without  the  offset
#
# From mathematica − if  you want  to  go to  intf  angle  to  (th , tv )
# a = −((c1−th−c2 v1+tv v1+c1 v2−th v2)/(1+h1−h2 v1+v2+h1 v2))
# b = −((−c2−c2 h1+c1 h2−h2 th+tv+h1 tv)/(−1−h1+h2 v1−v2−h1 v2))
# then  m1 = (a,  b)
# and   m2 = (h1*a+v1*b, h2*a+v2*b) ~= (28th
# but  beam angle  is  2x mirror  angle , and  intf  angle = arm1+arm2
# so  for  beam angle (th ,  tv ) you should  input  (th /4,  tv /4)


# Calibration  data
points_arm1 =  [[(0,0) ,  (0,0) ],
               [(23408,  0),  (−50328, 234)],
               [(−23408, 23408),  (47753,  −47753)],
               [(23408,  −23408),  (−47753, 48689)],
               [(−23408,  −23408), (53371,  47753)],
               [(23408,  23408),  (−53137, −47285)],
               [(0,  23408),  (−2574,  −47519)]
               ]
points_arm2 =  [[(0,  0),  (0,  0) ],
               [(0,  23408),  (−2106,  −49860)],
               [(23408,  0),  (−51264, −3745)],
               [(23408,  23408),  (−53371, −51499)],
               [(−23408,  −23408), (52201,  44008)],
               [(−23408, 0),  (51030,  −3043)],
               [(0,  −23408), (1638,  45178)]
               ]


# Insert  data  set  here
```

```python
datasets = [np.vstack([np.hstack(p) for p in points_arm1]),
            np.vstack([np.hstack(p) for p in points_arm2])]
names = ['Arm1', 'Arm2']


# Perform regressions for each arm
for j in range(len(datasets)):
    p = datasets[j]
    print("Fitting {} 1st without offset, second with (better ?)".format(names[j]))

    # Perform the regression both with an offset, and without
    # (If calibration was done properly, offset should be 0)
    for i in [0,1]:
        m1 = np.c_[p[:,0:2], i*np.ones(len(p))]
        m2H = p[:,2]
        m2V = p[:,3]
        h1, v1, c1 = np.linalg.lstsq(m1, m2H)[0]
        h2, v2, c2 = np.linalg.lstsq(m1, m2V)[0]
        fs = "{:+04.4f}"
        print('Horizontal m2 axis h1, v1, c1, : {0}, {0}, {0}'.format(fs).format(h1,
            v1, c1))
        print('Vertical m2 axis h2, v2, c2, : {0}, {0}, {0}'.format(fs).format(h2,
            v2, c2))
        fs = "{:+04.5f}"
        print('Calibration String : [{0},{0},{0},{0}]'.format(fs).format(h1,v1,h2,v2))
    print('\n')
```

Appendix D

Scan Errors

Image	Log K-Space	Description
		The battery powering a very noise sensitive circuit was low, so the circuit was switched to be powered by an AC adapter. The resulting increase in noise is clearly visible as a strip in k-space.
		Reference signal or interferometer not tuned up very well resulting in some missing data points. Missing points are somewhat periodic.
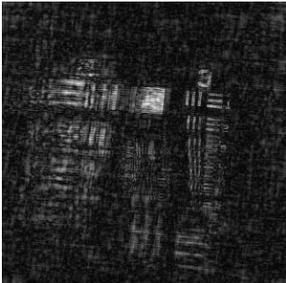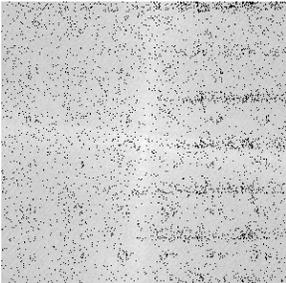
Periodic spots of missing data. In both cases the fringes on the pinhole were formed with non-ideal wavefronts in one or both beams. The pinhole signals were weaker and more noisy as a result, leading to occasional failures in the demodulation algorithm. The source of the periodicity is unknown, but could be related to periodic non-linearities in the stepper motors contributing to small misalignments, resulting in particular noisy signals periodically throughout the scan.

Motorized mirror failures leading to bad k-space data. Top: A stepper motor atachement slipped off one of the mirrors partway through the scan. Bottom: binding of one of the adjustment screws in one of the mirrors.

		Beam mode distorted so much (from plastic in beam) that the lock in algorithm often failed. Note that this occurred in large contiguous regions.
		A mirror was bumped causing a small misalignment partway through the scan causing a shift in k-space for the rest of the scan, as well as a drop in SNR.
		A stepper motor attachment came off towards the end of the scan causing the remaining data to be 'smeared' in the y direction.
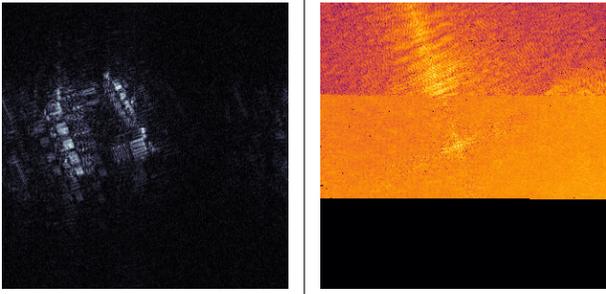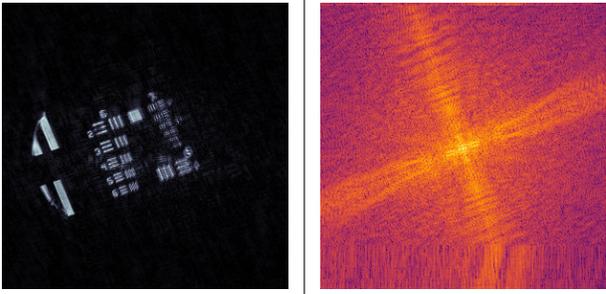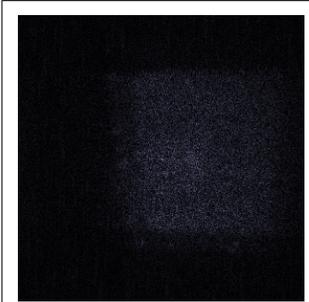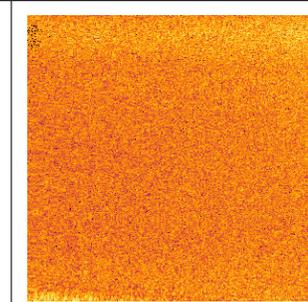
Table D.1 Scan error effects. A list of k-space and object space images are shown demonstrating results of various errors during the scan process.

Bibliography

[1] J. Garcia-Sucerquia, W. Xu, M. H. Jericho, and H. J. Kreuzer, "Immersion digital in-line holographic microscopy," Optics Letters **31,** 1211–1213 (2006).

[2] X. Cui, L. M. Lee, X. Heng, W. Zhong, P. W. Sternberg, D. Psaltis, and C. Yang, "Lensless high-resolution on-chip optofluidic microscopes for Caenorhabditis elegans and cell imaging," Proceedings of the National Academy of Sciences of the United States of America **105,** 10670–10675 (2008).

[3] W. Bishara, T.-W. Su, A. F. Coskun, and A. Ozcan, "Lensfree on-chip microscopy over a wide field-of-view using pixel super-resolution," Optics Express **18,** 11181–11191 (2010).

[4] S. Pang, X. Cui, J. DeModena, Y. M. Wang, P. Sternberg, and C. Yang, "Implementation of a color-capable optofluidic microscope on a RGB CMOS color sensor chip substrate," Lab on a Chip **10,** 411–414 (2010).

[5] A. Greenbaum, W. Luo, T.-W. Su, Z. Göröcs, L. Xue, S. O. Isikman, A. F. Coskun, O. Mudanyali, and A. Ozcan, "Imaging without lenses: achievements and remaining challenges of wide-field on-chip microscopy," Nature Methods **9,** 889 (2012).

[6] A. Ozcan and E. McLeod, "Lensless imaging and sensing," Annual Review of Biomedical Engineering **18,** 77–102 (2016).

[7] Z. Zhang, X. Ma, and J. Zhong, "Single-pixel imaging by means of Fourier spectrum acquisition," Nature Communications **6,** 6225 (2015).

[8] Z. Zhang, X. Wang, G. Zheng, and J. Zhong, "Hadamard single-pixel imaging versus Fourier single-pixel imaging," Optics Express **25,** 19619–19639 (2017).

[9] P. Chakraborty, "Layered synthetic microstructures as optical elements for the extreme ultraviolet and soft X-rays," International Journal of Modern Physics B **5,** 2133–2228 (1991).

[10] A. Akhsakhalyan *et al.*, "Current status and development prospects for multilayer X-ray optics at the Institute for Physics of Microstructures, Russian Academy of Sciences," Journal of Surface Investigation: X-ray, Synchrotron and Neutron Techniques **11,** 1–19 (2017).

[11] T. Ueno, M. Hasegawa, M. Yoshimura, H. Okada, T. Nishioka, K. Teraoka, A. Fujii, and S. Nakayama, "Development of ZnS lenses for FIR cameras," SEI Technical Review 69 (2009).

[12] X. Jiang *et al.*, "All-dielectric metalens for terahertz wave imaging," Optics Express **26,** 14132–14142 (2018).

[13] V. Poher *et al.*, "Optical sectioning microscopes with no moving parts using a micro-stripe array light emitting diode," Optics Express **15,** 11196–11206 (2007).

[14] S. Battiato, A. R. Bruna, G. Messina, and G. Puglisi, *Image processing for embedded devices* (Bentham Science Publishers, 2010).

[15] M. S. Mermelstein, "Synthetic aperture microscopy," Ph.D. thesis, Massachusetts Institute of Technology, 1999.

[16] M. S. Mermelstein, "Multiple beam pair optical imaging,", U.S. Patent 6,016,196 (Jan 18, 2000).

[17] S. S. Hong, M. S. Mermelstein, B. K. P. Horn, and D. M. Freeman, "High-resolution microscopy without high-numerical-aperture lenses: standing-wave scanning fluorescence microscopy," the Defense Advanced Research Projects Agency (DARPA) under grant N66001-02-1-8915 .

[18] J. Ryu, S. S. Hong, B. K. P. Horn, D. M. Freeman, and M. S. Mermelstein, "Multibeam interferometric illumination as the primary source of resolution in optical microscopy," Applied Physics Letters **88,** 171112 (2006).

[19] D. Feldkhun and K. H. Wagner, "Single-shot afocal three-dimensional microscopy," Optics Letters **41,** 3483–3486 (2016).

[20] D. Feldkhun and K. H. Wagner, "Doppler encoded excitation pattern tomographic optical microscopy," Applied Optics **49,** H47–H63 (2010).

[21] D. Feldkhun, "Fourier domain sensing,", U.S. Patent 8,184,279 (May 22, 2012).

[22] G. Futia, P. Schlup, D. G. Winters, and R. A. Bartels, "Spatially-chirped modulation imaging of absorbtion and fluorescent objects on single-element optical detector," Optics Express **19,** 1626–1640 (2011).

[23] D. J. Higley, D. G. Winters, G. L. Futia, and R. A. Bartels, "Theory of diffraction effects in spatial frequency-modulated imaging," Journal of the Optical Society of America A **29,** 2579–2590 (2012).

[24] J. J. Field, D. G. Winters, and R. A. Bartels, "Plane wave analysis of coherent holographic image reconstruction by phase transfer (CHIRPT)," Journal of the Optical Society of America A **32,** 2156–2168 (2015).

[25] J. J. Field and R. A. Bartels, "Digital aberration correction of fluorescent images with coherent holographic image reconstruction by phase transfer (CHIRPT)," Proceedings SPIE **9713,** 97130B (2016).

[26] B. Judkewitz and C. Yang, "Axial standing-wave illumination frequency-domain imaging (SWIF)," Optics Express **22,** 11001–11010 (2014).

[27] L.-H. Yeh, L. Tian, and L. Waller, "Structured illumination microscopy with unknown patterns and a statistical prior," Biomedical Optics Express **8,** 695–711 (2017).

[28] J. Tan, C. Wang, Y. Wang, W. Wang, J. Liu, R. Leach, and L. Hao, "Long working distance microscope with a low obscuration aspherical Schwarzschild objective," Optics Letters **39,** 6699–6702 (2014).

[29] J. T. Frohn, H. F. Knapp, and A. Stemmer, "True optical resolution beyond the Rayleigh limit achieved by standing wave illumination," Proceedings of the National Academy of Sciences of the United States of America **97,** 7232–7236 (2000).

[30] R. Dorn, S. Quabis, and G. Leuchs, "Sharper focus for a radially polarized light beam," Physical Review Letters **91,** 233901 (2003).

[31] V. Kalosha and I. Golub, "Toward the subdiffraction focusing limit of optical superresolution," Optics Letters **32,** 3540–3542 (2007).

[32] G. M. Lerman and U. Levy, "Effect of radial polarization and apodization on spot size under tight focusing conditions," Optics Express **16,** 4567–4581 (2008).

[33] L. Axel, R. Summers, H. Kressel, and C. Charles, "Respiratory effects in two-dimensional Fourier transform MR imaging.," Radiology **160,** 795–801 (1986).

[34] M. L. Wood and R. M. Henkelman, "MR image artifacts from periodic motion," Medical Physics **12,** 143–151 (1985).

[35] P. Storey, Q. Chen, W. Li, R. R. Edelman, and P. V. Prasad, "Band artifacts due to bulk motion," Magnetic Resonance in Medicine: An Official Journal of the International Society for Magnetic Resonance in Medicine **48,** 1028–1036 (2002).

[36] G. McGibney, M. R. Smith, S. T. Nichols, and A. Crawley, "Quantitative evaluation of several partial Fourier reconstruction algorithms used in MRI," Magnetic Resonance in Medicine **30,** 51–59 (1993).

[37] K. P. Pruessmann, M. Weiger, M. B. Scheidegger, and P. Boesiger, "SENSE: sensitivity encoding for fast MRI," Magnetic Resonance in Medicine **42,** 952–962 (1999).

[38] M. A. Griswold, P. M. Jakob, R. M. Heidemann, M. Nittka, V. Jellus, J. Wang, B. Kiefer, and A. Haase, "Generalized autocalibrating partially parallel acquisitions (GRAPPA)," Magnetic Resonance in Medicine **47,** 1202–1210 (2002).

[39] M. Blaimer, F. Breuer, M. Mueller, R. M. Heidemann, M. A. Griswold, and P. M. Jakob, "SMASH, SENSE, PILS, GRAPPA: how to choose the optimal method," Topics in Magnetic Resonance Imaging **15,** 223–236 (2004).

[40] J. Mitić, T. Anhut, M. Meier, M. Ducros, A. Serov, and T. Lasser, "Optical sectioning in wide-field microscopy obtained by dynamic structured light illumination and detection based on a smart pixel detector array," Optics Letters **28,** 698–700 (2003).

[41] S. Bourquin, P. Seitz, and R. P. Salathé, "Two-dimensional smart detector array for interferometric applications," Electronics Letters **37,** 975–976 (2001).

[42] S. Ando and A. Kimachi, "Correlation image sensor: Two-dimensional matched detection of amplitude-modulated light," IEEE Transactions on Electron Devices **50,** 2059–2066 (2003).

[43] M. Habibi, "A high sensitivity correlation image sensor," In *Sensors Applications Symposium (SAS), 2011 IEEE*, pp. 197–202 (2011).

[44] M. Habibi, "Analysis, enhancement, and sensitivity improvement of the correlation image sensor," IEEE Transactions on Instrumentation and Measurement **61,** 708–718 (2012).

[45] B. Büttgen and P. Seitz, "Robust Optical Time-of-Flight Range Imaging Based on Smart Pixel Structures," IEEE Transactions on Circuits and Systems **55,** 1512–1525 (2008).

[46] M. Lustig, D. Donoho, and J. M. Pauly, "Sparse MRI: The application of compressed sensing for rapid MR imaging," Magnetic Resonance in Medicine **58,** 1182–1195 (2007).

[47] M. F. Duarte, M. A. Davenport, D. Takhar, J. N. Laska, T. Sun, K. F. Kelly, and R. G. Baraniuk, "Single-pixel imaging via compressive sampling," IEEE Signal Processing Magazine **25,** 83–91 (2008).

[48] D. Takhar, J. N. Laska, M. B. Wakin, M. F. Duarte, D. Baron, S. Sarvotham, K. F. Kelly, and R. G. Baraniuk, "A new compressive imaging camera architecture using optical-domain compression,", Proceedings SPIE, 2006.

[49] T. T. Do, L. Gan, N. H. Nguyen, and T. D. Tran, "Fast and efficient compressive sensing using structurally random matrices," IEEE Transactions on Signal Processing **60,** 139–154 (2012).

[50] D. S. Durfee and J. Jackson, "Wave interference systems and methods for measuring objects and waves,", U.S. Patent App. 16/030,520 (January 10, 2019).

[51] J. Jackson and D. Durfee, "Lensless Single Pixel Imaging with Laser Interference Patterns," Microscopy and Microanalysis **24,** 1366–1367 (2018).

[52] J. S. Jackson and D. S. Durfee, "Demonstration of Interference Pattern Structured Illumination Imaging," In *Frontiers in Optics*, pp. FW7B–6 (2018).

[53] J. Jackson and D. Durfee, "Mechanically scanned interference pattern structured illumination imaging," Optics Express **27,** 14969–14980 (2019).

[54] J. S. Jackson, J. L. Archibald, and D. S. Durfee, "Light splitting with imperfect wave plates," Applied Optics **56,** 1062–1068 (2017).

[55] T. B. Jones, N. Otterstrom, J. Jackson, J. Archibald, and D. S. Durfee, "Laser wavelength metrology with color sensor chips," Optics Express **23,** 32471–32480 (2015).

[56] J. S. Jackson and D. S. Durfee, "Magneto-Optical Trap Field Characterization with the Directional Hanle Effect," arXiv e-prints p. arXiv:1703.03817 (2017).